

DTIC FILE COPY

AFOSR-TR. 89-0128

(2)

# HIGH-TEMPERATURE METAL MATRIX COMPOSITES

AD-A204 619

ANNUAL REPORT

VOLUME 1

DTIC  
ELECTE  
FEB 17 1989  
S D  
D C

AIR FORCE OFFICE OF SCIENTIFIC RESEARCH

Contract No. F49620-87-C-0017

October 1, 1987 - September 30, 1988

DISTRIBUTION STATEMENT A  
Approved for public release  
Distribution Unlimited

CARNEGIE MELLON UNIVERSITY

Pittsburgh, PA 15213

Principal Investigator, A.W. Thompson

and

University of California, Berkeley  
Clemson University

October 30, 1988

89 2 16 090

ADA204619

REPORT DOCUMENTATION PAGE				
1a REPORT SECURITY CLASSIFICATION Unclassified		1b RESTRICTIVE MARKINGS		
2a SECURITY CLASSIFICATION AUTHORITY		3 DISTRIBUTION/AVAILABILITY OF REPORT See Distribution List		
2b DECLASSIFICATION/DOWNGRADING SCHEDULE				
4 PERFORMING ORGANIZATION REPORT NUMBER(S)		5 MONITORING ORGANIZATION REPORT NUMBER(S) APOSR-TR-89-0128		
6a NAME OF PERFORMING ORGANIZATION Dept. of Metallurgical Eng. and Materials Science	6b OFFICE SYMBOL (if applicable)	7a NAME OF MONITORING ORGANIZATION AFOSR/NE		
6c ADDRESS (City, State, and ZIP Code) Carnegie Mellon University Pittsburgh, PA 15213		7b ADDRESS (City, State, and ZIP Code) Bldg. 410 Colling AFB, DC 20332		
8a NAME OF FUNDING/SPONSORING ORGANIZATION Air Force Office of Sci. Res.	8b OFFICE SYMBOL (if applicable) NE	9 PROGRAM/INSTRUMENT IDENTIFICATION NUMBER F49620 87-C-0017		
8c ADDRESS (City, State, and ZIP Code) Bldg. 410 Colling AFB, DC 20332		10 SOURCE OF FUNDING NUMBERS		
		PROGRAM ELEMENT NO. 61102F	PROJECT NO. 2306	TASK NO. A1
11 TITLE (Include Security Classification) High-temperature Metal Matrix Composites (Vol 1)				
12 PERSONAL AUTHOR(S) A.W. Thompson and those listed in table of contents				
13a TYPE OF REPORT Annual Report	13b TIME COVERED FROM 10/1/87 to 9/30/88	14 DATE OF REPORT (Year, Month, Day) 1988 October 30	15 PAGE COUNT 430	
16 SUPPLEMENTARY NOTATION				
17 COSATI CODES			18 SUBJECT TERMS (Continue on reverse if necessary and identify by block number)	
FIELD	GROUP	SUB-GROUP	High-temperature metal-matrix composites, interfaces, composite processing, aluminides, Ti-aluminides, fatigue, creep, toughness, atomic resolution. (JTS) ←	
19 ABSTRACT (Continue on reverse if necessary and identify by block number) The Annual Report for Year 2 of the University Research Initiative grant at Carnegie Mellon University on High-temperature Metal Matrix Structural Composites contains sections on processing, characterization, and mechanical properties. These are further divided into reports from individual tasks on powder blending and consolidation, composite performance, structure and composition of composite interfaces, fatigue crack growth, creep, and fracture behavior.				
20 DISTRIBUTION/AVAILABILITY OF ABSTRACT <input checked="" type="checkbox"/> UNCLASSIFIED/UNLIMITED <input type="checkbox"/> SAME AS RPT <input type="checkbox"/> DTIC USERS			21 ABSTRACT SECURITY CLASSIFICATION Unclassified	
22a NAME OF RESPONSIBLE INDIVIDUAL A.W. Thompson			22b TELEPHONE (Include Area Code) (412) 268-2700/20	22c OFFICE SYMBOL NE

# TABLE OF CONTENTS

## VOLUME 1

	<u>Page</u>
SUMMARY	1
STATEMENT OF WORK	3
TECHNICAL PROGRESS REPORT	
SECTION 1, Processing	5
Task 1: "Blending of P/M Metal Matrix Composites", J.O.G. Parent, J. Iyengar, M. Kuhni and H. Henein	9
"Deformation Processing of Composites", H.R. Piehler, D.M. Watkins, M. Kuhni and J. Richter	57
Task 2: "High Temperature Structural Materials", H.J. Rack	91
SECTION 2, Characterization	171
Task 3: "Interfacial Structure and Stability in Metal and Intermetallic Matrix Composites", J.M. Howe	173

## VOLUME 2

Task 3 (continued)	209
SECTION 3, Properties and Performance	279
Task 4: "Toughness and Fatigue of Metal Matrix Composites", R.O. Ritchie	281
Task 5: "Creep of High Temperature Composite Matrices", W. Cho, A.W. Thompson and J.C. Williams	377
Task 6: "Thermal and Mechanical History Effects", W.M. Garrison and D. Symons	411



By _____	
Distribution/ _____	
Availability Codes	
Dist	Avail and/or Special
A-1	

## SUMMARY

This second Annual Report for the University Research Initiative program at Carnegie Mellon University, including subcontracted research efforts at Clemson University and at the University of California (UC), Berkeley, contains technical summaries for each of six task areas. These are listed below by Task title and Task Investigator(s). The individual sections in the body of the report follow in this same order, and are grouped into three major parts, Processing (Tasks 1 and 2), Characterization (Task 3), and Properties and Performance (Tasks 4, 5 and 6). Task 2 is being conducted at Clemson and Task 4 at UC Berkeley.

- Task 1. Experimental Study of Processing of Composites. H. Henein, H.R. Piehler
- Task 2. Modeling of Consolidation and Deformation Processing of Composites. H.J. Rack
- Task 3. Structure and Composition of Interfaces in Composites. J.M. Howe
- Task 4. Toughness and Fatigue of Metal Matrix Composites. R.O. Ritchie
- Task 5. Micromechanisms of High Temperature Composite Behavior. A.W. Thompson
- Task 6. Thermal and Mechanical History Effects on Composite Properties. W.M. Garrison

The Processing part of the report comprises three reports. The first of these, by Parent and co-authors, addresses several issues in powder blending as a processing step for metal matrix composites. Emphasis is being placed on fundamental understanding of the mechanisms of blending, with account being taken of powder characteristics and operating and design variables, toward a goal of using physical models to identify scale-up criteria in blending. Results have been concentrated on spherical particle experiments, with successful definition and measurement of a segregation behavior diagram for binary mixtures. The second report, completing the summary for Task 1, is by Piehler and co-authors, on the subject of consolidation processing, as a natural complement to the first part of Task 1. The primary accomplishment has been achieving operational status for the hot triaxial compaction apparatus, which can apply shear in addition to hydrostatic stresses. This equipment has impressive capabilities and has been described as unique in the United States. Among the early goals is to test Ashby's hot isostatic pressing diagrams, and to extend them to the conditions of superimposed shear. Completing the Processing part is the Task 2 report, from H.J. Rack, addressing several topics related to consolidation and performance of metal matrix composites. A sub-task on interfacial modification for reinforcement phases in metal matrix composites has yielded several important results, particularly for carbon fibers. Two other sub-tasks have addressed composite performance, one in titanium aluminides and the other in a model system, Inconel 718 reinforced with TiC particulates.

The Characterization part of the report, from J.M. Howe, has focused on two objectives. The first was to complete a study of residual strains in a model composite system, a SiC-whisker reinforced aluminum alloy. This work has been finished, and the results are being submitted for publication. The second objective was to continue work on the structure and the deformation behavior of interfaces in alloys based on TiAl and Ti<sub>3</sub>Al. Both the structure and the deformation response of alpha-2/gamma interfaces have been studied, and interesting results have been obtained for both ordered and disordered hcp/bcc interfaces.

The Properties and Performance part of the report contains reports from three tasks. The first, from R.O. Ritchie, addresses micromechanisms of critical and sub-critical crack advance in composites. Work to date has been carried out in model composite systems with particulate reinforcement. At low fatigue crack growth rates, it was found that crack hindrance or trapping and roughness-induced crack closure occurred, resulting in lower growth rates than in

unreinforced materials. At intermediate growth rates, the composite also showed improved crack growth resistance, now due to crack tip bridging, a behavior which was successfully modeled. The second report in this part is by A.W. Thompson and J.C. Williams, and has the topic of creep and deformation of aluminide materials. A fairly complete report on creep in the  $Ti_3Al$ -based alloy, Ti-25 Al-10 Nb-3 V-1 Mo, is included. It was found that microstructure of this alloy strongly influenced creep behavior, and that mechanistic evidence indicated dislocation-controlled creep, with an activation energy consistent with literature values. This Ti-25-10-3-1 alloy was more creep resistant than near-alpha titanium alloys recently developed for creep performance. The third report in this part, by Garrison and Symons, discusses work on thermal and mechanical history effects. The work in this period has been on two titanium aluminide alloys, Ti-24 Al-11Nb and Ti-24 Al-17 Nb. Mechanical properties and thermal stability of the microstructures obtainable in these alloys have been studied to provide guidance for additional work, concentrating on the three microstructural variables which appear to be central to the fracture mechanisms in the alloys, namely alpha-2 plate size, volume fraction of second phase, and amount of c+a slip.

### STATEMENT OF WORK

The program in progress is an integrated study of composite materials having metal, ceramic or intermetallic matrices with particulate or fiber reinforcements, produced under controlled and understandable conditions, characterized in detail, emphasizing interface structure and composition, and with measurement and modeling of a broad range of mechanical properties, at ambient and elevated temperature.

- Task 1. Develop experimental capability with triaxial forging; conduct powder blending experiments and apply to compaction/forging experiments; determine experimental fiber rotation and breakage for comparison to Task 2 results; capture experimental understanding in frame-based expert system.
- Task 2. Conduct extension of existing finite element code to accommodate compaction of powder; include porous flow effects, friction effects, and fiber rotation and breakage; verify experimentally.
- Task 3. Characterize structure, composition, and bonding of interfaces between metal, ceramic, or intermetallic matrix and reinforcements, at ambient and elevated temperature, as functions of processing history from Tasks 1 and 2; determine residual stresses and deformation micromechanisms in composites.
- Task 4. Identify extrinsic toughening mechanisms in fatigue and fracture of composite materials, at ambient and elevated temperature; develop micromechanical models for intrinsic and extrinsic contributions to cracking resistance, in cooperation with Tasks 5 and 6.
- Task 5. Conduct creep, fatigue, stress rupture and creep-fatigue evaluations on metal and intermetallic matrix composites, under conditions of varying stress, strain amplitude and temperature; identify micromechanisms of failure; integrate results into behavior models with Tasks 4 and 6.
- Task 6. Examine effects of thermal and mechanical history on mechanical performance of metal and intermetallic matrix composites, through testing at varying temperature and service stress conditions; characterize micromechanisms of deformation and fracture as a function of exposure history; develop model descriptions of performance with Tasks 4 and 5.

In addition to these task-specific efforts, there will be several other objectives of work which involve integration among tasks. Some are shown above explicitly; others are listed below.

- Determine interrelationships among composite processing parameters, composite microstructure (including interfacial characteristics), and mechanical behavior, at ambient and elevated temperature (all tasks).
- Identify and model fundamental micromechanisms of mechanical behavior, at ambient and elevated temperature, in composite materials (Tasks 4-6).



**PART 1**

**PROCESSING**





## PROCESSING

The processing portion of the URI program on High-temperature Metal Matrix Composites is being accomplished in the form of two tasks. The first task is conducted at Carnegie Mellon University and has two parts, each with its own Investigator. The first part is under H. Henein and addresses powder blending, particularly as it affects consolidation issues. The second part is directed by H.R. Piehler and is concerned with deformation processing of composites, both for fiber and particulate reinforcements. The second task in the processing portion of the program is being carried out at Clemson University under the direction of H.J. Rack. Under a general task title of "Modeling of Consolidation and Deformation Processing of Composites", this task is addressing several interrelated topics, as described on p. 91. These include modification of the interface of composite reinforcements for improved performance; a study of a series of Ti-Al-Nb-V and Ti-Al-V aluminide alloys for high-temperature properties; and the first part of a study of creep in a model composite, Inconel 718 reinforced with particulate TiC.

	<b>Page</b>
<b>Task 1: "Blending of P/M Metal Matrix Composites", J.O.G. Parent, J. Iyengar, M. Kuhni and H. Henein</b>	<b>9</b>
<b>"Deformation Processing of Composites", H.R. Piehler, D.M. Watkins, M. Kuhni and J. Richter</b>	<b>57</b>
<b>Task 2: "High Temperature Structural Materials", H.J. Rack</b>	<b>91</b>



## **Blending of P/M Metal-Matrix Composites**

**J.O.G. Parent**

**J. Iyengar**

**M. Kuhn**

**H. Hensel**

**Department of Metallurgical Engineering and Materials Science  
Carnegie Mellon University  
Pittsburgh, Pennsylvania**

**Annual Report - Year 2**

---

**Table of Contents**

---

- 1. Introduction**
- 2. Previous Work**
  - 2.1 Bed Behavior
  - 2.2 Mixing
  - 2.3 Segregation
  - 2.4 Effect of Gas Atmosphere on the Flow Properties of Powder Beds
  - 2.5 Summary
- 3. Experimental Apparatus and Program**
  - 3.1 Model Materials**
    - 3.1.1 Experimental Setup
    - 3.1.2 Experimental Variables and Procedure
    - 3.1.3 Results and Discussions
    - 3.1.4 Conclusions
  - 3.2 MMC Powder Materials**
    - 3.2.1 Apparatus
    - 3.2.2 Materials
    - 3.2.3 Procedure
    - 3.2.4 Variables of Interest and Test Matrix
- References**

---

**List of Figures**

---

- Figure 1-1:** Powder metallurgy processing route (adapted from Willis<sup>1</sup>).
- Figure 2-1:** Modes of Transverse Bed Motion (adapted from Henlein et al.<sup>3</sup>).
- Figure 2-2:** Regions of Mixing in the Bed of a Rotary System
- Figure 2-3:** Segregated region formation (adapted from Donald and Roseman<sup>12</sup>).
- Figure 2-4:** Effect of Apparatus Speed ( $V_a$ ) and Viscosity ( $\mu$ ) on the Gas Interaction Number
- Figure 2-5:** Effect of Particle Size ( $d_p$ ), Viscosity ( $\mu$ ) and Apparatus Speed ( $V_a$ ) on the Gas Interaction Number
- Figure 3-1:** Equipment Schematic for Model Experiments
- Figure 3-2:** Experimental results for model materials, for increasing speed.
- Figure 3-3:** Segregation behavior for varying size ratios and drum speeds, for increasing speed (solid lines) and decreasing speed (dashed lines).
- Figure 3-4:** Segregation behavior for varying percent fines and percent fill.
- Figure 3-5:** Segregation behavior for varying density ratio.
- Figure 3-6:** Schematic of gas delivery system for blending experiments
- Figure 3-7:** Materials for use in blending experiments
- Figure 3-8:** Initial placement of reinforcement and matrix charge.

---

**List of Tables**

---

**Table 2-1:** Data for Calculation of  $N_1$  as a Function of the Apparatus Speed

**Table 2-2:** Data for Calculation of  $N_1$  as a Function of the Particle Size

**Table 3-1:** Model Material Characteristics

**Table 3-2:** Experimental Variables

**Table 3-3:** Materials for Blending Experiments

---

## Chapter 1

---

### Introduction

The need to achieve reproducible results in the formation of composite materials has prompted considerable interest in the materials research community. Several methods are available to produce such materials: liquid metal infiltration, powder metallurgy (P/M) processing, formation of composites from the melt and spray deposition techniques are but a few. Those techniques which use the liquid metal as a starting point seem to provide an inexpensive means of processing metal matrix composites (MMC's). In many cases, however, concerns about possible contamination of the matrix material while in the liquid form, as well as prohibitively high melting points make liquid metal techniques inappropriate. In such cases, the powder metallurgy route provides a better controlled means of forming the product. An overview of the P/M processing route is shown in Figure 1-1.

This approach does have its own inherent problems. The requirement of a uniform distribution of the reinforcement material is not always readily achieved. In P/M, the procedure generally entails a mixing stage (to achieve a preliminary blend of the matrix and reinforcement material), followed by a consolidation process involving prolonged exposure at high temperatures and possibly high pressures. While some redistribution of the constituent powders may occur during the consolidation step, it is in the mixing stage that the character of the composite will be determined, and it is this step which is the most critical.<sup>1</sup> As in the case of metal-matrix composite systems, mixtures that have two or more constituents possessing significantly different physical properties very often do not mix well, resulting in the formation of regions which have a higher proportion of one or the other constituent powder. In order to properly assess the effectiveness of a mixing operation, it is necessary to identify those operating parameters which yield the undesirable results, and determine the proper combination of these parameters which will give the best mixture. Although much work has been done in large-scale systems to address this problem, little has been done to determine if the observed relationships will apply to powder systems, and especially to those systems of interest in metal-matrix applications.

The main focus of this research, then, is to examine the mixing operation of powders to be used in metal-matrix composite applications, with special emphasis on titanium aluminide materials aimed at high temperature applications. In particular the issues to be addressed are:



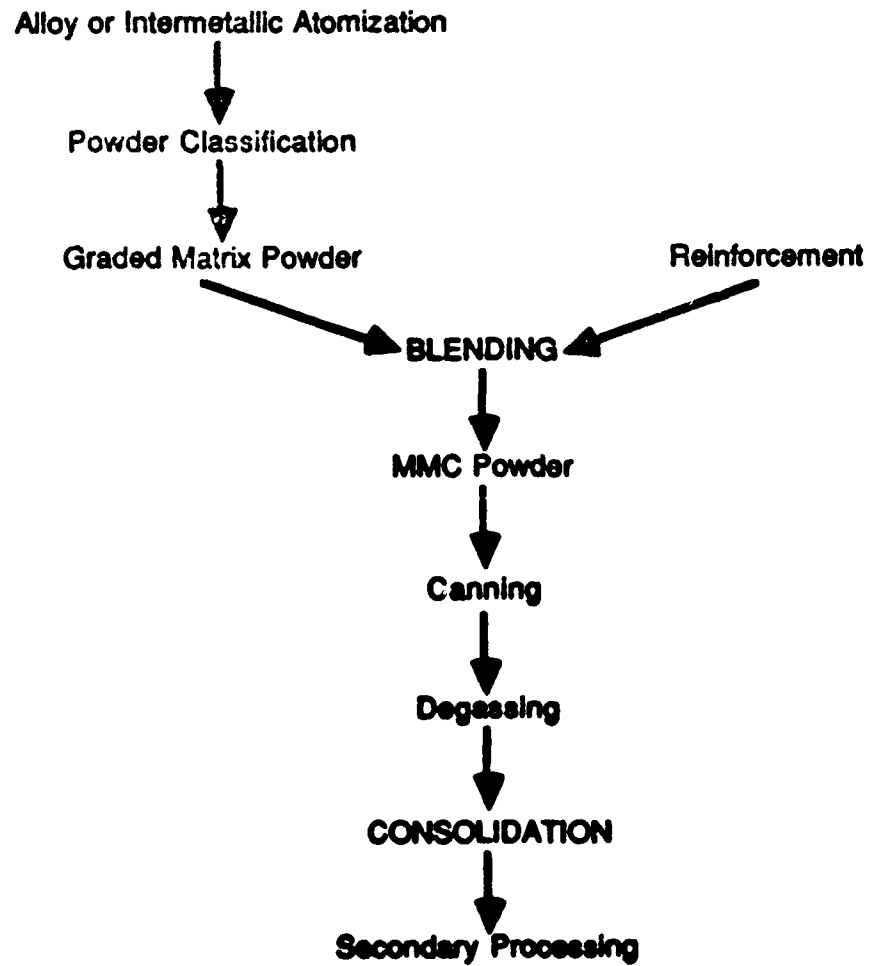


Figure 1-1: Powder metallurgy processing route (adapted from Wills<sup>1</sup>).

1. The development of a fundamental understanding of the mechanisms associated with the blending of MMC powder.
2. A study of the extent that powder characteristics, operating and design variables affect the formation of a disperse-homogeneous MMC powder mixture.
3. Identification of the scale-up criteria for MMC powder blending, using physical modelling criteria.
4. Determination of the relationship between the quality of a blended powder mixture and subsequent consolidation via HIPing.

In the next year, it is expected that a comprehensive study of the first three will be completed. An additional issue to be addressed is that of the importance of ensuring a uniform mixture at the microscopic level. It is not expected, however, that in the time remaining this will be addressed in a comprehensive manner.

The report is divided into two main sections, one detailing a thorough analysis of the literature in the area of mixing and segregation as it applies to MMC systems, and a report on the experimental program adopted, which includes details of the results achieved to date.

---

## Chapter 2

---

### Previous Work

There are a variety of mixer systems available for blending MMC powder. These range from V-blenders and ribbon blenders, where the mixing action is complicated and therefore not easily characterized, to the more simple geometry of the horizontal (and sometimes inclined) rotary blenders. Since in the last case the bed action is relatively uncomplicated and can be controlled, horizontal cylinders are most often used in basic research to determine fundamental mixing and segregation mechanisms. This is due to the fact that the contribution from the various fundamental mixing mechanisms (to be described later) can be controlled in this apparatus. As a result, the current investigation will deal with this system exclusively. In order to determine the best starting point for the current study, previous work must be reviewed and analyzed. While there are hundreds of papers in the literature dealing with the mixing and segregation of particulates and powders, only a small fraction present results relevant to mixing MMC powders. Thus, this chapter will focus on an analysis of the pertinent literature to MMC powder processing by blending. A reasonable starting point is a discussion of the types of bed motion that can be encountered when using horizontal rotary blenders. Next, the literature dealing with pure mixing will be examined, followed by that concerned with segregation. Finally, a review of the effect of changes in the gas atmosphere will be presented.

### 2.1 Bed Behavior

The shape of the bed, the type of bed motion occurring in a horizontal rotary cylinder and the attendant particulate flow patterns for cohesionless solids have been studied experimentally in some detail,<sup>2,3,4</sup> and have been mathematically modelled.<sup>5</sup> The bed motion has been found to be a function of the rotational speed of the cylinder being used, the amount of material present within the drum, the size of the cylinder being used, the static and dynamic angles of repose of the material as well as the particle size. Six specific types of bed motion have been identified, these being slipping, slumping, rolling, cascading, cataracting and centrifuging (see Figure 2-1).

At low rotational speeds or low Froude numbers, the bed may undergo slipping motion. This has been discussed to be composed of three different motions, depending on the specific value of the bed depth or per cent fill, the rotational speed within this regime and the bed wall friction angle.<sup>6</sup> First, the bed

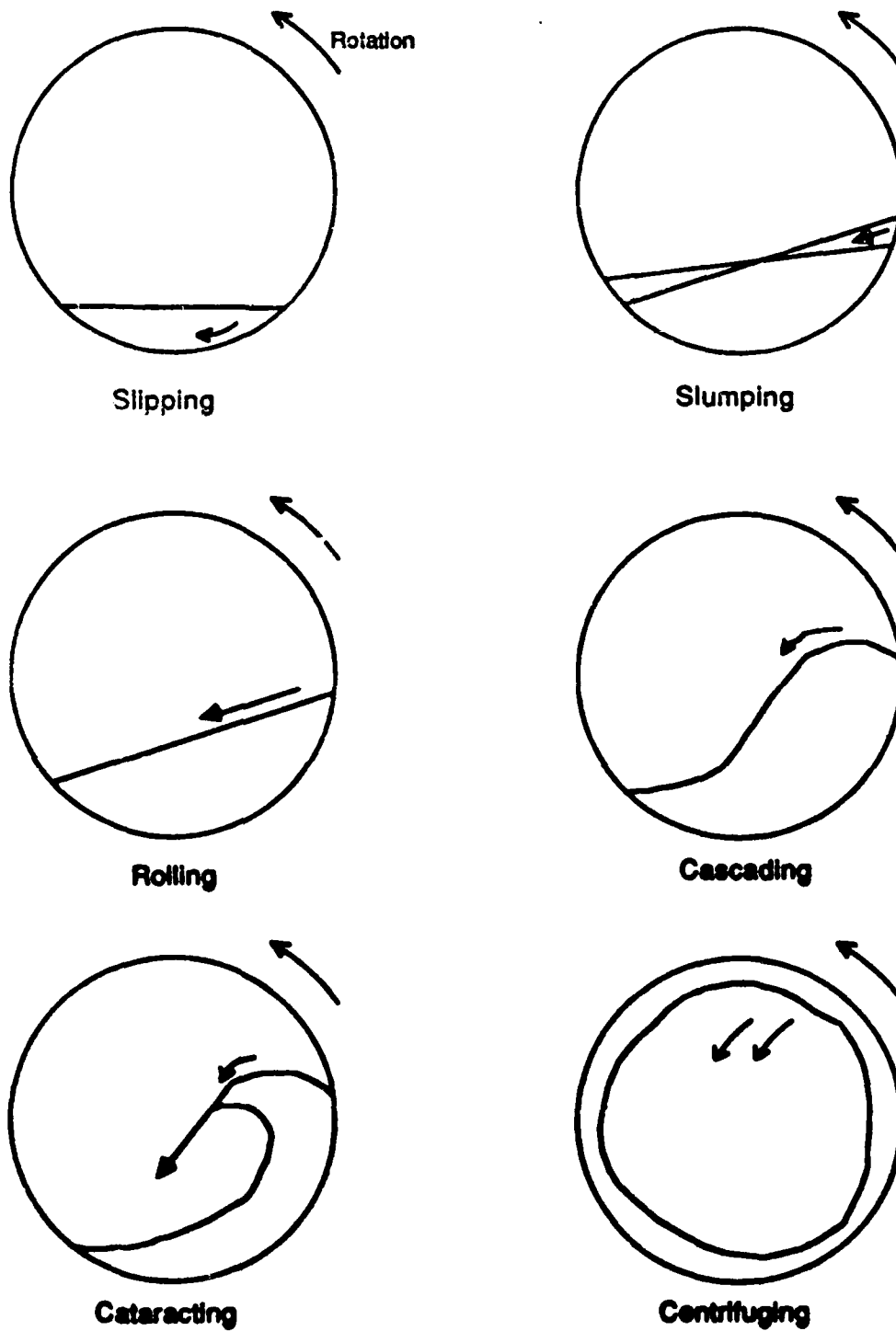


Figure 2-1: Modes of Transverse Bed Motion (adapted from Hensin et al.<sup>9</sup>).

may move as a whole along with the cylinder as it rotates. At the point where the frictional forces along the wall are exceeded (the maximum angle of repose), the entire bed slides down the wall and comes to rest at an angle less than the static angle, from which point the process is repeated. Second, the bed may move with the wall but at a lower rotational speed, with the solids rolling slowly along the free surface of the bed. Finally, the bed may adopt a particular position along the cylinder wall where it is observed to slide continuously. Since slipping results in little relative motion between the particulates, this type of bed motion is undesirable as it results in little mixing. In our experimental work, steps have been taken to ensure that there is sufficient bed/wall friction to eliminate the possibility of the bed slipping.

For higher bed/wall friction and low rpms, motion of the bed would be a slumping mode. This is characterized by the bed moving up with the wall to the static angle of repose, at which point a wedge of solids separates from the bulk of the bed and rolls down the bed surface, resulting in a reduced angle of repose. The process then repeats itself in a regular manner, the slumping frequency being dependent upon the rotational speed of the cylinder, the physical properties of the material and the cylinder diameter.<sup>3</sup>

Further increases in the speed results in a transition to the rolling mode. The bed in this phase of motion is characterized by the continuous motion of the solids over the bed surface. At low rotational speeds, the bed has a flat surface and adopts a constant angle of inclination, known as the dynamic angle of repose. At higher speeds the solids in the upper corner of the bed ride farther up the cylinder wall before detaching, resulting in a kidney-shaped bed cross-section. At this point the bed is said to be in a cascading mode. It is this mode which is generally associated with the best mixing, as the particulates are subjected to the maximum shearing action within the bed.<sup>6</sup>

Increasing the speed past the cascading regime results in cataracting. In this mode the solids detach themselves completely from the wall at the top of the travel. They are then flung through the freeboard of the cylinder, landing on the surface of the bed at some point near the bottom of the bed. Finally, at the point where the inertial forces imparted by the rotation balance the gravitational forces experienced by the bed (the critical speed, with the Froude number,  $Fr = \omega^2 R / g = 1$ ) centrifuging begins. As in the case of the slipping mode, very little mixing occurs due to the fact that there is no relative particle motion in this mode.

It has been clearly shown that the scale-up parameters for bed motion are the Froude number (i.e. the ratio of inertial to gravitational forces), the percent fill of the cylinder, the static and dynamic angles of repose and the particle size.<sup>4</sup> For example, if the same uniformly sized material is placed in cylinders having different diameters and rotated at different RPMs, the same bed motion will be observed at the same Froude number and percent fill.

For the bulk of mixing operations, the useful range of motion exists between the rolling and cascading modes. As will be discussed later, segregation can occur in rolling and cataracting beds where differences exist in the physical properties of the materials. Furthermore, it is important to note that the extent of the regions of the various bed motions changes with the composition of the bed.<sup>7</sup> At a given RPM, the presence of segregation can therefore change both the motion of the bed as well as the degree and effectiveness of the mixing operation. In order to determine optimum mixing conditions, it is not sufficient to observe bed motion with particles of uniform properties or characteristics (i.e. size, shape and density). In order to understand the effect of the bed motion on the segregative behavior of a mixture, the range of motion in the system must be analyzed for the bed mixtures which will be used in segregation studies. However, it would be expected that the scale-up parameters of bed motion of uniform materials properties will also play a role in the bed motion of solids with a range of properties (i.e. size, shape and density).

It should be mentioned here that in all cases (except perhaps the centrifuging mode) the flow patterns in the bed may be divided into three separate regions.<sup>2, 8, 9, 10</sup> This is shown pictorially in Figure 2-2. In the passive region, very little particle motion is observed, and material is transported through this region without changing its position in the bed. The active region of the bed (the "active layer" or "shear layer") comprises a small portion of the bed, usually only a few particle dimensions in thickness. It is in this region that the bulk of the mixing and segregation action occurs, especially at lower rpm's. As will be seen later, the interaction between particles in this layer, voids and even the mixer account for the redistribution of material observed. In some cases (for beds with greater than 50% fill<sup>10</sup>), a "dead-" or "zero-velocity" zone can occur in the bed. Particles which find their way into this area remain trapped here and are removed from further interaction with the remainder of the bed. This zone is of special importance in systems showing segregative behavior, but can also occur in "ideal" systems for certain combinations of the operating parameters. Thus, all experiments in our study were conducted with less than 50% fill.

## 2.2 Mixing

Early work focussed on a determination of the fundamental mechanisms responsible for the mixing action observed in all types of mixers. Lacey was perhaps the first to directly state the mechanisms involved in mixing.<sup>8</sup> These are:

1. Diffusive - This involves the redistribution of particles due to their random motion.
2. Convection - Groups of particles from one location in the solids mass to another.
3. Shear - This mechanism occurs when shear planes are formed or occur within the particulate bodies.

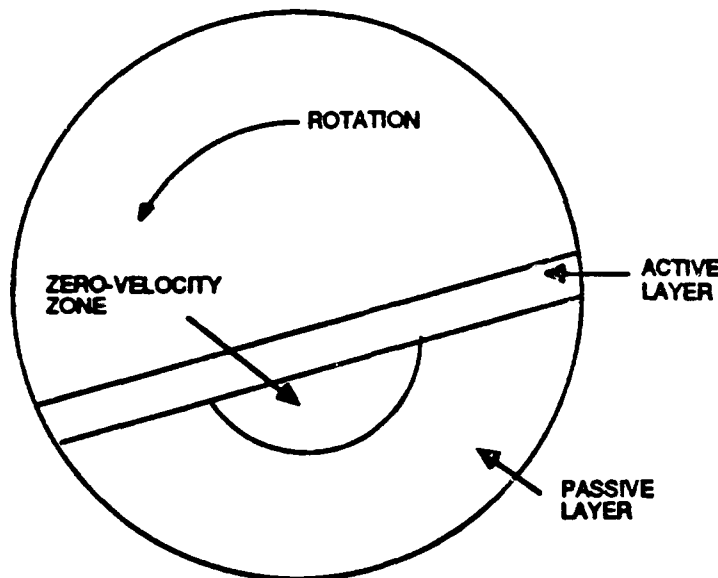


Figure 2-2: Regions of Mixing in the Bed of a Rotary System

In particular, Lacey asserted that in the case of mixing of mono-sized particles in a drum mixer, diffusion was the dominant mechanism in mixing. Diffusive mixing was accomplished by the random scattering of particles over the surface of the bed, and thus the mixing planes were restricted to the surface layers of the bed. It should be noted that this diffusive mixing mechanism was applied to the axial mixing of similar particles. The presence of diffusion as a mixing mechanism has been supported by additional workers,<sup>9, 11, 12, 13</sup> but they revealed the contribution of additional mechanisms that are worth examining in more detail.

Donald and Roseman<sup>12</sup> studied both the axial and radial mixing characteristics of drum mixers. They found that for mixing in the radial direction, mixing occurred as a result of changes in the path of circulation of the particle of the bed. This can be understood in terms of the regions identified in Figure 2-2. They postulated that the particles travelling through the active layers in the bed will fall into voids of the next layer down. When the particle is carried into the passive layer, it should not change its position relative to the mass, and any change in the radial direction should then occur only if the particle travels a different path in the active layers and thus gets trapped at a different position in the passive layer than it occupied originally. The opening of voids and subsequent trapping of the particles in the passive layers was explained to be a result of differences in the velocity between the two bed regions. It was found that mixing was optimized for intermediate values of the operating speed, and that the mixing time was decreased for increased percent fill, showing no variation with the particle size (for beds composed of

mono-sized particles). For axial mixing, they separate the bed into two regions. Away from the end walls of the cylinder, mixing was found to proceed slowly and thus thought to be a result of diffusive processes only. Near the end walls, however, axial mixing was accelerated due to the presence of steep velocity gradients.

Later work by Rutgers<sup>4, 14</sup> also considered both axial and radial mixing. The best radial mixing was found to occur for bed speeds ranging between the rolling and cataracting modes for beds composed of a single particle size. For longitudinal mixing, he again supported the concept that it is the result of random deflections at the surface, with the rate of axial mixing increasing with decreases in the particle size.

Later Cahn and co-workers,<sup>9</sup> again using systems in which the beds were composed of particles with similar physical properties, confirmed the presence of the diffusive mechanism as the mixing mechanism predominating for axial mixing. Again the action was limited to the active layers in the bed (and more specifically the surface of the bed), the diffusion resulting from an axial component to the motion of the particles across the surface coupled with trapping of the particles in voids in the underlying active layers. Subsequent work<sup>11</sup> led to the inclusion of particle-mixer collisions as a contribution to the diffusive mechanism, and efforts to develop a probabilistic model of the particle motion led to reasonable estimates of the 'diffusion' coefficient. Diffusion was found to depend on both the load in the cylinder and the speed of operation.

Work by Hogg et al.<sup>13</sup> and Hogg and Fuerstenau<sup>10</sup> continued to examine the role of diffusion in mixing in rotary cylinders. Hogg et al.<sup>13</sup> refined the diffusion model for axial mixing to include the effect of the presence of the cylinder ends for long mixing times. The modification comes in as a different solution to the diffusion equation for long and short times, for short times the mixing goes as  $N^{1/2}$  (where  $N$  is the number of revolutions), whereas as at long times the mixing proceeds as  $\exp(N)$ . As in the case of the works of Cahn and Lacey, the mixing proceeds as the movement of a plane diffusional front along the axial direction. Radial mixing was considered in the later work.<sup>10</sup> In this Hogg and Fuerstenau proposed that the shear mechanism of Lacey is actually a combination of the convective and diffusive mechanism. In this case, the mixing of material in the radial direction occurs as a result of the interchange of particles between different circulation paths in the bed, and as this exchange is random, it must then be "diffusive". The convective component to the mixing process comes in as a means of reducing the distance over which the diffusion occurs. This results in a striated structure to the bed across the cross-section, with the thickness of the striations decreasing with increasing number of rotations. The convective component was thought to arise from differences in the residence time of particles at different radial positions in the bed. The limitation to this work, however, is that it applies only to the limited "ideal" systems which have been studied. An significant point raised by Hogg in this work, however, is the importance of the considering both macro- and micromixing, i.e., the difference between the combining of separate



components into an apparently well-mixed bed (macromixing) and the short range mixing required between regions rich in one component to regions rich in another. As will be seen in the next section, this has important consequences in P/M MMC applications where the microscopic distribution determines the properties of the final consolidated product.

More recent developments have begun to cast some doubt on the validity of the diffusion mechanism as a means of explaining the observed mixing phenomena. Bridgwater<sup>15</sup> contends that the diffusive process may actually be a purely convective process which, due to the probabilistic nature of the mixing process, appears to be diffusive. Also, Bridgwater indicated that some redistribution of the particles may occur at a particle to particle (or 'micro-') level in the passive region of the bed, and that this redistribution is likely not a result of any diffusive process. Later work by Scott and Bridgwater<sup>16</sup> proposed a different mechanism for mixing to occur to account for this micro-distribution. They envisage the bed as a series of 'convective blocks' surrounded by failure zones. These convective blocks account for macroscopic movement of the particulate materials, whereas mixing at the microscopic level would occur as a result of interparticle percolation. They predict that this mechanism would become important for particles greater than 30  $\mu\text{m}$ , and be commonplace for mixtures with particle sizes greater than 100  $\mu\text{m}$ . Their work indicated that the application of strain to the shear zones, resulting in expansion of the bulk sufficient to allow particles to pass through voids between other particles, allowed percolation to proceed, and that the rate of mixing due to this mechanism depended on the amount of strain imposed on the material and the relative volumes of the constituent particles (the density having been found to be unimportant).

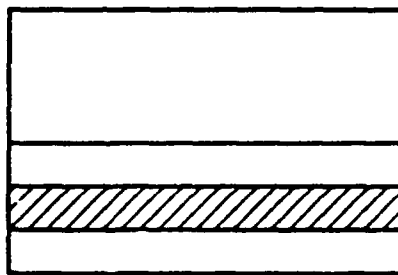
It is important to realize the previously mentioned works represent only a small portion of the available literature on mixing, much work having been done to evaluate the efficiency of industrial systems and alternative mixers. It is also notable that in all of the cases, the bulk of the work was performed on systems in which the particles showed no significant differences in physical properties (size, shape, density, etc.) and thus are limited in their usefulness to the understanding of real systems where such ideality in the particle properties rarely exists. The discussions above have focussed on some of the more important studies looking at the fundamentals of the mixing process, especially that applied to rotating cylinder mixers. These studies clearly outline the mechanisms by which particles flow in mixers. In systems with tendencies for segregation, the mixing mechanisms described above will still be present. The extent to which they will contribute to the final state of the mixture will depend on the segregative tendencies of the mixture. It is thus important to study the literature dealing specifically with non-ideal systems. This is done in the following section.

## 2.3 Segregation

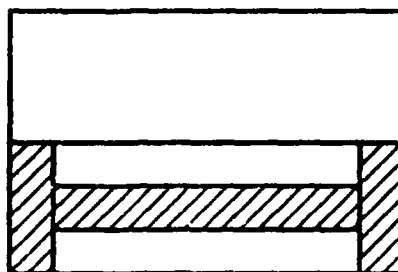
Detailed investigations into the mixing properties of beds containing particles of non-uniform physical properties originated in the sixties with the work of Donald and Roseman<sup>12, 17</sup> and Campbell and Bauer<sup>2</sup>. Donald and Roseman reported the formation of segregated regions in the bed of a rotating cylinder for cases where significant differences in the physical properties of the constituent particles existed. In their case, they considered only differences in either the size or density of the materials used. They found that segregation could occur in both the axial and the radial directions, and that the final shape of the segregated regions depended on the static angle of repose of the materials being used. For the case where the segregating material (the smaller or denser material) has the lower angle of repose, and considering a situation where there are negligible end effects, a segregation core forms along the length of the cylinder at some point below the active layer of the bed (see Figure 2-3 (a)). When end effects become important, such as in the case of increased speed and/or rough walls, the core at the ends of the cylinder become unstable and small regions of banding perpendicular to the cylinder axis may form at the ends, as shown in Figure 2-3 (b). Finally, for the case where the segregating material has the higher static angle of repose, the bed will form only bands along the length of the cylinder (Figure 2-3 (c)). Their explanation for these effects lies with the fact that changes in the angle of repose will affect the velocity which the material sees as it travels down the surface. For low angles of repose, the material will have a low velocity along the surface, and thus the chances that it can drop through the active layers without being scattered axially increases, and thus the radial segregation core may be formed.

Donald and Roseman also investigated the role of material and process variables on the segregation phenomenon. They found that for density and size ratios greater than 1.2, segregation occurred rapidly and the final form of the mixed bed was one of the configurations explained above. Contrary to some of the ideas of Rose,<sup>18</sup> Donald and Roseman also found that the formation of the segregated regions did not depend on the initial position of the components. Also, they determined that the rate at which segregation occurs decreases with increasing percent fines (for particles differing in size) and would be slowest for equal volumes of coarse and fine particles. This was due to a decrease in the number of free voids available for the smaller particles to fall into. Finally, they observed that the shape of the material had apparently little effect on the segregative behavior when compared to size and density differences. It isn't clear what actual size of materials was used in this study, however, it will be seen later that shape effects can be important for fine materials (powders).

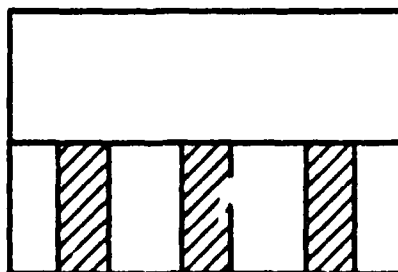
Campbell and Bauer<sup>2</sup> extended some of these concepts to examine the effect of changes in the particle shape on the segregative behavior. They confirmed the ideas of Donald and Roseman that the degree of segregation encountered depends on the size ratio of the particles being mixed. They expressed their observations, though, as the volume ratio of the particles being mixed. In considering the effect of changes from spherical particles to needle-like particles, they used the weight of individual



(a).



(b).



(c).

Figure 2-3: Segregated region formation (adapted from Donald and Roseman<sup>12</sup>).

particles to determine an equivalent spherical volume for the acicular materials. They then found that for mixtures of acicular and spherical particles, segregation was minimized for those cases where the equivalent spherical volume was equal to the volume of the spherical particles. Thus the volume of the particles was found to be the determining factor in segregation, rather than the shape. Also, Campbell and Bauer determined that the density differences were minor when compared to differences in the volume of the materials being mixed. This was, however, for a density ratio of only 1.26, which is very near the limit stated by Donald and Roseman for the density to have an effect on the segregation.

Later work by Ulrich<sup>19</sup> considered that two segregative tendencies would dominate, that due to size differences and that due to density differences. Using steel and glass balls, he determined that a segregated core formed along the cylinder axis, composed of the finer (or denser) material. The experiments were restricted to consider the effect of changes in the size ratio and operating speed (expressed as  $\omega^2 R/g$ ) only (although no effect of changes in the drum speed were reported). He was able to show that to some extent the tendency to form a segregated core can be minimized by making the denser particle larger than the other. For a size ratio of denser:finer of 1.4:1, segregation was minimized. He also pointed out, however, that at the point of minimum segregation, the mixture could not be considered to be stochastically well-mixed. This implies that elimination of segregation is likely to be very difficult, and that macroscopically well-mixed beds may still show significant segregation at the microscopic level.

Rogers and Clements<sup>20</sup> looked at the effect of the rotational speed in more detail, for mixtures of coarse granular materials (500-600  $\mu\text{m}$ ). For low rpm and short operating times, a segregated core was observed along the length of the mixer. As the operation time was increased, the fines were seen to move towards the ends of the mixer, resulting in large cores at the ends of the mixer, and a fines-depleted region in the center. Increases in the rpm led to more band formation, with the number of bands increasing for increasing rpm. The percent fines was observed to affect the size of the bands formed, but only at higher rpm. Rogers and Clements also noted that even for systems with similar physical properties between the particles, segregation can still occur, despite the fact that the bed may appear to be visually homogeneous. This again implies that segregation on a microscopic scale is important.

This last point was borne out by the work of Sauer.<sup>21, 22</sup> Using iron and copper powders in size ranges typical to powder metallurgy applications ( $\sim 60 - 200 \mu\text{m}$ ), Sauer was able to look at the effect of particle properties on mixing at both the macroscopic and microscopic level. Sauer deduced that macroscopic segregation in these systems occurred for both differences in the density as well as differences in the size, primarily due to the changes in the kinetic behavior of the particles resulting from differences in the mass of the individual particles. Sauer also credits part of the segregation resulting from size differences to the fact that the smaller particles may fall into voids in the charge. Again

segregation was seen to increase with increases in the size ratio, and size variations accounted for more of the observed segregation than did the variations in density. Sauer also showed, however, that the shape of the particles affected the mixing and segregation processes in these materials. Increased surface interference between irregular particles was found to reduce the rate at which segregation occurred, and this effect increased with decreases in the overall particle size due to the attendant increase in the surface area. At the microscopic level, it was found that the size ratio had qualitatively the same effect as in the macroscopic case. In this case, however, the absolute size and shape of the particles determined more critically the distribution observed. Sauer found that as the particle size decreased, the distribution became worse, but that this could be minimized somewhat by the addition of an appropriate mixing additive. Also, it was shown that if even one of the components of the bed has an irregular shape, good mixing at the microscopic level was not achieved. This obviously has important consequences for MMC applications, where the reinforcement phase is not likely to be spherical with a smooth surface.

To this point little has been said as to the mechanisms governing the segregation process. Most of the above work relied on traditional interpretations of the phenomena governing the motion of the particles (i.e. the motion being governed by convective and diffusive mechanisms). Williams asserts, however, that in segregative processes, different mechanisms govern the motion of the particles<sup>23</sup>. He states more formally that segregation can result from four factors, these being:

- differences in particle size
- differences in particle density
- differences in particle shape
- variations in particle resilience

In these cases the motion of the particles will be governed by the following mechanisms:

1. Trajectory or flow segregation - In which segregation occurs due to differences in the distance over which the particles travel on the surface of the bed.
2. Percolation - as described in the section on mixing, this involves the motion of particles through voids in the bed. This mechanism has been alluded to in the previous work on segregation, though never formally addressed as a mechanism for the segregation.
3. Vibration - In which motion of particles through the bed occurs due to variations in the bed voidage resulting from externally imposed vibrations. This mechanism is of little importance in rotary cylinders.

The role of the first two mechanisms has been addressed in very few studies. The most notable involve

the work of Henein et al.<sup>7</sup> and Nityanand et al.<sup>8</sup> In examining the segregation behavior of a model rotary kiln system, Henein et al. found that segregation occurred both axially and radially, and in particular, for bed motions in the slumping and rolling regimes. The segregated core was found to have the same general shape as the bed, and lay at some point below the active layer, though usually in the top half of the bed. Based upon their observations of the formation of the core, they postulated that it could not have formed as a result of any convective or diffusive process, and proposed that the percolation mechanism was primarily responsible for the segregation process. They also allowed for some contribution of the trajectory mechanism, though considered it to be of minor importance.

In the work of Nityanand et al.<sup>8</sup> the goal was to determine the rate at which segregation proceeded, and to see if percolation was indeed responsible for the formation of the segregated core. Using model materials, the observations of Henein et al. as to the shape and location of the bed were confirmed for a more general case. Segregation was again found to occur for slumping and rolling beds, and for rolling beds the segregated core was located just below the active layer. Direct measurement of the formation of the core indicated that the kinetics of formation followed zero order kinetics, with the kinetics a linear function of the rotational speed, and independent of the percent fill and bed depth. This is not consistent with either a diffusive or convective mechanism, and direct observation of the bed confirmed that the fines reported to the core by means of percolation. The presence of flow segregation could not be discounted, however, since the number of coarse particles present in the core was less than was expected. Since percolation cannot account for the removal of coarse particles from the core, flow segregation must still be operative. The rate of segregation increased with increasing size ratio, and also increased with increases in the size of the cylinder. This led to the development of the size ratio and the dimensionless speed  $\omega^2 R/g$  as scale-up criteria for segregation phenomena. This should allow comparison of results of macromixing investigations of powder systems to these larger systems to determine whether percolation dominates for the smaller systems, and also to determine the relative importance of additional effects such as the shape difference and increased surface area.

## 2.4 Effect of Gas Atmosphere on the Flow Properties of Powder Beds

Recent work has indicated that a complete analysis of powder operations requires an understanding of the interaction between the gas atmosphere in the apparatus of interest and the powders. This interaction depends not only on the properties and state of the gas (i.e., gas viscosity  $\mu$  and pressure), but also on the properties of the powders involved (powder density and particle size) and the typical operating speed of the apparatus itself. In essence, the effect of the gas atmosphere is to change the state of fluidization of the powder bed, thus altering the flow characteristics and properties of the powder bed.

In determining the extent to which the gas has an effect of the flow properties of the bed, Platema<sup>24</sup>

considered the hydrodynamic interactions between the gas and the powder mass. He reasoned that in cases where the typical velocity of the powder-handling apparatus exceeded the rate at which the entrapped gas could escape the bed, the powder would remain fluidized and in an expanded state. The removal of the gas from the bed can be followed as the movement of a "continuity shock wave", above which the porosity of the bed is that of the expanded state, and below which the porosity is that of the settled bed,  $\epsilon_0$ . The velocity of the shock wave is given by the expression

$$V_{CS} = \frac{\rho_d d_p^2 g}{150 \mu} \frac{\epsilon^3}{(\epsilon - \epsilon_0)}$$

In this expression,  $\rho_d$  = the powder density,  $d_p$  = the powder particle size,  $g$  = gravitational acceleration,  $\mu$  = the gas viscosity and  $\epsilon$  = the porosity in the fluidized portion of the bed. For a typical powder handling speed  $V_a$ , the bed can be expected to remain fluidized for conditions where  $V_a \gg V_{CS}$ . Rietema then uses this condition to arrive at an expression for predicting the influence of a gas atmosphere, the so-called Gas Interaction Number,  $N_1$ . The expression for this number is

$$N_1 = \frac{\rho_d d_p^2 g}{\mu V_a} \ll 100$$

The physical significance of  $N_1$  is as follows: for values of the gas interaction number less than 100, the gas atmosphere will remain trapped in the powder mass. This effect increases for decreasing values of the gas interaction number, i.e., the lower the value of  $N_1$ , the greater the influence of the gas. From the form of the equation, it can be seen that low values of  $N_1$  can be achieved for large values of both the gas viscosity and the powder-handling apparatus speed. The effect of the speed of the apparatus can be readily understood, as it arises from the derivation of the expression. If the speed of the apparatus is low, the  $V_a$  will be less than  $V_{CS}$  and the gas will be able to leave the powder mass. The porosity of the powder bed will remain close to  $\epsilon_0$  and there will appear to be no gas effect. As  $V_a$  increases and becomes larger than  $V_{CS}$  the gas will remain trapped in the bed. The pressure exerted by this entrapped gas will then cause the powder bed to expand, and the bed will thus flow more readily.

The influence of the viscosity of the gas can be explained in the following manner. For increases in the gas viscosity, the momentum exchange between the gas molecules is large. This results in increased force on the powder particles, and thus the observed increase in the interaction between the gas atmosphere and the powder mass. As the viscosity decreases the mean free path,  $\lambda$ , increases and the number of gas molecule collisions decreases. This results in a lower rate of momentum transfer, and thus a decreased interaction between the gas and the powder. For low values of  $\mu$  and  $V_a$ , then, the bed will be collapsed and relatively static, as compared to its free flowing behavior for large values of these two variables. The effect of changes in both the viscosity and the speed can be seen graphically in

Figure 2-4. The values of the variables used are shown in Table 2-1, and correspond to quantities which might be encountered in metal-matrix composite applications. It can be seen that the value of  $N_1$  remains well below 100 even for relatively high speeds and low viscosities. The effect of variations in the particle size can be seen in Figure 2-5. The increasing viscosity here corresponds to the same range as the previous figure (see Table 2-2 for the values used). It can be seen clearly in this case that changes in the rotational speed have a significant effect on the gas interaction behavior. It is apparent that at low rpms, the bed will be fluidized for small particles only. As the rotational speed is increased, the fluidizing effect of the atmosphere is extended to include the larger particles. For a rotational speed of 100 rpm (which is a reasonable number for the cascading regime in these blenders) it can be seen that, for a system with all particles less than 100 microns (a typical situation for the experiments to be conducted in this work) the entire bed will be fluidized. Thus it is expected that the kinetics of mixing in this regime will be enhanced for all the particles in the system. At the lower speeds, where segregation is usually a problem (the powders which will be studied are expected to be strongly segregating), it appears that the smaller reinforcement particles could be fluidized, but that the larger matrix particles would not. This could have some as-yet unknown and interesting effects on the nature and extent of segregation observed. Thus it will be necessary to take into account the effect of the atmosphere in any of the experiments conducted, and a determination of the best atmosphere to minimize segregation will be an important aim of this research.

It is reasonable to assume that the pressure of the gas will also have some effect on the behavior of the powder bed. It is not apparent from the previous expressions, however, how the changes in the pressure should affect the bed behavior. If one were to assume that the viscosity in Fletema's expression is the absolute viscosity, then its value would change very little with pressure, and the gas interaction number could not be used to predict the influence of the atmosphere for changes in the pressure. In a later paper, however, Cottar and Fletema<sup>25</sup> did consider the effect of a change in the pressure. They looked at two cases: first, the case where  $\lambda$  is much smaller than some critical dimension  $R$  (for powder masses, this would correspond to the size of the interparticle voids); and secondly, the case where  $\lambda > R$ . They develop their arguments based on considerations of the force  $F$  exerted by a flowing gas at speed  $U$  on a tube of length  $L$  and radius  $R$ .

The first case corresponds to the case of viscous flow in the tube. In this case the result can be readily obtained from fluid mechanics with the result that

$$\frac{F}{L} = 8\mu_1 U$$

Here  $\mu_1$  corresponds to the viscosity of the gas at high pressure. As mentioned, this is for the case of  $\lambda \ll R$ , and thus an expression for the gas viscosity can be obtained from the kinetic gas law, based on



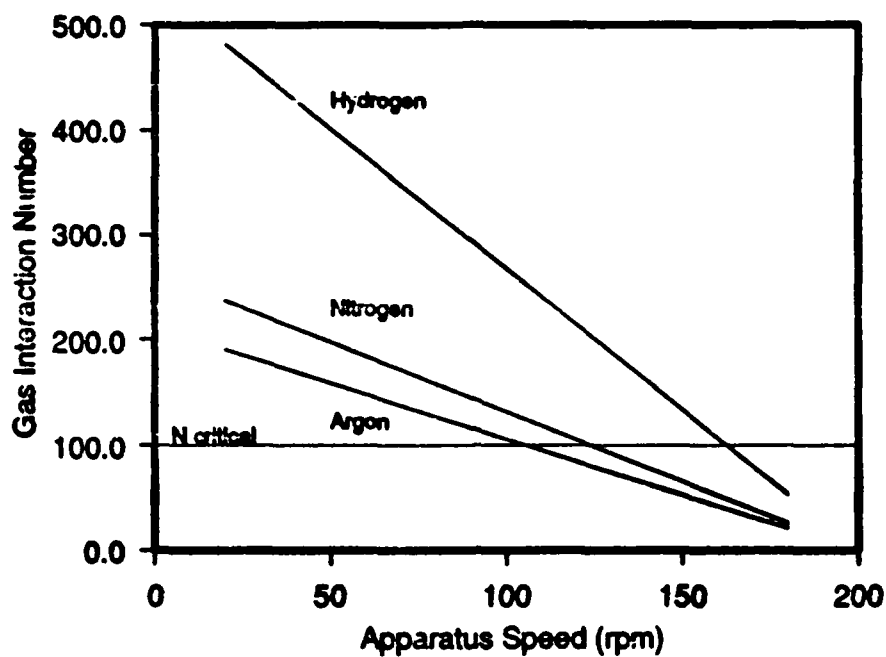


Figure 2-4: Effect of Apparatus Speed ( $V_a$ ) and Viscosity ( $\mu$ ) on the Gas Interaction Number

Table 2-1: Data for Calculation of  $N_1$  as a Function of the Apparatus Speed

$d_p$	$1 \times 10^{-4}$ meters
$\rho$	4500 kg/m <sup>3</sup>
$g$	9.81 m/s <sup>2</sup>
$\mu$	$2.217 \times 10^{-3}$ kg/ms
	for Ar at 20 °C and 1 atm
	$1.781 \times 10^{-3}$ kg/ms
	for N <sub>2</sub> at 27.4 °C and 1 atm
	$8.76 \times 10^{-4}$ kg/ms
	for H <sub>2</sub> at 20.7 °C and 1 atm

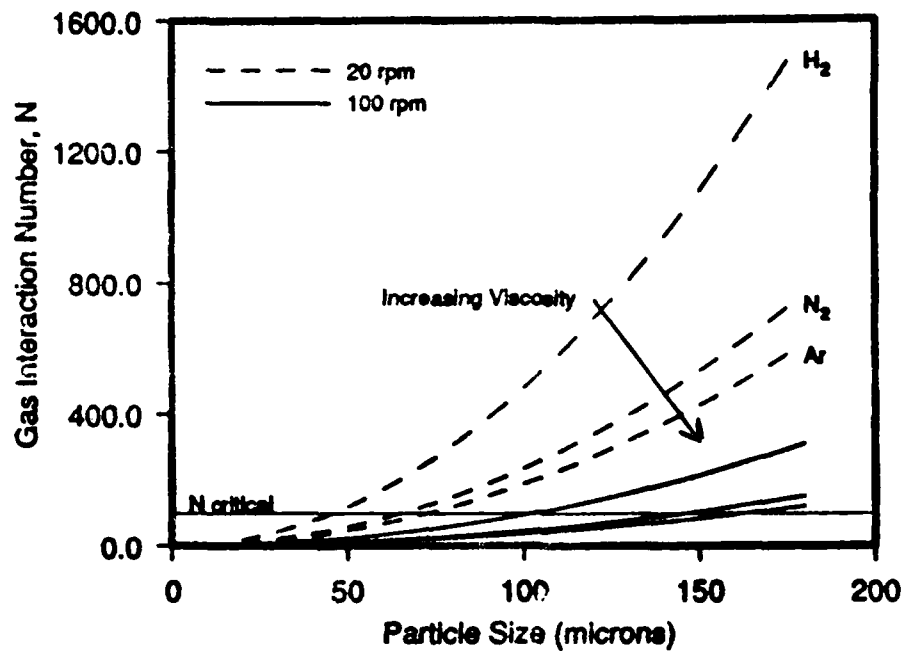


Figure 2-5: Effect of Particle Size ( $d_p$ ), Viscosity ( $\mu$ ) and Apparatus Speed ( $V_o$ ) on the Gas Interaction Number

Table 2-2: Data for Calculation of  $N_i$  as a Function of the Particle Size

$d_p$	$2 \times 10^{-5}$ meters to $1.6 \times 10^{-4}$ meters
$\rho_p$	4500 kg/m <sup>3</sup>
$s$	9.81 m/s <sup>2</sup>
$\mu$	$2.217 \times 10^{-3}$ kg/ms for Ar at 20 C and 1 atm $1.781 \times 10^{-3}$ kg/ms for N <sub>2</sub> at 27.4 C and 1 atm $8.76 \times 10^{-4}$ kg/ms for H <sub>2</sub> at 20.7 C and 1 atm
$V_o$	20.0 rpm 100.0 rpm

the assumption that the viscous forces will arise predominantly from momentum exchange between the gas molecules and not from interactions between the gas and the tube walls. In this case the expression for the viscosity is

$$\mu_1 = \frac{1}{2} \rho \lambda v_t$$

where  $\rho$  is the gas density and  $v_t$  is the thermal velocity of the gas molecules (i.e., the actual velocity of the gas molecules for the temperature at which the gas is held). The quantity  $\rho \lambda$  is independent of pressure and thus the viscosity at high pressures remains at a relatively constant value.

For the case of gases at low pressure (and thus large  $\lambda$ ), Cottrell and Rietema consider the situation as one representing free molecular flow. The momentum exchange of one molecule is thus considered. For molecules of mass  $M$ , and assuming that the wall and molecules are in thermal equilibrium so that the momentum exchange due to thermal velocity is on average zero, the net momentum exchange for the molecule will be  $MU$ , where  $U$  is again the gas flow velocity. Since the gas molecule will on average travel over a maximum distance of  $R$  between collisions, the total number of effective collisions becomes  $L/R$  and the total force per unit length becomes

$$\frac{F}{L} = \pi \rho U^2 R$$

From this a new expression for an apparent viscosity  $\mu_2$  was obtained, given as

$$\mu_2 = \frac{1}{8} \rho R U$$

Thus the effect of gas pressure can be seen as a modification of the value of the viscosity. This effect is two-fold. First, the distance that a molecule travels changes from the value of  $\lambda$  for the particular conditions experienced by the gas, to the size of the opening through which the gas is forced to pass. Secondly, the velocity at which the gas moves decreases from the value of the thermal velocity to the value of  $U$ , which is typically several orders of magnitude smaller than the thermal velocity<sup>25</sup>. Thus, as the pressure of the gas is decreased, the apparent viscosity of the gas is reduced. In terms of its effect on the gas interaction number, then, as the pressure of the gas decreases, the value of  $N_1$  will increase. This indicates that the effect of pressure is similar to that of viscosity: for beds that show fluidized behavior, the extent of fluidization and thus the ease of flow of the powder mass decreases with decreasing pressure (and decreasing apparent viscosity). An additional point is that since the value of the apparent viscosity is a function of  $R$ , and  $R$  is of the order of the interparticle spacing, the particle size has a role in determining the value of the interaction number directly (due to its presence in the expression for  $N_1$ ) and indirectly, inasmuch as it changes the value of the apparent viscosity.

Experiments have been performed to determine how changes in the gas atmosphere affect the performance of ball milling<sup>25, 26, 27, 28</sup> and mixing<sup>29</sup> operations. The behavior predicted by the gas interaction number was found to be observed in all cases, i.e., for high values of either the gas pressure or the gas viscosity, and thus low values of  $N_1$ , the beds were observed to be very fluid, with good intermixing of the powders in the bed. For the studies on milling operations, it was found that the rate of breakage of the product increased with increases in pressure and  $\mu$ . The uniformity of the end product increased, with less fines being produced, and the number of agglomerates formed during the milling operation decreased. Thus for the case of milling, improvements in both the quality and efficiency of the operation can be achieved with the use of either highly viscous gases or high gas pressures.

In the mixing studies, systems of similar particles (differing only in color) and systems showing segregative behavior were considered. In the first case, using variance as a measure of the progress of the mixing operation, it was found that an increase in the powder mobility (again, due to increases in either the pressure or the viscosity) resulted in increases in the diffusion coefficient (i.e., the rate at which random movement of the particles occurs) of the process, as well as decreases in the variance in the sample. Since the mixture of similar particles is a random process, this improvement in the mixing process is a reasonable one. In the case where the samples showed a tendency to segregate during mixing, it has been found that the opposite conditions were beneficial, i.e., low gas pressures and low viscosities resulted in a decrease in the mobility of the powders and thus reduced the tendency towards segregative behavior. Again the improvements were demonstrated by a decrease in the variance of the measured samples of the mixtures considered. In terms of the gas interaction number, then, high values of  $N_1$  will be beneficial in reducing the extent of segregation observed in those systems predisposed to its occurrence, whereas low values of  $N_1$  will benefit those operations which rely on increases in the rate of occurrence of random particle movements (pure mixing).

## 2.5 Summary

It is obvious from the brief descriptions above that a complete assessment of the success of a blending operation is a difficult task. Identification of the dominant mode of particle movement can be expected to be obscured by overlying observations of segregation when materials of differing physical properties are involved. The situation is further complicated by the role of the circumambient gas in the drum, which can markedly alter the kinematics of the bed motion, and thus the degree of mixing and segregation which occurs. Also, the conditions which can lead to apparently good macromixing will not necessarily lead to a proper microdistribution of the components, which is of great importance in creating a suitable final product for composite applications. The benefits of the previous work on large scale materials, however, is in providing a framework from which to begin an analysis of mixing using fine powder materials. The concept of similarity may also allow an identification of the contribution from

additional small particle forces (van der Waals, electrostatic, etc.) in the event that the dynamics and mechanisms of mixing and segregation are found to be comparable in the case of small versus large particles.

## Experimental Apparatus and Program

The research program was divided into two main areas. First, investigations were performed on model materials to examine the relationship between operating parameters and the segregation behavior in rotating cylinders. By comparison of these results with parallel studies performed on powders, it is hoped that the effect of traditional variables such as size, density and rotational speed can be separated from any effects peculiar to powder systems (such as shape, surface roughness, etc.). In both cases, macromixing will be the primary focus, with the issue of micromixing in the powder systems being addressed if there is enough time.

### 3.1 Model Materials

#### 3.1.1 Experimental Setup

The schematic of the experimental set up is shown in Figure 3-1. An aluminum cylinder of diameter and length 20 cm was mounted on two rollers, one of which was driven by a variable speed electric motor. With this arrangement the cylinder speed could be increased to a maximum of 140 rpm. A rough fabric was used to line the inside surface of the cylinder to eliminate slippage between the particulates used and the cylinder wall. Observations of the bed behavior was made from one end of the cylinder which had a transparent glass plate attached to it. The model materials used were monosized spherical particles of four different sizes, and two different densities. The size ratios of the model materials were chosen between 1.3 and 3.04 (also see Table 3-2), which was within the range of that available for the MMC materials. The model materials were also chosen, so that their density ratio (1.8) was within the range of that available for the MMC systems. Table 3-1 summarizes the physical properties of the two materials used.

#### 3.1.2 Experimental Variables and Procedure

The following operating variables were tested using the model materials:

1. Size ratio -  $d_{\text{coarser}}/d_{\text{finer}}$

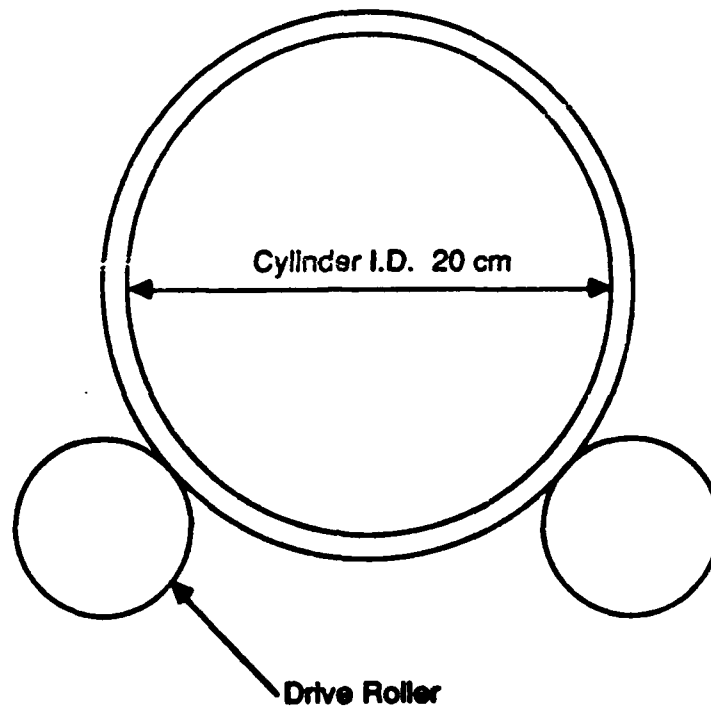


**Figure 3-1: Equipment Schematic for Model Experiments**

**Table 3-1: Model Material Characteristics**

Material	Size (mm)	Density (g/cm <sup>3</sup> )	Shape
Acrylic	9.5	1.3	Spherical
	6.4		
	4.0		
	3.1		
Alumina	3.1	0.72	Spherical

2. Percent fill -  $(V_{mixture}/V_{cylinder}) \cdot 100$

3. Percent fines -  $(V_{fines}/V_{mixture}) \cdot 100$

4. Density Ratio -  $\rho_{coarser}/\rho_{finer}$

5. Cylinder Speed (RPM)

Table 3-2 provides a list of the operating variables that were tested. The following portion of this section outlines the important parameters and the basic procedure used in the different sets of experiments that were performed with the model materials. The bed behavior and macro-segregation or mixing patterns that were observed during these experiments is discussed in detail in the next section of this report.

1. First Set - Binary mixtures of acrylic spheres (with density ratio of 1.0) with 35% percent fill and 14% fines were used in this set. With these parameters fixed, six binary mixtures ranging in size ratio between 1.3 and 3.04 were each tested. In each case, the cylinder speed (RPM) was increased from 0 rpm to a maximum of 140 rpm, and the bed behavior, macro-segregation or mixing were observed.
2. Second Set - These experiments were very similar to the first set, except for the fact that the speed was decreased from the maximum speed of 140 rpm to 0 rpm. This set was therefore intended to provide comparisons between increasing and decreasing cylinder speeds, all other parameters being fixed.
3. Third Set - Experiments performed here were very similar to the first set, except for the percent fill and percent fines used, which were changed to 37% and 20% respectively. This gave a direct comparison between cases with varying percent fines.
4. Fourth Set - Here mixtures of acrylic and alumina spheres were used (with density ratio 1.8). The percent fill and percent fines were fixed at 35% and 14% respectively as in the first set, and three binary mixtures with size ratios 1.3, 2.1 and 3.04 were studied in this set. The results of this set when compared with the first set, would therefore, provide the differences in the segregation for mixtures varying in density ratios.

In each case, the cylinder was loaded with a measured quantity of the binary mixture and was well shaken to form a randomly mixed bed. The cylinder was then placed on the drive rollers and the speed was either slowly increased from 0 rpm, or slowly decreased from 140 rpm depending on the set of experiments performed. The flow of the fines were observed in each case.



Table 3-2: Experimental Variables

Materials	Size Ratio	Density Ratio	Percent Fill	Percent Fines
Acrylic/Acrylic	3.04	1.0	35	14
	2.4		37	20
	2.1			
	1.6			
	1.5			
	1.3			
Acrylic/Alumina	3.04	1.8	35	14
	2.1			
	1.3			

### 3.1.3 Results and Discussions

Figure 3-2 shows the typical behavior that was observed at progressively increasing speeds. At low speeds a central segregated core made up of the fines was formed, by rotating the cylinder at a constant speed for a few seconds. This behavior was observed for each case tested (see Figure 3-2 a,f,k). On further increasing the cylinder speed, the fines began to disperse gradually to the other parts of the bed (see Figure 3-2 b,g,l). This dispersion of the fines promoted mixing of the fines in the bed. However, even distribution of the fines throughout the bed did not occur at any particular speed but occurred over a range of speeds. The range of speeds over which the fines were evenly distributed throughout the bed is defined as the transition zone from core segregation to mixing. The lowest speed at which the fines dispersed from the center and began to mix with the other parts of the bed marked the beginning of the transition zone. Starting at this speed, the motion of the cylinder was arrested at various speeds to observe the distribution of the fines in the bed. The end of the transition zone or the beginning of the mixing zone was determined by this procedure. Once this was determined, the cylinder speed was further increased, and mixing continued (see Figure 3-2 c,h,m) until the larger particles began to move towards the center of the cylinder. This determined the beginning of reverse segregation. As the speed was further increased, reverse segregation continued (see Figure 3-2 d,i,n) until the fines began to form a monolayer against the inner wall of the cylinder. This speed marked the beginning of centrifuging (see Figure 3-2 e,j,o), and the cylinder remained centrifuged with any further increase in the rotational speed. The boundaries of the various zones (core segregation, transition, mixing, reverse segregation and centrifuging) were thus determined in each case. This procedure was repeated seven times for each size ratio in each set, and the speeds which determined the boundaries of the various zones were typically within two standard deviations ( $2\sigma$ , where  $\sigma$  varied between 0.5 and 3.1 rpm) of the mean speed calculated in each case, indicating that the experimental error is within acceptable limits. The photographs shown in Figure 3-2 provides a good representation of the bed behavior that was observed

visually. This figure shows that the bed behavior at low, high and intermediate speeds were similar in each case, except that the boundary speeds varied with size ratio. These observations provided information on the mixing patterns when the speed of the mixer is increased, starting with a segregated bed. The results discussed so far were similar for the first, third and fourth set, showing that the variation in percent fill, percent fines and density ratio did not make any qualitative difference in the mixing patterns for binary mixtures.

The second set of experiments were performed to study the effects of decreasing the speed, starting with a centrifuged bed. In this case, the bed behavior changed from centrifuging, to reverse segregation, to mixing, to transition, to core segregation. However, the overall results in this case was similar to the other cases, and is discussed later in this section.

From previous work discussed in Chapter 2, it can be seen that a non-dimensionalized number,  $\omega^2 R/g$  provides a useful means of expressing the important parameters. Therefore, the results for each set of experiments are expressed in terms of plots of  $\omega^2 R/g$  versus Size ratio. The results of the experiments with acrylic/acrylic mixtures are shown in Figures 3-3 and 3-4. The zones on either side of the mixing region can be classified as the segregated regions. The figures show that at very low and very high speeds the bed is segregated, and at intermediate speeds thorough mixing occurs. The figures indicate that at a size ratio of 1.3 (mixture of 4.0 mm and 3.125 mm diameter spheres), not only is the mixing zone shifted towards the right indicating that mixing begins at higher speeds, but the mixing zone is larger as well. At size ratios above 1.5, there is very slight variation in the transition boundary (variation of about 43 to 46 rpm, between size ratios of 1.5 and 3.04). Previous work done by Roseman and Donald<sup>17</sup> indicates that up to a diameter ratio of 1.2, the smaller particles cannot slip through the voids of the larger particles, which results in very little segregation. A similar effect is seen from our data, which shows a larger mixing region for a mixture of diameter ratio 1.3. Our results also show, that the width of the mixing zone decreases with increasing size ratio. It is also seen that centrifuging occurs at  $\omega^2 R/g$  greater than 1.0. This could be due to some amount of slippage that exists between the cylinder inner surface and the spheres. It can also be noted that for a given larger particle size, the speed at which centrifuging occurs increases with the size of the smaller particles. The speed at which centrifuging begins is also seen to depend on the size ratio of the particles (increasing with the size ratio). From Figure 3-3 it is seen that the mixing region obtained by increasing the speed from an initially segregated bed is smaller than that obtained by decreasing the speed from an initially centrifuged bed. Figure 3-4 shows that there is negligible effect on the mixing patterns for varying percent fines.

Figure 3-5 is a comparison of the results for the acrylic/acrylic and acrylic/alumina mixtures, showing that the same trend is observed in the two cases. The only difference is that, the data for the acrylic/alumina mixtures are slightly shifted to the left, indicating that transition from core segregation to mixing and mixing to reverse segregation occurs at lower speeds, for higher size ratios.

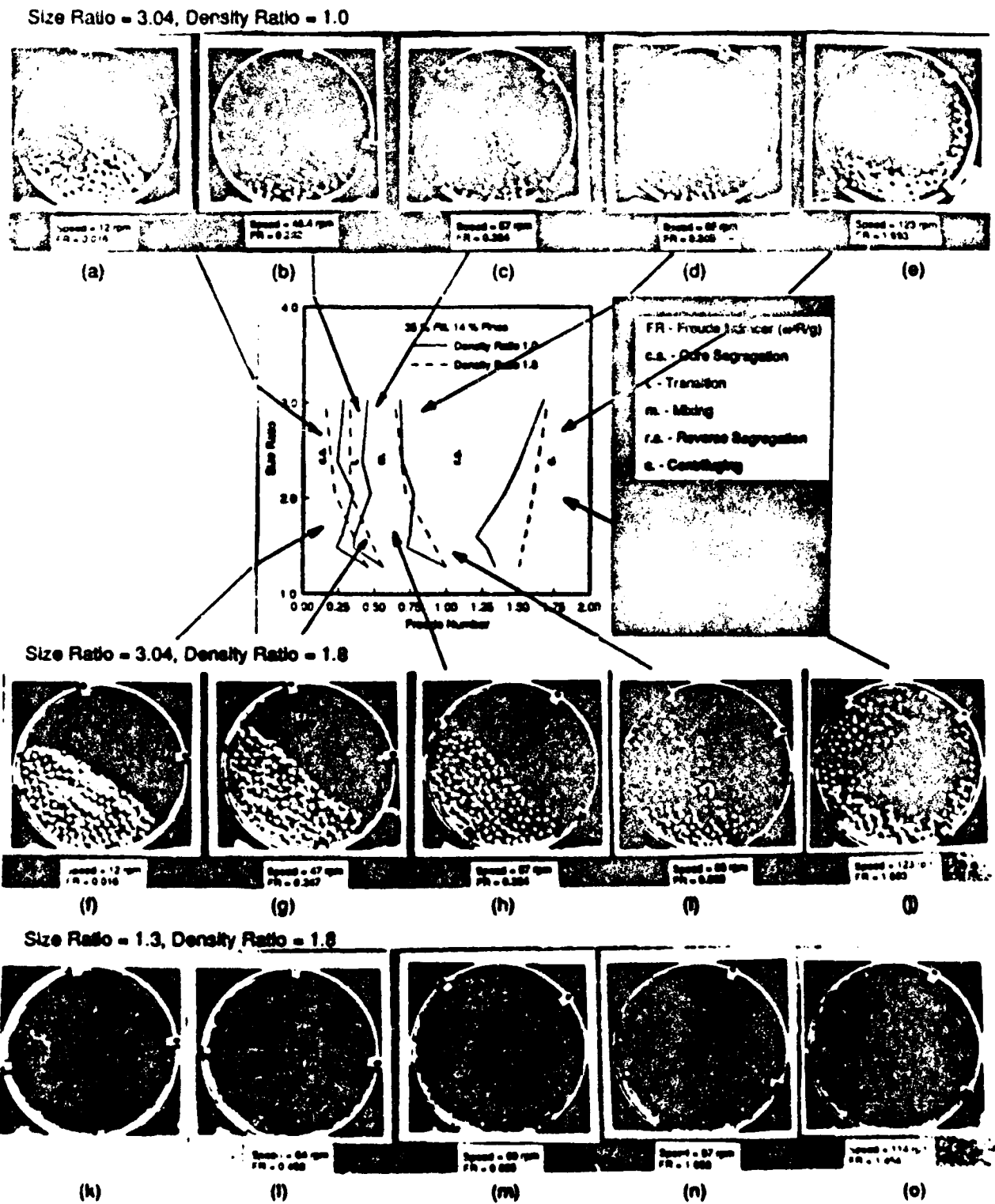


Figure 3-2: Experimental results for model materials, for increasing speed.

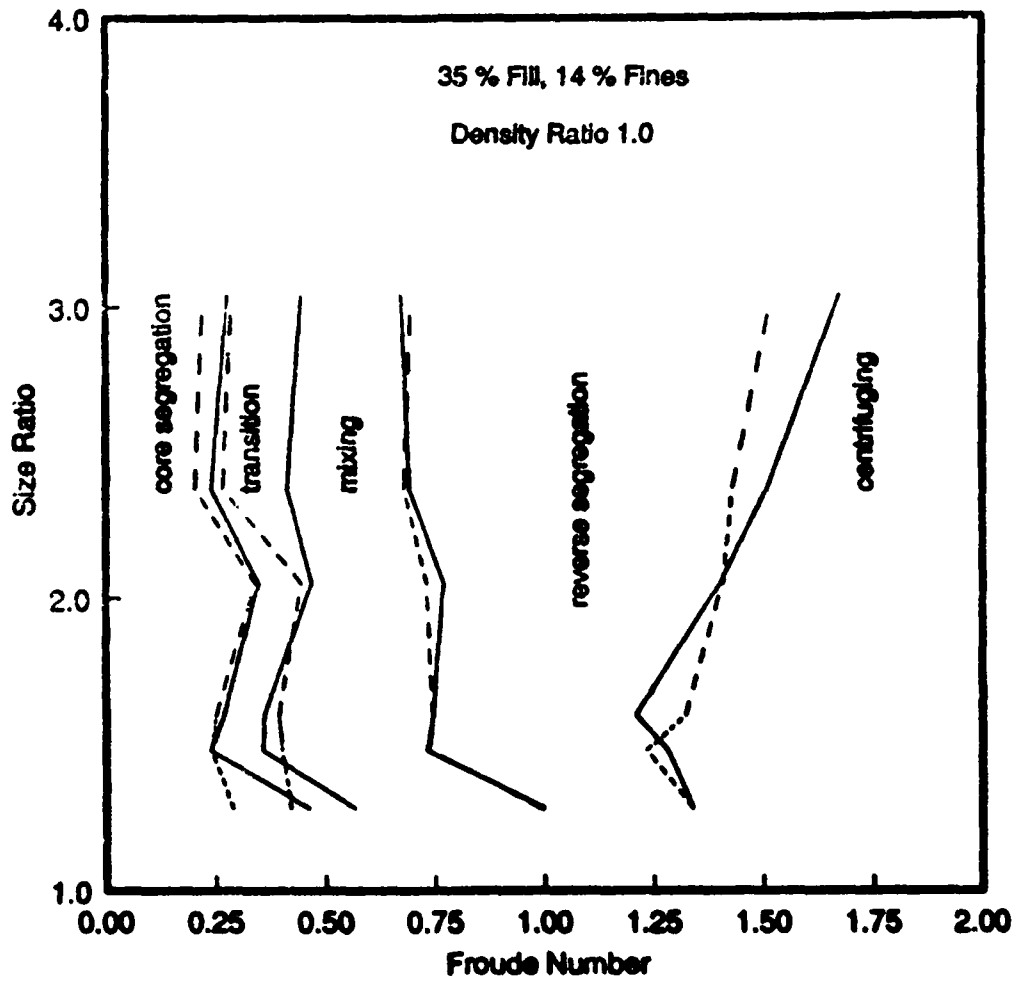


Figure 3-3: Segregation behavior for varying size ratios and drum speeds, for increasing speed (solid lines) and decreasing speed (dashed lines).

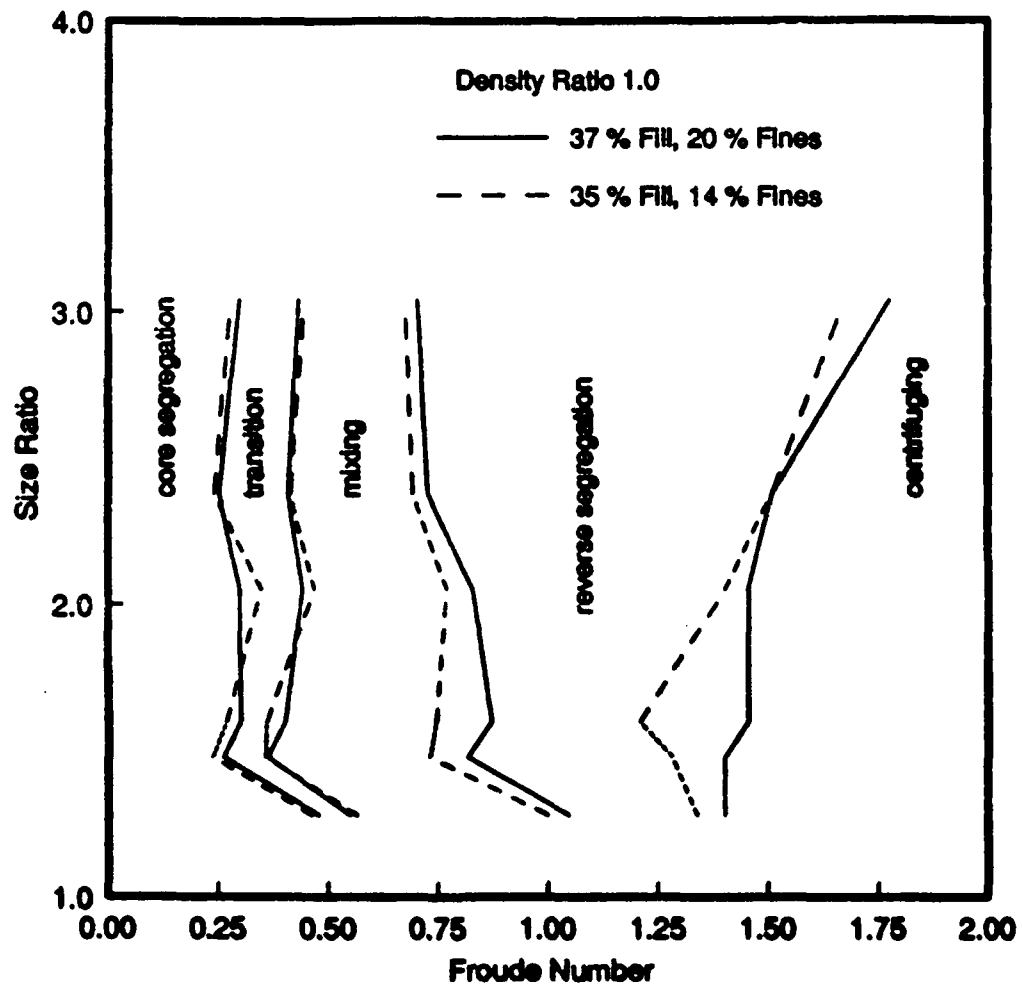


Figure 3-4: Segregation behavior for varying percent fines and percent fill.

The following are the implications of these results to MMC systems:

1. Comparisons of similar results for MMC systems can determine the effect of other forces (Van Der Waals and electrostatic forces for example) on the blending of fine powders.
2. For a fixed cylinder size and size ratio these results give a range of speeds at which mixing can be achieved. Moreover, these results can be extended to other cylinder sizes, using  $\omega^2 R/g$  (non-dimensionalized number), which provides scale-up parameters for macromixing of MMC systems.
3. If similar results are obtained for MMC systems, then the conditions for studying micromixing are easily defined.

### 3.1.4 Conclusions

Experiments were conducted to study the blending of binary mixtures of spherical particles, and macro-mixing was observed as a function of size ratio, density ratio, rpm, percent fill and percent fines. Spherical particles varying in size between 3.1mm and 9.5mm were used in the experiments. The results have been expressed in terms of  $\omega^2 R/g$  versus size ratio, which provides a segregation behavior diagram showing the mixing region which is of most interest in our studies. The mixing region is defined as the region where the finer particles were seen to be evenly distributed in the bed. The results were seen to be reproducible, with experimental errors within acceptable limits. The range of rpm's for mixing region was observed to increase with decreasing size ratio of the binary mixture. For the experiments where the density ratio was 1.8, the coarser particles used were more dense ( $\rho=1.3$ ) than the finer particles ( $\rho=0.72$ ). Therefore, the mixing region is not affected by the density difference at small size ratios, but does increase the mixing region at bigger size ratios. With all other parameters remaining constant, variation in percent fines is seen to have negligible effect on the results.

## 3.2 MMC Powder Materials

### 3.2.1 Apparatus

The blending experiments will be conducted in rotary blenders which are capable of being pressurized to a pressure of 2 atm of a selected gas, and may also be evacuated to a vacuum of better than  $10^{-2}$  atm. The blenders are constructed from seamless steel pipe, and have a titanium insert to eliminate contamination from the steel of the drum. Three separate drums have been constructed, with nominal internal diameters of 5, 10 and 20 centimeters and  $L/D = 1$ . The design of the unit allows for the use of either glass or metal end plates, thus allowing the possibility of both visual observations and controlled sampling. The gas exchange is accomplished through the use of a rotating gas seal, allowing for atmosphere control throughout the duration of an experiment. Figure 3-6 shows a schematic view of

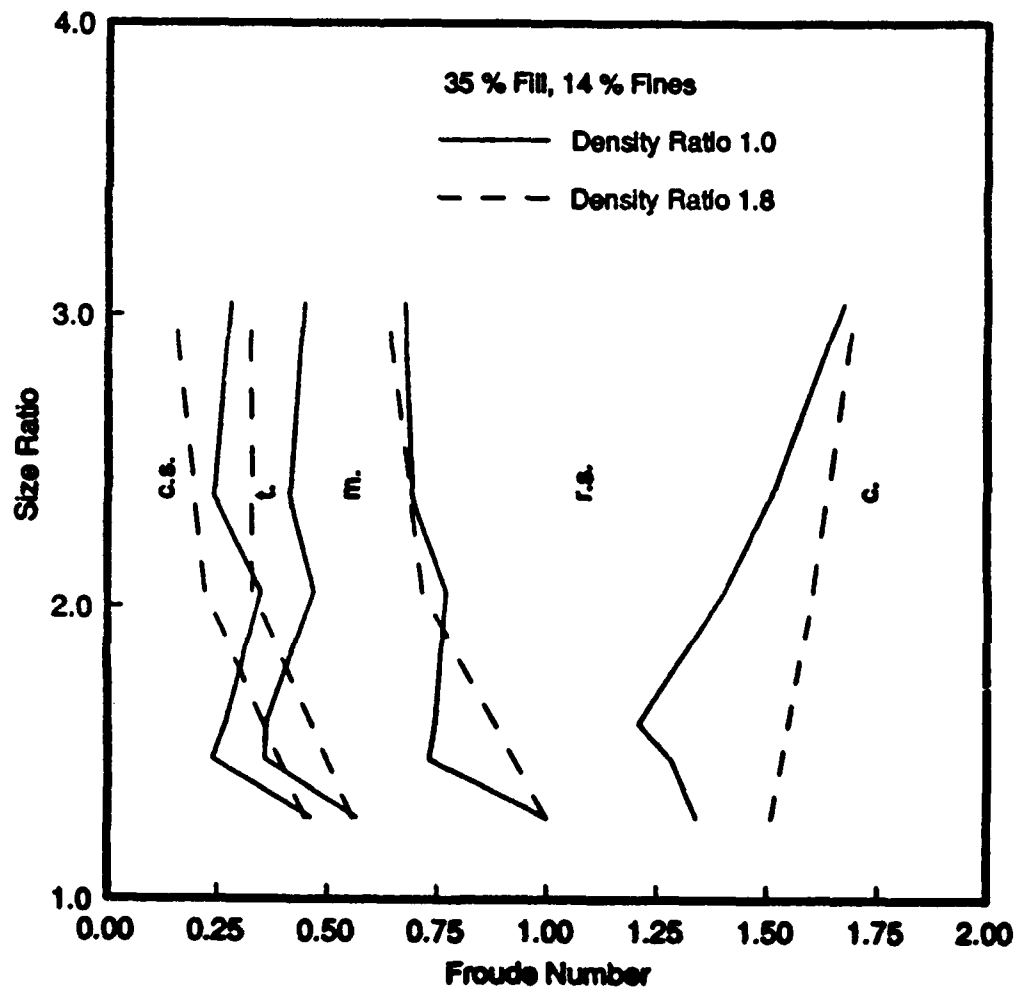


Figure 3-8: Segregation behavior for varying density ratio.

the gas delivery system. The speed of the drums is controlled via belt-driven rollers connected to a variable speed motor, and is monitored through the use of an optical tachometer. Vacuum is achieved by using a rotary vacuum pump, and can be improved through the use of a diffusion pump.

### 3.2.2 Materials

The choice of materials for the blending experiments was based on a determination of those systems of greatest interest to the sponsors, as well as those systems which will provide the easiest means of investigating the variables of interest. All of the materials used were commercially available products, and have been chosen after examining samples of the materials for size distribution, shape and density. The list presented in Table 3-3 (see also Figure 3-7) represents the materials to be used in the blending experiments, as well as a summary of the characteristics of each powder. Due to the difficulty and expense of obtaining the aluminide material, most of the experiments with the titanium will be conducted with the Ti-6-4, of which large quantities are currently in our possession. Due to the similarity of the densities, the results of the Ti-6-4 blends should be applicable to the aluminide powder, and these can then be used for the experiments which will result in blends targeted for the consolidation experiments. One notable absence from this list is whisker reinforcement materials. Due to their expense, we have refrained from purchasing these materials until such time as a better appreciation of the variables of interest allows a few key experiments to be designed, to investigate accurately the effect of changes in the reinforcement shape.

### 3.2.3 Procedure

A procedure has been developed to ensure that the initial conditions remain the same for each set of experimental conditions. The first step is to ensure that the drum internal surfaces are clean and free of any residue from previous tests. The drum is then assembled, taking care to make sure that the faces of the end plates touch the drum flanges at all points. This is to ensure that there are no material losses and disturbances due to gaps between the end plates and the body of the drum. With the drum standing vertically on its front end, a premeasured amount of the matrix powder is introduced into the drum using a funnel through a feed hole in the back plate of the drum. The drum is then placed horizontally, and the corresponding amount of reinforcement powder is added to the drum through the use of a specially designed "scoop". This results in the arrangement shown in Figure 3-8, with the matrix powder evenly distributed in the drum, and the reinforcement powder lying on the surface of the bed, along the axis of the drum. All of the experiments conducted use this configuration as a starting point.

The filled drum is then placed in the drive system, and the speed adjusted to the desired range, depending on the particular experiment being conducted. With the glass end plate in place as the front of the drum, visual observation may be conducted and photographs taken to record the events. In most



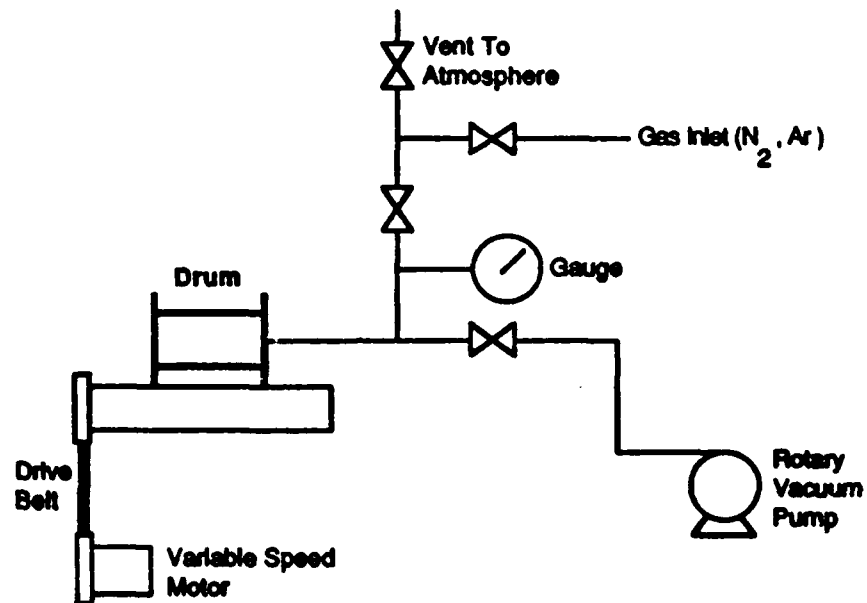


**Figure 3-6: Schematic of gas delivery system for blending experiments**

Table 3-3: Materials for Blending Experiments

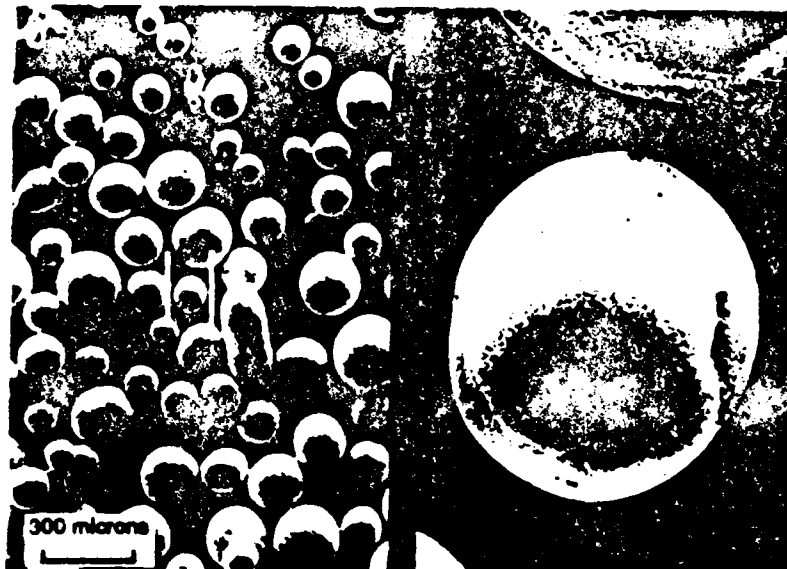
Material ( )-supplier	Size (as received)	Density (g/cm <sup>3</sup> )	Shape
PREP Ti-6Al-4V (Nuclear Metals)	-35 mesh -80 mesh	-4.5 4.51	Spherical Spherical
PREP Ti-24Al-11Nb (Nuclear Metals)	-35 mesh	-4.4	Spherical
cp Ti (Atlantic Equipment Engineers)	-100 mesh	-4.5	Irregular
Fe - Spheromet 100 Fe - Atomet 604 (Quebec Metal Products)	-35 mesh -35 mesh	-7.6 -7.6	Spherical Irregular
Silicon Carbide (Norton Company)	nominally 240 grit	3.20	Irregular Sharp
Boron Carbide (Norton Company)	nominally 220 grit	2.51	Irregular Sharp

cases, this usually consists of varying the speed of rotation of the drum (either increasing or decreasing) and taking pictures at set increments of the speed to determine the macromixing characteristics and corresponding motion of the bed.

In order to reduce the possibility of contamination of the results, fresh material will be used for all experiments (micro- and macro- mixing). For those studies aimed at determining the micromixing characteristics of the bed, the experiments will be stopped at a predetermined point, and the bed infiltrated with a low-viscosity epoxy material to "freeze" the bed in place. Once the epoxy sets, the bed may be removed as one complete body, and sectioned for microscopic examination. This procedure may also be employed for the preparation of samples for consolidation experiments, so that the structure of the mixed bed may be preserved through to the formation of a solid material. In cases where neither of the previous cases is desired, then the material will simply be sealed into cans and disposed of in the appropriate manner.



(a). P.R.E.P. Ti-6Al-4V powder

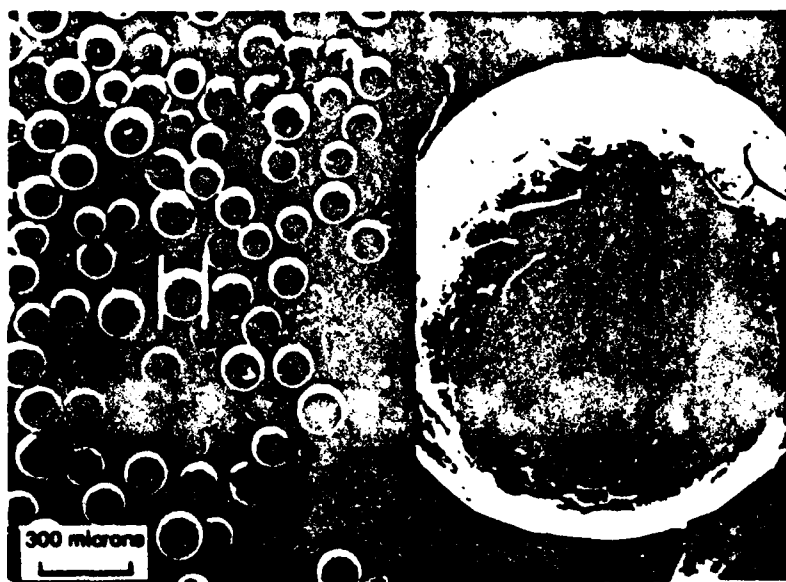


(b). P.R.E.P. Ti-24Al-11Nb powder

Figure 3-7: Materials for use in blending experiments



(c). Commercially Pure Ti powder



(d). Spheromet 100 Fe powder

Figure 3-7, cont.



(e). Atomet 604 Fe powder



(f). Silicon Carbide powder

Figure 3-7, cont.



(g). Boron Carbide powder

Figure 3-7, cont.

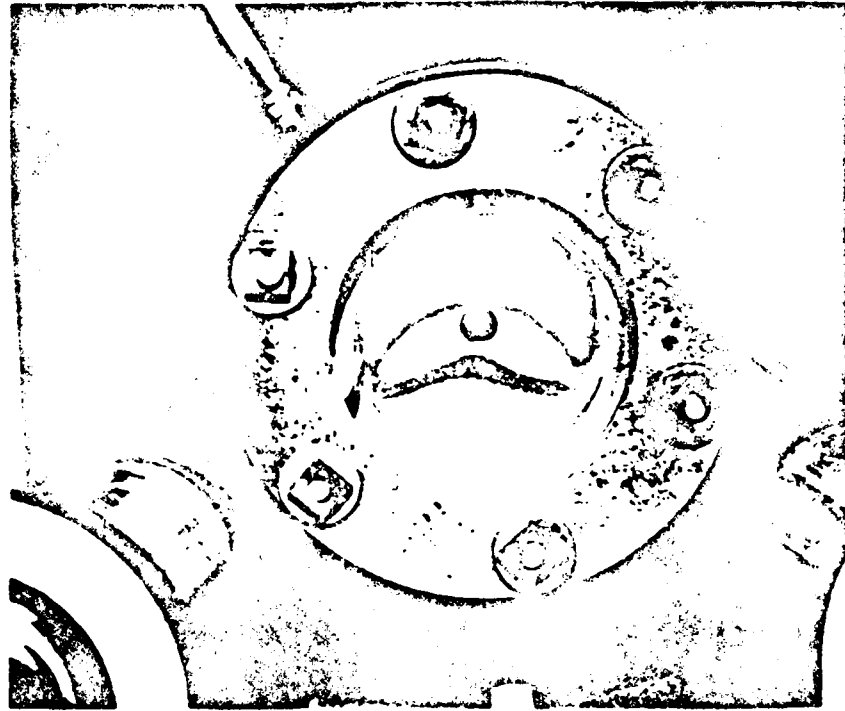


Figure 3-8: Initial placement of reinforcement and matrix charge.

### 3.2.4 Variables of Interest and Test Matrix

As described in the review of previous work, there are many operating variables which may be considered to have some effect on the mixing of materials, and especially materials which have a tendency towards segregative behavior. It is necessary then to make some estimation of the degree of importance of these variables in order to arrive at a reasonable set of experiments to perform, that will give a complete picture of the mixing processes without taking an inordinate amount of time. Based upon an examination of the literature, the following variables will be used in a test matrix. This closely parallels the tests done on the model materials, so that a comparison of the effects of these variables can be easily made, and some deduction as to the role of small-particle effects (such as electrostatic forces) can be made. The only variable unique to this set of experiments is the gas atmosphere. In the case of the model materials, the size of the particles is such that unreasonable values of the gas pressure and rotational speed would be required in order to observe any effects of changes in the gas.

- Percent fill
- Percent fines
- Size ratio
- Rotating speed of the drum (RPM)

- Gas atmosphere
- Density ratio
- Particle Shape (matrix and reinforcement)

The experiments will be conducted so that in each case the effect of the variable will be determined as a function of the rpm, i.e., the rpm will be used as the independent variable in each case. The experiments will then be conducted in the same manner as the model material experiments, using one of the other quantities as a variable and keeping the rest fixed. For the size ratio, percent fines and percent fill, three separate cases for each variable should give a sufficiently broad spectrum. The gas atmosphere can be varied both in composition and pressure, with three variations for each instance being sufficient. These experiments will be specifically targeted for the visual observations of macromixing. It has been demonstrated in earlier work that results for different absolute sizes of particles and drums can be scaled using the size ratio and the nondimensionalized speed ( $\omega^2 R/g$ ), thus allowing comparison of the model material results for macromixing to those obtained for MMC materials (subject to the constraint of having the same gas atmosphere). Once the situations corresponding with observably good macromixing have been established, investigations of the micromixing occurring in these instances can be examined in a few well defined cases. The details of the latter experiments have not yet been finalized, but will likely be less time consuming than this first round of experiments.



---

## References

---

1. T.C. Willis, "Spray Deposition Process for Metal Matrix Composites Manufacture", *Metals and Materials*, August 1988, p. 485-488.
2. Campbell H., and Bauer W.C., "Cause and Cure of Demixing in Solid-Solid Mixers", *Chemical Engineering*, Vol. 73(19), 1968, p. 179-185.
3. Henlein H., Brimacombe J.K., and Watkinson A.P., "Experimental Study of Transverse Bed Motion in Rotary Kilns", *Metallurgical Transactions B*, Vol. 14B, 1983, p. 191-205.
4. Rutgers R., "Longitudinal Mixing of Granular Material Flowing Through a Rotating Cylinder: Part 1. Descriptive and Theoretical", *Chemical Engineering Science*, Vol. 20, 1965, p. 1079-1087.
5. Henlein H., Brimacombe J.K., and Watkinson A.P., "The Modeling of Transverse Motion in Rotary Kilns", *Metallurgical Transactions B*, Vol. 14B, 1983, p. 207-220.
6. Nityanand N., Manley B., and Henlein H., "An Analysis of Radial Segregation for Different Sized Spherical Solids in Rotary Cylinders", *Metallurgical Transactions B*, Vol. 17B, 1986, p. 247-257.
7. Henlein H., Brimacombe J.K., and Watkinson A.P., "An Experimental Study of Segregation in Rotary Kilns", *Metallurgical Transactions B*, Vol. 16B, 1985, p. 763-774.
8. Lacey P.M.C., "Developments in the Theory of Particle Mixing", *Journal of Applied Chemistry*, Vol. 4, 1954, p. 257-268.
9. Cahn D.S., Fuerstenau D.W., Healy T.W., Hogg R., and Rose H.E., "Diffusional Mechanism of Solid-Solid Mixing", *Nature*, Vol. 209, 1966, p. 494-498.
10. Hogg R., and Fuerstenau D.W., "Transverse Mixing in Rotary Cylinders", *Powder Technology*, Vol. 6, 1972, p. 139-148.
11. Cahn D.S., and Fuerstenau D.W., "A Probabilistic Model of the Diffusional Mixing of Particulate Solids", *Powder Technology*, Vol. 2, 1968, p. 215-222.
12. Donald M.B., and Roseman B., "Mixing and De-Mixing of Solid Particles: Part 1. Mechanisms of Mixing in a Horizontal Drum Mixer", *British Chemical Engineering*, Vol. 7(10), 1962, p. 749-753.
13. Hogg R., Cahn D.S., Healy T.W., and Fuerstenau D.W., "Diffusional Mixing in an Ideal System", *Chemical Engineering Science*, Vol. 21, 1966, p. 1025-1038.
14. Rutgers R., "Longitudinal Mixing of Granular Material Flowing Through a Rotating Cylinder: Part 2. Experimental", *Chemical Engineering Science*, Vol. 20, 1965, p. 1089-1100.
15. Bridgwater J., "Fundamental Powder Mixing Mechanisms", *Powder Technology*, Vol. 15, 1976, p. 215-238.
16. Scott A.M., and Bridgwater J., "Interparticle Percolation: A Fundamental Solids Mixing Mechanism", *Industrial and Engineering Chemistry - Fundamentals*, Vol. 14(1), 1975, p. 22-27.
17. Roseman B., and Donald M.B., "Mixing and De-Mixing of Solid Particles: Part 2. Effects of Varying the Operating Conditions of a Horizontal Drum Mixer", *British Chemical Engineering*, Vol. 7(11), 1962, p. 823-827.
18. Rose H.E., "A Suggested Equation Relating to the Mixing of Powders and its Application to the

- Study of the Performance of Certain Types of Machines", *Transactions of the Institution of Chemical Engineers*, Vol. 37, 1959, p. 47-64.
19. Ullrich M., "Entmischungserscheinungen in Kugelschüttungen (translation on hand)", *Chemie-Ingenieur Technik*, Vol. 41(16), 1969, p. 903-907.
  20. Rogers A.R., and Clements J.A., "The Examination of Segregation of Granular Materials in a Tumbling Mixer", *Powder Technology*, Vol. 5, 1971, p. 167-178.
  21. Sauer C. von., "Mischungs- und Entmischungsprobleme bei Metallpulvern. Teil 1: Verhalten von Metallpulvern beim Mischprozeß - Makroverteilung der Komponenten (translation on hand)", *Neue Hütte*, Vol. 17(6), 1972, p. 358-362.
  22. Sauer C. von., "Mischungs- und Entmischungsprobleme bei Metallpulvern Teil 2: Verhalten von Metallpulvern beim Mischprozeß - Mikroverteilung der Komponenten (translation on hand)", *Neue Hütte*, Vol. 18(10), 1973, p. 231-234.
  23. Williams J.C., "The Segregation of Particulate Materials. A Review", *Powder Technology*, Vol. 15, 1975, p. 245-251.
  24. Rietema K., "Powders, What Are They?", *Powder Technology*, Vol. 37, 1984, p. 5-23.
  25. Cottaar W., and Rietema K., "The Effect of Interstitial Gas on Milling", *Powder Technology*, Vol. 38, 1984, p. 183-194.
  26. Cottaar W., Rietema K., and Stemerding S., "The Effect of Interstitial Gas on Milling. Part 2", *Powder Technology*, Vol. 43, 1985, p. 189-198.
  27. Cottaar W., and Rietema K., "The Effect of Interstitial Gas on Milling. Part 3. Correlation Between Ball and Powder Behavior and the Milling Characteristics", *Powder Technology*, Vol. 46, 1986, p. 89-98.
  28. Rietema K., and Cottaar W., "The Effect on Interstitial and Circumambient Gas in Fine Powders on the Scaling Up of Powder-Handling Apparatus as Illustrated by the Ball Milling Operation", *Powder Technology*, Vol. 50, 1987, p. 147-154.
  29. Cottaar W., and Rietema K., "Effect of Interstitial Gas on the Milling of Fine Powders", *Powder Technology*, Vol. 48, 1986, p. 219-225.



**Second-Year Progress Report for the Project**

**Deformation Processing of  
Composites**

**Henry R. Piehler  
Daniel M. Watkins  
Michael Kuhni  
John Richter**

**Deformation Processing Laboratory  
Department of Metallurgical Engineering & Materials Science  
Carnegie Mellon University  
Pittsburgh, Pennsylvania 152213-3890**

## ***Introduction***

This project is designed to develop a fundamental understanding of the deformation processing of short-fiber, powder-based metal matrix composites for high temperature applications. This knowledge will enhance the selection, fabrication, and performance of these materials and will complement the current blending research at Carnegie Mellon described in the previous section. The framework and methodology for this project is based upon selecting model composite geometries and materials plus designing advanced deformation processing equipment in order to physically and analytically model existing and novel composite processing conditions.

This report is divided into the following sections:

- **HIPing of 7-Filament Arrays.** The model 7-filament geometry used for the physical and analytical modeling of the HIPing process is described in this section, and experimental and analytical results achieved to date using this model geometry are reported.
- **Hot Triaxial Compaction.** The rationale for the benefits achievable by compacting monolithic powders and powder-based metal matrix composites using a shear in addition to a hydrostatic stress is identified. The design and construction of the unique hot triaxial compaction apparatus built to accomplish this goal is described.
- **Future Efforts.** Future deformation processing efforts involving HIPing and hot triaxial compaction are described. These deformation processing studies will involve composites fabricated from SiC and Ti-6Al-4V, both in the seven-filament geometry and as short fibers and powders, respectively.

### ***HIPing of 7-Filament Arrays***

A simplified model geometry, the 7-filament array [Figures 1 and 2], has been developed to study the micromechanisms of powder consolidation during Hot Isostatic Pressing (HIPing). As previously used in study of the sintering process<sup>1-3</sup>, physical models allow observation consolidation at all stages under controlled conditions. As a result, the fundamental consolidation mechanisms are isolated from stochastic factors (e.g., random packing). The goals for the use of this 7-filament array are to:

- identify the operative micromechanisms in powder consolidation under both both applied stress state and temperature.
- analyze the influence of stress state and temperature on the resulting microstructure (grain morphology, reaction zone, dislocation structure) to develop a fundamental framework for optimizing the processing path for real powder compacts.
- identify the effect of a reinforcing phase on the consolidation-parameter/microstructure relationship.

As will be described in greater detail in the next section, this project is focussed on the effects of shear stress in addition to a hydrostatic stress on powder compaction. The goal is to provide fundamental information on the effect of shear stress on individual existing consolidation mechanisms and possibly identify additional consolidation mechanisms mechanisms as well. The approach is to use scaling laws, simple models, and transmission electron microscopy to examine the dominant mechanisms under a range of realistic processing conditions for unreinforced and reinforced matrix material [Figure 3]. Work is also proceeding to refine process controls in order to accumulate and utilize accurate displacement, temperature, and pressure data as a function of time.

In practice, the fibers/wires are arranged and sealed, under vacuum, in a metal tube. Though more difficult to execute, these "canning" techniques are basically the same as those used for HIPing of powders. Since the purpose of this physical modeling is to observe consolidation under controlled and easily reproducible geometrical and processing conditions, filament sizes may be larger than powder particles, subject to the following size-selection criteria:

- the availability of a range of sizes appropriate for scaling analysis
- the use of filament sizes sufficiently close to real powder sizes so that trends may be extrapolated and mechanisms operative in real powder scale are not overwhelmed by mechanisms dominant at the scale of the model.
- the modeling of metal matrix composites, where the reinforcing fiber may be placed either in the interstitial or substitutional sites in the metal wire array, depending on the appropriate wire size which is available and/or chosen.

The tube must be of the same material as the wires and either provide as little resistance to compression as possible or simulate the mechanical response of the next 12 filaments in a close-packed array. Low resistance to deformation can be achieved with either a small wall thickness to diameter ratio or by using a weaker tube material. For example, in this study, the tube used is of commercial purity titanium (CP-Ti) and the wires of either Ti-6Al-4V or CP-Ti. The rationale for this material selection are given in the next section.

One final criterion for the selection of the overall compact size is the ability to make thin specimens for transmission electron microscopy (TEM) from the compacts. Since the compact geometry is new, adjustments in compacted sample size may be necessary as the TEM technique is developed.

Extension of this geometry to 19 filament arrays is possible [Figures 4 and 5]. The 19-filament packing geometry is more difficult but not impossible to control. This 19-filament geometry is of interest in that effects of packing on the local stress distribution and thus on consolidation may be observed. Further, interactions among filaments in the substitutional position can be studied [Figure 5A].

The criteria for a model material system include:

- the absence of a pervasive, compaction inhibiting oxide or other surface film.
- the availability of wire and a non-constraining or mechanically similar container material (as described above).

- the absence of phase transformations during the deformation processing cycle.
- for simplicity, a single phase system, if possible.
- a microstructure amenable to observation by TEM.
- an easily variable grain size.
- the availability of physical property data required for analytical modeling.

As is the case in this study, some of these considerations may strongly influenced by the desire to study a particular system. In this research a compromise between material specific and ideal model system information is made. In this series of experiments Ti-6Al-4V, a candidate composite matrix material is being studied. The major problem is in the additional complexity of analysis resulting from this two phase system. Cp-Ti wire is also studied for two reasons: first, to contrast the effects of particle hardness to particle compaction [Figure 4] and second, to make a model compact with no chemical inhomogeneities and no second phase. With the Cp-Ti wires and tubes, the analysis of the stress distribution between tube and filaments can be more accurately modeled.

For the initial 7-filament study <sup>1</sup> (Appendix I), pure aluminum was chosen but has been subsequently abandoned as a model material owing to problems in both sealing and consolidation resulting from the presence of a tenacious oxide film. The deleterious effect of the oxide film on interparticle bonding is well documented in the aluminum P/M literature. Interestingly, however, the use of this 7-filament geometry may be the best way to observe local oxide film buildup in these materials. In addition, the use of this film to restrict certain diffusion mechanisms in order to isolate plastic flow from power law creep during consolidation is also a possibility.

The 7-filament array has a zero consolidation density of 92% whereas powders typically have a tap density of about 60%. In fact, some of the modeling efforts in the past have specified 90% as the transition from the intermediate stage of consolidation (cylindrical porosity) to the final stage (isolated spherical porosity). Deviations based on the 7-filament geometry, rather than limiting analysis, enable simple models to be employed without having to make assumptions about the transitions between different stages of consolidation.

The mechanisms which modify pore morphology include those from sintering <sup>4-6</sup>:

1. surface diffusion from a surface source



2. volume diffusion from a surface source
3. volume diffusion from a grain-boundary source
4. grain-boundary diffusion from a grain-boundary source
5. volume diffusion from a dislocation source.

For HIPing, the following mechanisms are operative <sup>7,8</sup>:

6. plastic flow
7. power law creep
8. diffusional (Nabarro-Herring, Coble) creep

The first approach to modeling has been to add each mechanism's contribution independently based upon assumed geometries at specific densities and stages of compaction. The problems associated with making this assumption are circumvented to some extent by using the 7-filament geometry, since the transition from cylindrical porosity to closed spherical type porosity does not occur until the very last stage of consolidation [Figure 6A], where the cylindrical pore pinches off at various points along the sample (and filament) axis. This simplifies matters somewhat, but some interaction still does occur between mechanisms at various stages of compaction. For example, the effect of dislocation motion by plastic yielding and power law creep can clearly affect Coble creep via a dislocation/grain-boundary interaction. Hence, the dislocations generated by mechanisms (6) and (7) will enhance mechanism (5).

Additionally, since composite materials generally require more time, temperature, or pressure to HIP to full density <sup>9</sup>, the constraining effect of a reinforcing constituent must be studied. The 7-filament geometry is ideally suited to study these densification-inhibiting effects associated with the presence of a reinforcing constituent.

Herring's scaling laws <sup>10</sup> can be judiciously applied when the entire driving force for consolidation is considered. Though these laws ignore interactions among consolidation mechanisms, they can be extremely useful if one mechanism strongly dominates the consolidation process. The scaling law analysis defines the ratio of times for two different sized wires,  $R_1$  and  $R_2$  ( $=\lambda R_1$ ), to reach identical geometries (same shape - different size). For plastic flow and creep, the contribution of the surface energy to the total driving force is generally small enough to be ignored meaning:

$$\Delta t_2 = \lambda^2 \Delta t_1$$

at constant hydrostatic pressure.

Surface diffusion is independent of stress and Herring's analysis, modified for cylinders, applies:

$$\Delta t_2 = \lambda^4 \Delta t_1$$

Grain boundary has the same derivation as surface stress but the form of the driving force is  $(\gamma/R + P)$  so that

$$\Delta t_2 = \lambda^3 \Delta t_1$$

holds as long as  $(\gamma + PR)$  is held constant. Here  $\gamma$  is the surface energy,  $P$  is applied hydrostatic pressure and  $R$  is the original particle radius. As with plastic flow, at HIP pressures the surface energy contribution to the driving force is small, so that the experiment is essentially performed at constant pressure.

Volume diffusion should scale as

$$\Delta t_2 = \lambda^3 \Delta t_1$$

Therefore, while the analysis provides no insight on the dominant diffusion mechanism in densification (surface diffusion is non-densifying) it is clearly seen that an observation of geometric similarity at constant conditions of pressure, temperature, and time is indicative of plastic flow or creep effects.

## **HOT TRIAXIAL COMPACTION**

There is anecdotal evidence to indicate that imposing a shear stress in addition to hydrostatic stress during powder compaction will not only enhance densification but also improve the fracture resistance of the resulting compact. The first of these triaxial compaction (shear + hydrostatic stress) studies is that of Koerner<sup>11</sup>, whose Mohr's circle representation of the stress states and deformation paths obtainable using cold triaxial compaction is illustrated in Figure 8. For hot triaxial compaction, the potential range of deformation/temperature paths is considerably increased, as is illustrated in Figure. 9. However, none of the previous investigators of hot and cold triaxial compaction has been able to control the temperature, shear stress, and hydrostatic stress independently, i.e., actually impose the sequence of processing conditions represented by Figure 9. It was this need for independent control of temperature, shear stress, and hydrostatic stress during the compaction of particulates and composites that motivated us to design and fabricate our first generation hot triaxial compaction unit as described in the next section. This fairly rapid triaxial compaction has the capability of:

- preserving unstable microstructures by compacting at lower temperatures, i.e., trading shear stress for temperature to achieve comparable densities.
- enhancing compact properties at comparable densities by promoting interparticle shear during compaction.
- minimizing fiber fracture during particulate/fiber composite compaction by enhancing the flow of the particulate matrix during compaction.
- minimizing the formation of stable spherical pores by minimizing thermal exposure.
- enhancing the fracture resistance of structural ceramics by reducing the scale of the defect geometry.

The design and construction of the special HIP (hot triaxial compaction) unit has been the principal effort to date. The design of this unit essentially involves a judicious combination of established technologies executed in a novel manner. The vessel sealing and force application borrow strongly from compressor technology. An in line load cell and hydraulic control system [Figures 10 and 11] with safety interlocks was designed and built with the help of John Richter and Co. The vessel operates at pressures of up to

60,000 psi while at the same time imposing an axial force of up to 50,000 lb and reaching the temperature levels described below.

The first furnace module, based on HIT technology, is currently being tested and is expected to operate to 1000° C. A second design, similar to that used in rock mechanics testing equipment<sup>12,13</sup> and capable of reaching temperatures of up to 1400° C, is currently under construction. The need to restrict conductive heat transfer made it necessary to design and fabricate alumina forging surfaces with a load train comprised of both alumina and zirconia. Both furnaces provide a 2-1/8" diameter x 1-1/2" high hot zone with a 1-1/2" stroke capability at forces up to 50,000 lbs and pressures of up to 60,000 psi.

The initial specimens are being prepared using glass encapsulation techniques. The specimens dimensions are 1" diameter and at least 1" high, which will provide a reasonable specimen size for subsize tensile, bend, Charpy, and fatigue tests.

### *Future Efforts*

Ashby's hot isostatic pressing diagrams provide a useful compilation, organization, and modeling of the HIP consolidation performed to date. The equations for this analysis are given in reference 1 (Appendix I). Future analytical efforts will be directed at modifying these maps to include the effects of imposing a shear stress in addition to a hydrostatic stress during the compaction process.

Examining the cracked fibers shown in Figures 5A and 7A leads us to suspect that they occurred during processing. Certainly fibers are damaged during extrusion<sup>14,15</sup> and in forging of fully dense composites<sup>9</sup>. In the latter case, fiber to fiber contact was seen to precipitate fracture of tungsten wires in a superalloy matrix.

TEM studies are being initiated to examine the local microstructural changes during HIP and relate them to the operative mechanisms.

One accepted and one submitted abstract of future presentations are contained in Appendix II.

## References

- (1) Yoshida, K., Steyer, T.E., Watkins, D., Piehler H., "HIP Consolidation of Seven Filament Arrays of Aluminum Wires", *Physical Modeling of Metalworking Processes*, Editors: Erman, E. and Semiatin, S.L., TMS Publications, 1987.
- (2) B. H. Alexander and R.W. Balluffi, "The Mechanism of Sintering of Copper", *Acta Met.* 5 (1957), pp. 666-677.
- (3) J. Brett and L. Seigle, "The Role of Diffusion versus Plastic Flow in the Sintering of Model Compacts", *Acta Met.* 14 (1966), pp. 575-582.
- (4) R. L. Coble, *J. Am. Ceram. Soc.*, 41(1958), P. 55.
- (5) T. L. Wilson and P. G. Shewmon, "The Role of Interfacial Diffusion in the Sintering of Copper", *Trans. AIME* 236 (1966), pp. 48-58.
- (6) M.F. Ashby, "A First Report on Sintering Diagrams", *Acta Met.* 22 (1974), 275-289.
- (7) A.S. Helle, K. E. Easterling, and M. F. Ashby, "Hot Isostatic Pressing Diagrams: New Developments", *Acta Met.* 33 (1985), pp. 2163-2174.
- (8) D. S. Wilkinson, Ph.D Thesis, University of Cambridge (1977).
- (9) A. Y. Kandiel, J-P. A. Immariageon, W. Wallace, and M. C. de Malherbe, "The Fracture Behavior of Tungsten Wire Reinforced Superalloy Composites during Isothermal Forging", *Metall. Trans.* 15A (1984), pp. 501-510.
- (10) C. Herring, "Effect of Change of Scale on Sintering Phenomena", *J. Appl. P.* 21 (1950), pp. 301-303.
- (11) R.M. Koerner, "Triaxial Stress State Compaction of Powders," *Powder Metallurgy Processing, New Techniques and Applications*, H.A. Kuhn and A. Lawley, ed., Academic Press, N.Y., pp.33-50, 1978.
- (12) Rack, URI Meeting at Carnegie Mellon University, Oct. 1988.

- (13) Clauer, Seminar at Carnegie Mellon University, Oct. 1988.
- (14) M. S. Patterson, "A High-Pressure, High-Temperature Apparatus for Rock Deformation", *Int. J. Rock. Mech. Min. Sci.* 7 (1970), pp. 517-526.
- (15) P. Malbrunot, P. A. Meunier, and D. Vidal, Design of Furnaces for Internal Heating in High Pressure Gases, *Chem. Eng. World*, 7 (1972), no. 3, pp. 55-58.



**FIG.1: Idealized geometry for physical model of powder consolidation. The tube is evacuated and the ends are TIG welded prior to HIP cycle.**



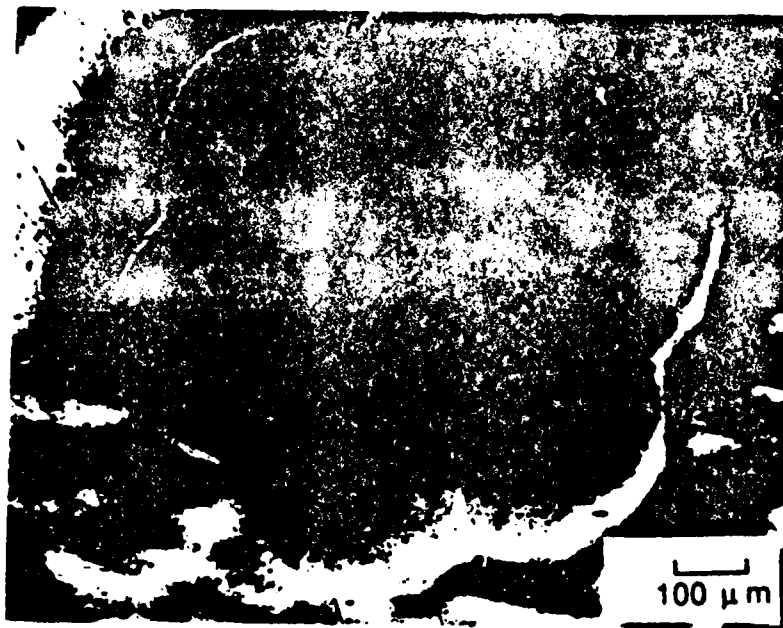


FIG. 2: Ti-6AL-4V filaments consolidated at 750 C and 15,000 psi in a CP Titanium tube. Prior Particle Boundaries (PPBs) show small amounts of residual porosity.

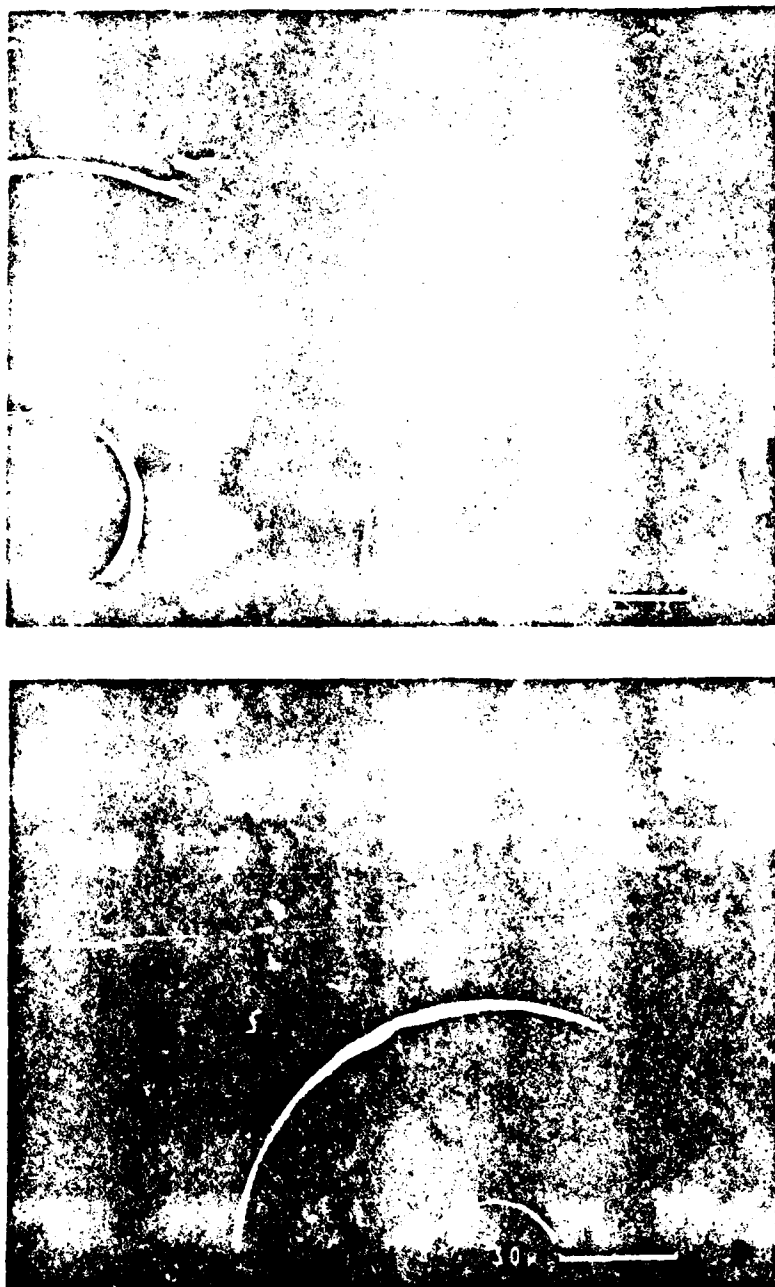


FIG. 3: CP Titanium filament with SiC SCS-6 reinforcement colsolidated at 650 C and 10,000 psi. Pores are sharply cusped at final stages indicating dominance of dislocation type densification mechanisms. Pores around SCS-6 fiber show high variability in closure rate where matrix pores display narrow size distribution.

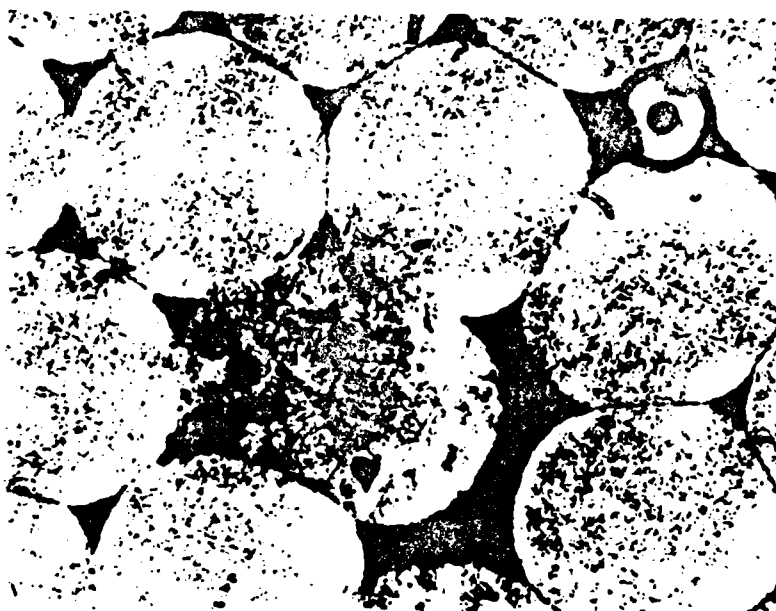
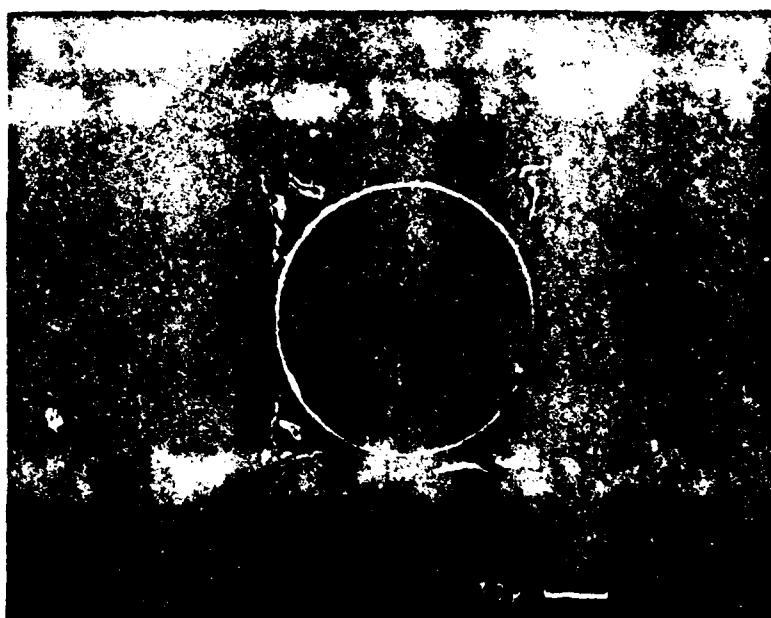
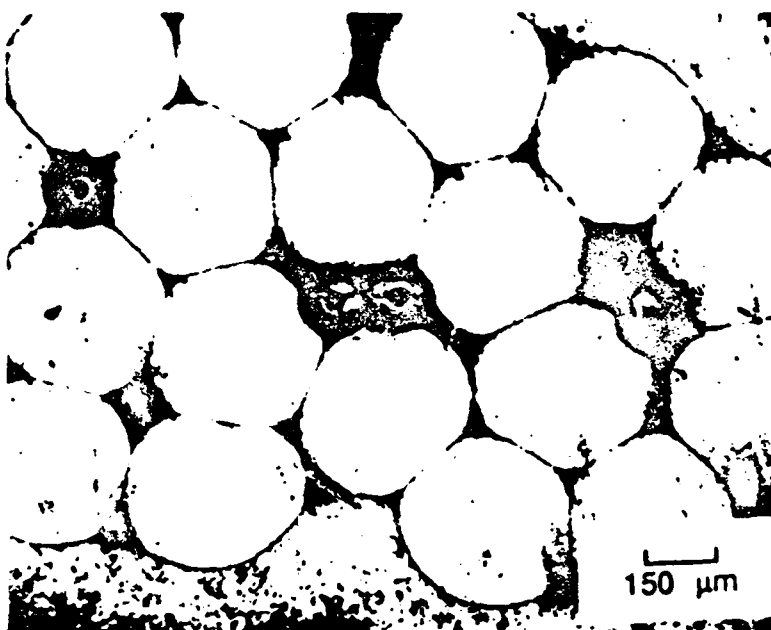


FIG. 4: 19 filament array of Ti-6Al-4V filaments with one CP Titanium filament and one SiC SCS-6 fiber. Deformation of CP Ti filament appears to indicate plastic flow mechanism since a higher diffusion coefficient is expected for the Ti-6Al-4V. (650 C and 10,000 psi)



**FIG. 5 A: 19 filament array with SiC SCS-6 reinforcement. Pores are filled with epoxy.**

**FIG. 5 B: Uniform pore size is observed around the single fiber and in the matrix.  
(650 C and 10000 psi)**

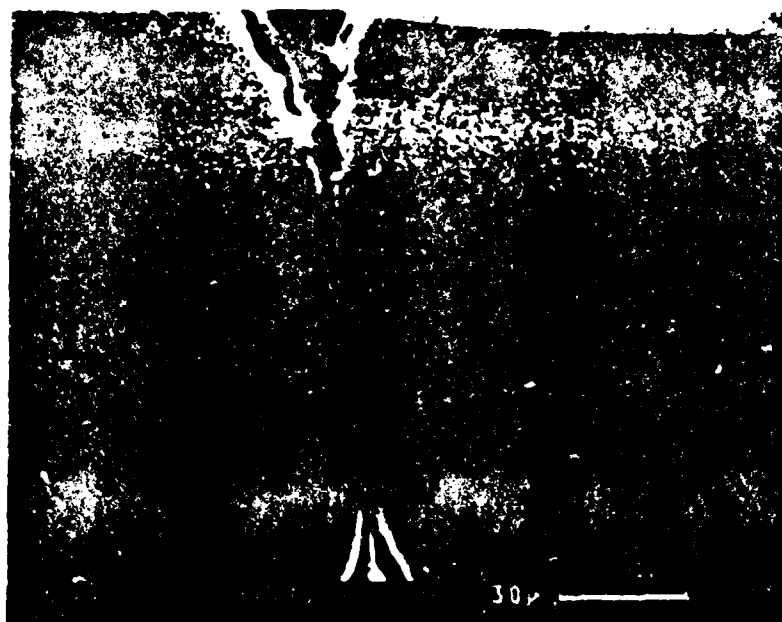
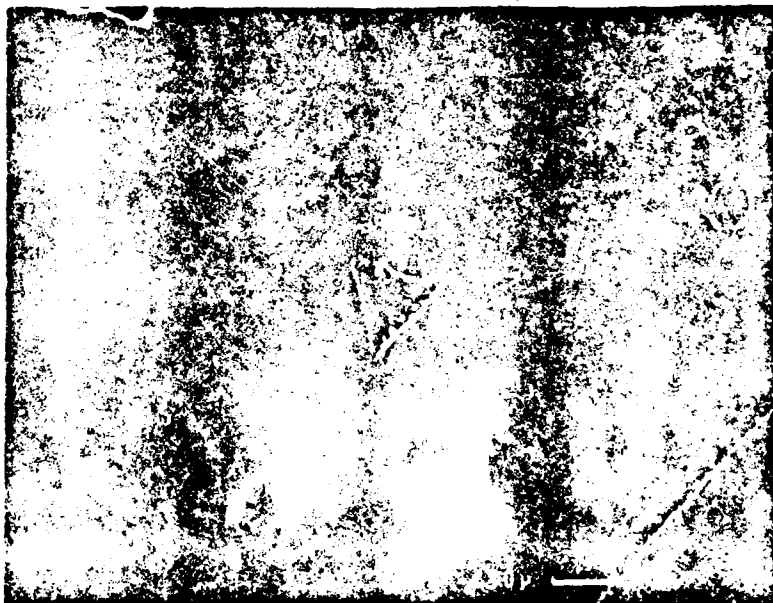


FIG. 6 A: Matrix Pore.

FIG. 6 B: Residual Porosity is observed on PPB's.  
(650 C and 10,000 psi)

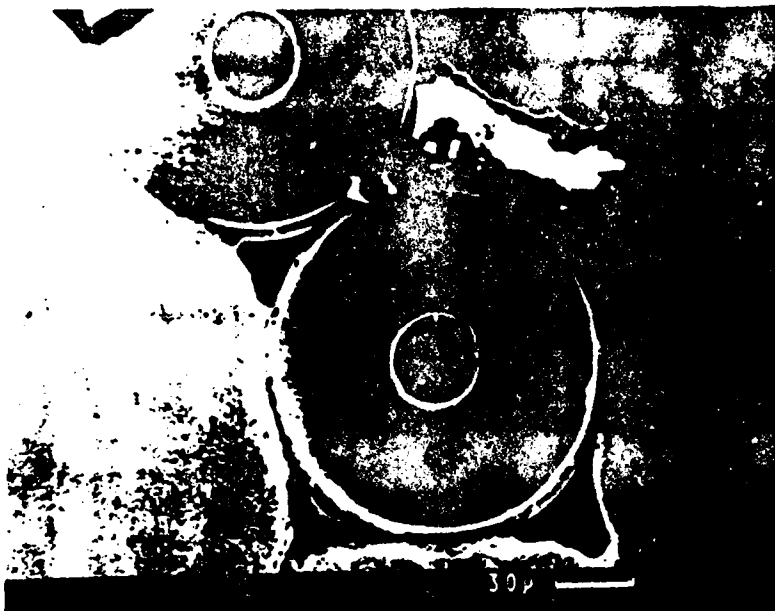
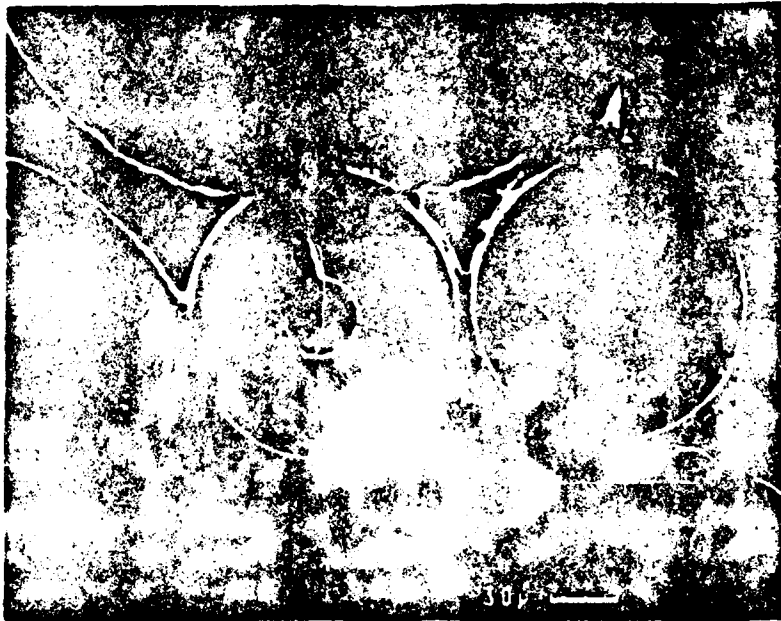
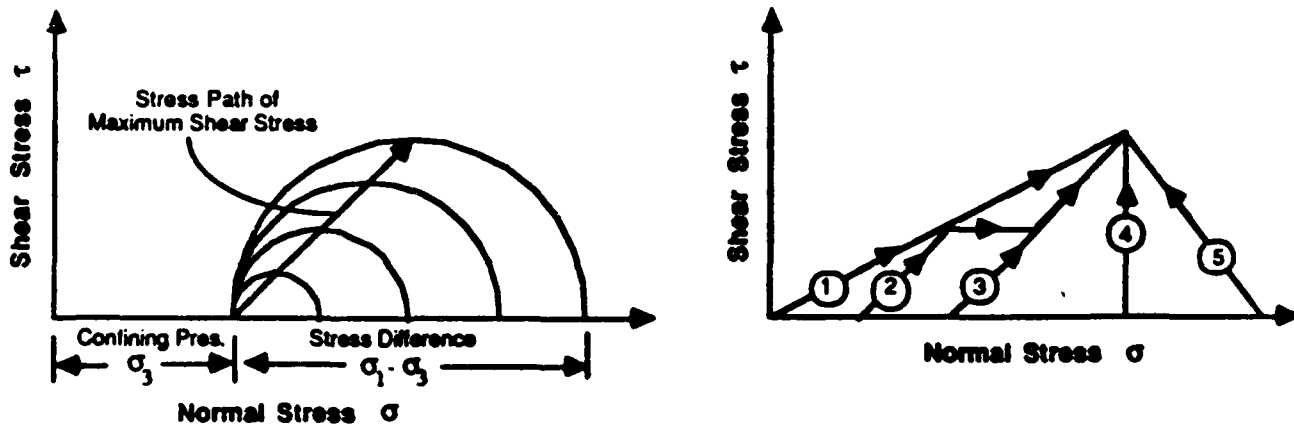


FIG. 7 A, 7 B: Adjacent filaments constrain consolidation. SCS-6 fiber damage appears to be processing related.

## TRIAXIAL STRESS STATES AND DEFORMATION PATHS USED BY KOERNER



(Compression is positive)

FIG. 8: Triaxial Processing Paths.

# TRIAXIAL STRESS/TEMPERATURE PATHS OBTAINABLE USING HOT TRIAXIAL COMPACTION

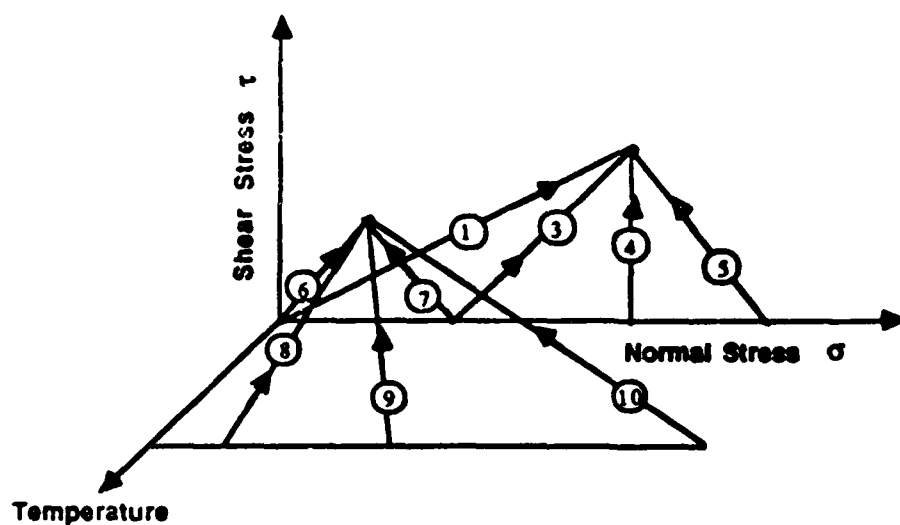


FIG 9: Hot Triaxial Processing Paths.



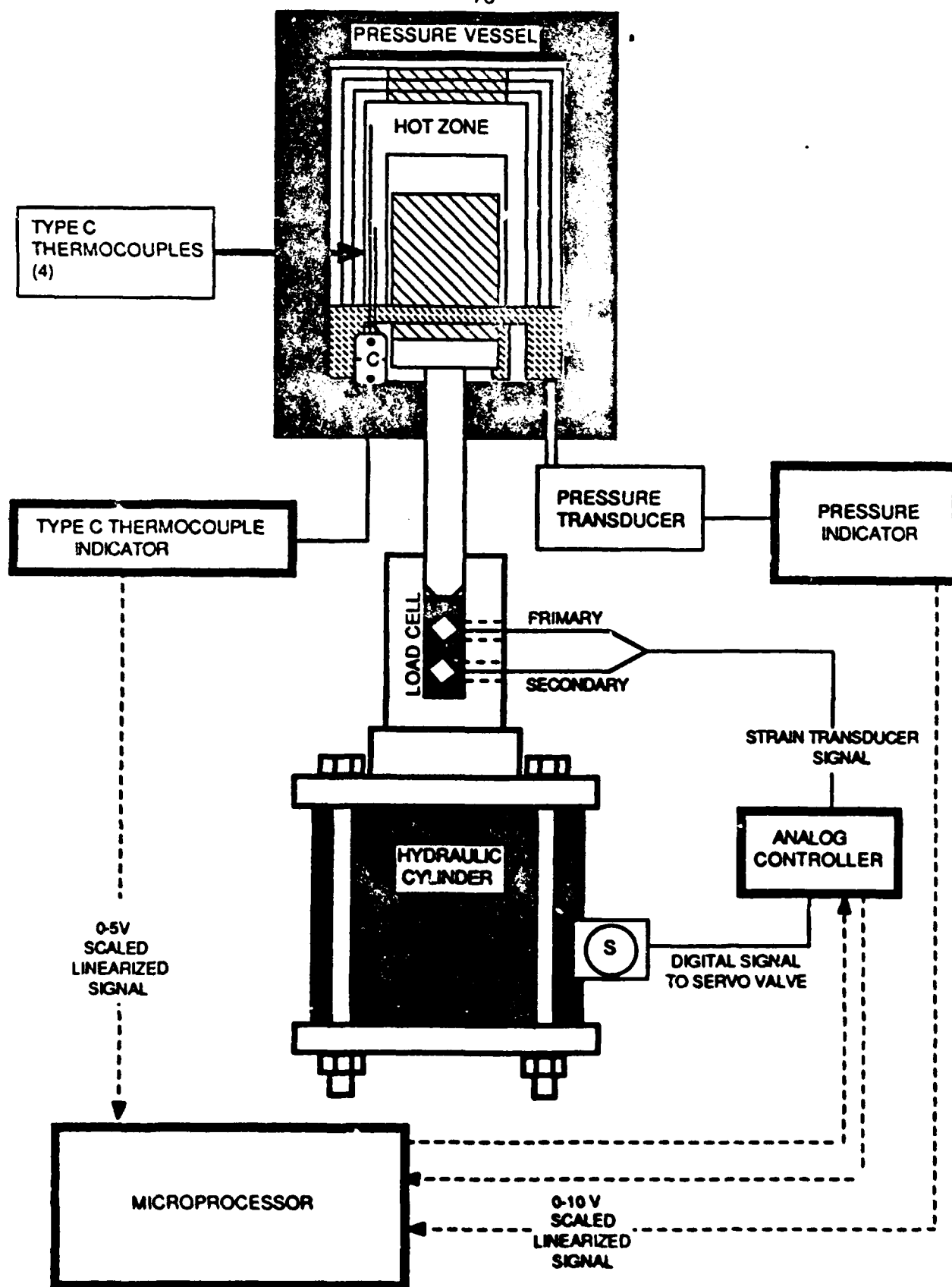


FIG. 10: HIP Control Systems.

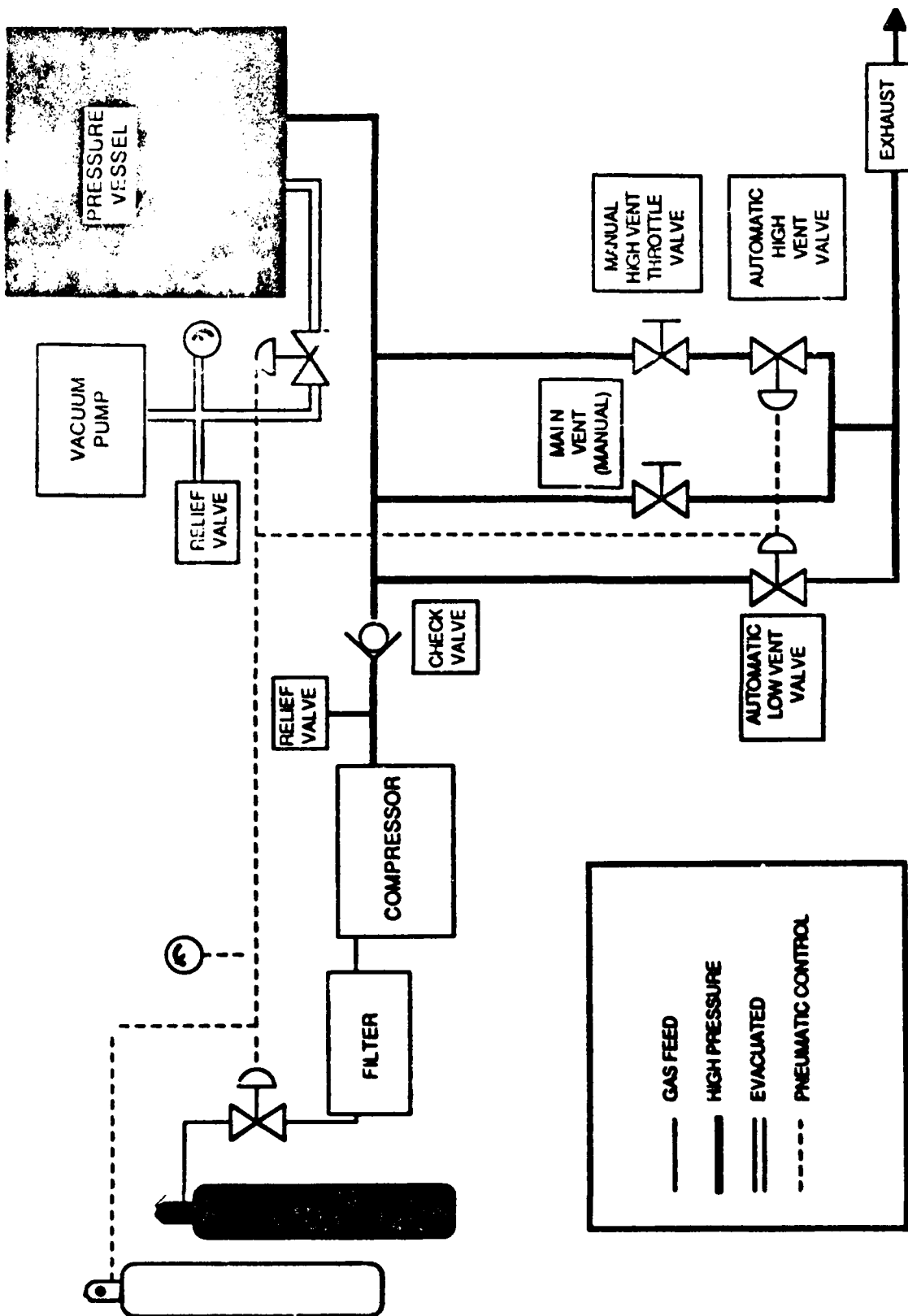


FIG 11: HIP Pressure Systems.

## **APPENDIX 1**

# PHYSICAL MODELING of METALWORKING PROCESSES

Proceedings of a symposium sponsored by the  
TMS-AIME Shaping and Forming Committee and  
held at the TMS Annual Meeting in Denver,  
Colorado, February 24-27, 1987.

Edited by

E. Erman

Bethlehem Steel Corporation  
Bethlehem, Pennsylvania

and

S.L. Semiatin

Battelle Columbus Division  
Columbus, Ohio

## HIP CONSOLIDATION OF SEVEN-FILAMENT ARRAYS OF ALUMINUM WIRES

K. Yoshida

Nippon Steel Corporation

Na-goya Works

5-3 Tokai-cho, Tokai Aichi, 476 Japan

T.E. Sleyer

D.M. Watkins

H.R. Pichler

Carnegie-Mellon University, Pittsburgh PA 15213.

### ABSTRACT

Seven-filament aluminum-wire arrays of varying diameters are encased in aluminum tubes and hot isostatically compacted. The objective of these experiments is to develop physical and analytical modeling methods to characterize densification mechanisms during the HIP process. Seven filament arrays of diameters ranging between 0.010 and 0.063 in. were compacted at 300° and 500° C using a pressure of 10 ksi. The initial results of these experiments reveal that no densification occurs at 300° C for all wire diameters and that the densification at 500° C is inversely proportional to wire diameter. These latter results indicate that the model geometry is indeed capable of distinguishing between densification by deformation, which should be independent of filament diameter, and densification by diffusional mechanisms, which should be strongly diameter-dependent. The background of physical modeling of powder-metallurgy systems, theoretical densification models, and additional scientific and technical applications for this seven-filament model configuration are discussed.



A Publication of The Metallurgical Society, Inc.

## INTRODUCTION

The basic elements of any deformation-processing system have been identified by Backofen<sup>1</sup>, who listed the following physical parts and associated problem areas:

- I. Continuous Plasticity
- II. Frictional Boundary Conditions
- III. Material Properties and Characteristics under Processing Conditions
- IV. Resolving Properties and Characteristics

The characterization and control of deformation-processing systems are ideally accomplished using a combination of both physical and analytical modeling. This dual approach to the characterization and control of deformation-processing systems is illustrated schematically in Figure 1 below.

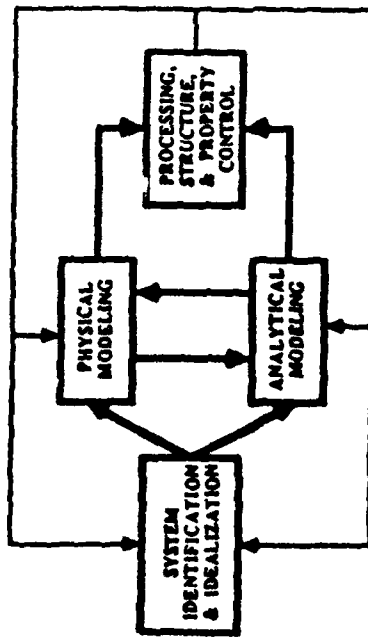


Figure 1

Prior to beginning any type of modeling, it is necessary to identify in appropriate detail the particular deformation-processing system to be characterized and controlled. While the delineation of system boundaries has been almost routine in the past, the combination of enhanced demands for product performance and the expanded capabilities for upstream and downstream integration of manufacturing processes has made this task less straightforward. However, the ultimate goal of any deformation-processing operation remains achieving the desired performance of the final component or product through the control of the processing parameters and resultant macrostructure and microstructure. The conjoint role of physical and analytical modeling in this process is illustrated schematically in Figure 1. The system identification and idealization leads naturally to the initial selection of physical and analytical modeling procedures. These two types of modeling efforts are enhanced by their mutual interaction, as illustrated by the two vertical arrows. The results of physical and analytical modeling can then achieve the desired goal of processing, structure, and performance control. Finally, the entire system operation can be further enhanced using the feedback indicated to refine the physical and analytical modeling procedures and perhaps even sharpen the identification and idealization of the deformation-processing system itself.

The initial results from such a conjoint physical and analytical modeling approach to deformation and property control via hot pressing of powder compacts are presented herein. This approach is based on the use of seven filament close-packed arrays. Previous physical and analytical modeling efforts in powder-metalurgy processing are reviewed below.

## BACKGROUND

### A. Physical Modeling

Physical modeling of powder consolidation has been used primarily to simulate mechanisms of sintering driven by temperature only. Here, we will review the principal experiments and their concomitant observations. The theoretical sintering mechanisms have evolved somewhat since Frenkel<sup>2</sup> (1945) proposed a single "viscous flow" mechanism driven by surface tension. In recent years, as a result of attempts to model the simultaneous application of temperature and pressure, such mechanisms as power law creep and plastic yielding have become important considerations.

Kuczynski<sup>3</sup> (1949) first considered multiple sintering mechanisms: viscous or plastic flow, evaporation and condensation, volume diffusion, and surface diffusion. In sintering copper and silver spheres (4 - 100 microns) to plates, an exponential relationship between neck growth and time was theoretically predicted to indicate dominant mechanisms. In the relationship

$$X^n = At,$$

the value of  $n$  will depend on the active mechanism (see Table 1). Kingery and Berg<sup>4</sup> (1950) refined the Kuczynski equations and sintered copper spheres (100 microns) together to verify their predictions. Both they and Kuczynski saw a neck growth dependence on time that indicated volume diffusion as the dominant mechanism.

Alexander and Balluffi<sup>5</sup> (1957) examined the sintering of copper with an array of fine wires wound around a spool. These studies revealed dramatic evidence for a grain-boundary controlled consolidation mechanism based on observations of preferential elimination of voids near grain boundaries. The authors divide the somewhat undefined viscous flow mechanism into plastic flow (viscous flow by dislocation motion) and Nabarro-Herring creep (viscous flow by diffusion). Also, it is noted that some mechanisms are capable of producing shrinkage while all can produce bonding. Alexander and Balluffi's results indicate the primary mechanism of densification is volume diffusion from grain boundary to the areas in the void with the lowest radius of curvature (cusps). This agrees with the conclusions of Kuczynski. They observed that the final densification rate at intermediate temperatures was higher than the densification rate at the higher test temperatures. Though the highest temperature specimens were observed to initially densify more rapidly, grain boundary elimination occurs sooner than for lower temperature specimens, thus slowing subsequent consolidation in the later stages. While not a dominant mechanism, there is also evidence of some capillarity driven transport from the convex void surface to the cusp occurs until spheroidization of the void (as discussed by Kuczynski). Acknowledged disadvantages of wire wound spools include:

- (1) the specimens are already at 90% density so shrinkage was relatively small compared to real powders which have a "loose" density in the neighborhood of 65%.
- (2) the specimens were not free of winding faults, and
- (3) relative particle sliding and readjustment are inadequately modeled.

Curvature is not a problem as Alexander and Balluffi provide a strong argument that the windings approximate a corresponding bundle of straight wires.

Ichinose and Kuczynski<sup>6</sup> (1962) focused on grain boundary effects during consolidation. By plating and recrystallizing copper on copper wires (0.005 in), necks without grain boundaries could be formed. Interestingly, the wires plated with a layer of Mo before plating with copper sintered at the same rate as those simply plated with copper. Thus a Mo layer did not appear to affect sintering mechanisms. The wires exhibited an exponential relationship

between neck growth and time that, again, indicates volume diffusion as the dominant mechanism. This is observed for both plated and unplated wires. The plated wires did sinter at a slower rate than the unplated wires. The researchers see this as evidence for grain boundaries acting as vacancy sinks. Also cited as further evidence for the role of grain boundaries in sintering was the observation that the centers of the wires with grain boundaries moved toward one another while those without grain boundaries did not. Likewise, the role of grain boundaries in sintering of ceramics is clearly demonstrated by Coble (1961) who obtained fully dense alumina only when suitable grain growth inhibitors and proper atmospheres were used. More recent theoretical work by Schott and Wieters (1986) proposes that the contact grain boundary between particles behaves differently from other grain boundaries. It appears that sintering is enhanced by the presence of a dislocation rich contact grain boundary.

Brett and Seigle (1966) also examined diffusional versus plastic flow effects in sintering. Using three wire arrays, the researchers studied marker motion, or lack of motion, as an indication of plastic flow or diffusion, respectively. The three wire arrays exhibited a variability in closure along the length of the compact, a problem that did not arise in the wire wound spools. In Ni-20 vol  $Al_2O_3$  (0.01 in. diameter), the pore and external cusps were observed to be free of marker material when sintered at 1400°C. In Cu-10 vol  $Al_2O_3$  (0.005 in. diameter), the same observation is made but densification is inhibited, compared to pure copper, by the presence of the  $Al_2O_3$  or possibly by dissolved Al or O. Lenel (1964) and coworkers, for example, have attributed this effect to resistance to dislocation motion by dispersion hardening, and take this as an indication of surface-tension driven plastic deformation. However, in later stages, the absence of marker material in the partially filled void would seem to contradict this. Also it should be noted that the grain size in the nickel is strongly affected by the dispersion, yet the rate of pore growth agrees extremely well with pure nickel wire sintering. Brett and Seigle conclude that diffusion appears to be the dominant mechanism in all but the earliest stages of sintering for materials with a high resistance to slip.

In response to Brett and Seigle, Lenel, Ansell, and Barron (1970) also used a twisted three wire array to investigate early stage marker transport in silver wires (100 - 180 microns). The markers were seen to move into the neck region in the earliest stages in a manner compatible with dislocation motion. The authors conclude that the early stage growth is dominated by the surface-tension driven dislocation motion and, as the neck grows, the surface tension decreases and diffusion dominates in later stages.

The bulk of the work on combined pressure and temperature consolidation mechanisms is in ceramic systems where certain flow mechanisms are not operative. The problem of pressure application and pressure integrity has prevented the kind of scaled-up physical modeling typical of pressureless sintering research. In a typical ceramics research program, Vasilos and Spriggs (1963) used pressure sintering to achieve full density. With pressure application, it was observed that consolidation could be achieved at lower temperatures. The low temperatures resulted in less grain growth, therefore, in the later stages where diffusion dominates, higher densification rates are observed. Thus, with pressure sintering, thermal exposures can be reduced in order to mitigate the problems of pore isolation caused by thermally activated grain growth.

## B. Analytical Modeling

While most of the research discussed in the physical modeling section above also involves analytical modeling, particularly the attempts to match experimental and analytical values of  $n$ , the more detailed analytical studies deserve separate discussion. This research is generally not accompanied by physical modeling and the data from the above papers are often used to substantiate these theories.

The most important result from these studies is the possible dominance of surface-diffusion densification. Nichols and Mullins (1965) carefully derived solutions

showing surface diffusion dominance for compacts with a certain particle size and volume diffusion dominance with larger sizes. The reasons for the apparent volume diffusion dominance in previous experiments are two fold:

- (1) multiple mechanisms are active and change with time, making the method of matching exponents unreliable and
- (2) detailed specimen geometry effects must be considered.

Ashby (1974) developed sintering diagrams showing mechanisms of densification for ranges of particle sizes and temperatures. The resultant mechanism maps generally bear out the conclusions of Nichols and Mullins in that they show that under the right set of conditions boundary, volume, or surface diffusion can dominate. The classical equations for pressureless sintering are presented in Table 1. The equations evolve from Kuczynski (3), to Wilson and Shewmon (20), to Ashby (14). Ashby modifies the geometry for Wilson and Shewmon's equations, uses the vapor transport model presented in Kingery and Berg (4) and derives stage 2 and 3 equations as well as an equation for lattice diffusion from dislocations.

The work of Helle, Easterling, and Ashby (1985) represents the most comprehensive analytical modeling of the combined pressure and temperature (i.e., HIPing) consolidation process. Maps of density and times to achieve density for various temperatures and pressures are generated. Such deformation-mechanism maps have the potential to design consolidation parameters without costly experimental characterization. The model assumes spherical, mono-sized particles, constant temperature, and constant hydrostatic pressure. The model simply superimposes the densification contributions from power law creep, plastic flow, and diffusional mechanisms. Both volume and grain-boundary mechanisms are considered in a simplified manner. Equations for the model are shown on Table 2.

It will be important to extend our ability to model the consolidation process to include shear stresses, second phase particles, non-constant temperature and pressure loads, and particle size distributions (16). Shear stresses are particularly interesting as their application can result in novel microstructures (17, 18) with potentially improved mechanical properties both because of the shear deformation and because of the potential for reduced thermal exposure required for consolidation. Also, in ceramic systems, imposed shear stresses have been observed to mitigate the problems of differential sintering in the consolidation of composite powders (19).

## EXPERIMENTAL PROCEDURE AND RESULTS

Aluminum (1199) wires were used to examine the effects of varying temperature and particle size on densification. Seven filaments were inserted into a cylindrical tube with an inner diameter approximately equal to three times the wire diameter so that close packing and good contact was achieved between the six outer wires and the tube inner diameter. The thickness of the two largest tube sizes was selected such that the cross-sectional area of the tube was equivalent to that of a hypothetical neat twelve wire layer. The smallest size compacts, 0.127 mm radius wire, were not sized this way because of difficulties in small tube production.

Since pure aluminum is easily oxidized and the layer of oxide may affect diffusional mechanisms, the specimens were carefully cleaned and polished before mounting. Wires and tubes were first cleaned by acetone and ethyl alcohol, then electrically polished in a solution of 20% perchloric acid plus 80% ethyl alcohol with a voltage of 8V for 30 seconds to 5 minutes depending on specimen size. The seven wire array was then mounted in the tube, the tube evacuated, and the compact hermetically sealed.

Two sets of three different size, 0.7875 mm, 0.508 mm, and 0.127 mm wire radius, were HIPed at temperatures of 300°C, and 500°C. The pressure with both temperatures was 10,000 psi.

Table 2: Equations for HIP Densification 15

MECHANISM	EQUATION
Immediate Plastic Flow	$D = 1 - \exp(-\frac{2}{3} \frac{P}{\sigma_y})$
Diffusion from Interparticle Boundaries	Initial Stage ( $D < 0.9$ ) $D = \frac{50(1-D_0)(16D_0 - \sigma D_0)}{(D_0 \sigma_y) \Delta TR}$ Final Stage ( $0.9 > D > 1$ ) $D = \frac{54(16D_0 - \sigma D_0)}{\Delta TR} \sqrt{D} P$
Power Law Creep	$D = 5.3 \sigma D_0^{\frac{1}{2}} \frac{1}{R} \left( \frac{D_0}{\sigma_y} \right)^{\frac{1}{2}} \left( \frac{P}{\sigma_y} \right)^{\frac{1}{2}}$
Nabarro-Herring and Coble Creep	$D = 24 \frac{9-11}{\Delta T G} \sigma D_0^{\frac{1}{2}} \frac{1}{R} \left( \frac{D_0}{\sigma_y} \right)^{\frac{1}{2}} \left( \frac{P}{\sigma_y} \right)^{\frac{1}{2}}$
Restrictions and Addends	$P_{eff} = \frac{P(1-D)}{D(1-D)}$

Table of Symbols

- $D_0$  = original tap density (~0.65)  
 $D$  = density, fraction of theoretical  
 $\delta$  = boundary thickness  
 $P$  = density  
 $D_b$  = diffusion coefficient for boundary diffusion  
 $D_s$  = diffusion coefficient for surface diffusion  
 $D_v$  = diffusion coefficient for volume diffusion  
 $\Omega$  = atomic volume  
 $P$  = applied pressure  
 $P_{eff}$  = effective pressure  
 $a, R$  = particle radius  
 $k$  = Boltzmann's constant  
 $T$  = temperature  
 $\bar{G}$  = average grain size  
 $x$  = neck radius  
 $L_0, n, n$  = creep parameters

Table 1: Classical Equations for Pressureless Sintering

Author	Equation	Author	Equation	Author	Equation
Kingery (1956, 1960)	$\dot{D} = \frac{64 \pi \gamma^3}{kT} \frac{D_s}{D_0} \quad (\text{surface plane})$	Kingery and Shyne (1960)	$\dot{D} = \frac{24 \pi \gamma^3}{kT} \frac{D_s}{D_0} \quad (\text{surface plane})$	Arly (1979)	Stage 1 $\dot{D} = \frac{64 \pi \gamma^3}{kT} \frac{D_s}{D_0}$
Kingery (1956)	$\dot{D} = \frac{64 \pi \gamma^3}{kT} \frac{D_s}{D_0} \quad (\text{surface plane})$	Arly (1979)	$\dot{D} = \frac{24 \pi \gamma^3}{kT} \frac{D_s}{D_0} \quad (\text{surface plane})$	Arly (1979)	Stage 2 & 3 $\dot{D} = \frac{64 \pi \gamma^3}{kT} \frac{D_s}{D_0}$
Kingery (1956)	$\dot{D} = \frac{64 \pi \gamma^3}{kT} \frac{D_s}{D_0} \quad (\text{surface plane})$	Arly (1979)	$\dot{D} = \frac{24 \pi \gamma^3}{kT} \frac{D_s}{D_0} \quad (\text{surface plane})$	Arly (1979)	Stage 2 & 3 $\dot{D} = \frac{64 \pi \gamma^3}{kT} \frac{D_s}{D_0}$
Kingery (1956)	$\dot{D} = \frac{64 \pi \gamma^3}{kT} \frac{D_s}{D_0} \quad (\text{surface plane})$	Arly (1979)	$\dot{D} = \frac{24 \pi \gamma^3}{kT} \frac{D_s}{D_0} \quad (\text{surface plane})$	Arly (1979)	Stage 2 & 3 $\dot{D} = \frac{64 \pi \gamma^3}{kT} \frac{D_s}{D_0}$
Kingery (1956)	$\dot{D} = \frac{64 \pi \gamma^3}{kT} \frac{D_s}{D_0} \quad (\text{surface plane})$	Arly (1979)	$\dot{D} = \frac{24 \pi \gamma^3}{kT} \frac{D_s}{D_0} \quad (\text{surface plane})$	Arly (1979)	Stage 2 & 3 $\dot{D} = \frac{64 \pi \gamma^3}{kT} \frac{D_s}{D_0}$
Kingery (1956)	$\dot{D} = \frac{64 \pi \gamma^3}{kT} \frac{D_s}{D_0} \quad (\text{surface plane})$	Arly (1979)	$\dot{D} = \frac{24 \pi \gamma^3}{kT} \frac{D_s}{D_0} \quad (\text{surface plane})$	Arly (1979)	Stage 2 & 3 $\dot{D} = \frac{64 \pi \gamma^3}{kT} \frac{D_s}{D_0}$
Kingery (1956)	$\dot{D} = \frac{64 \pi \gamma^3}{kT} \frac{D_s}{D_0} \quad (\text{surface plane})$	Arly (1979)	$\dot{D} = \frac{24 \pi \gamma^3}{kT} \frac{D_s}{D_0} \quad (\text{surface plane})$	Arly (1979)	Stage 2 & 3 $\dot{D} = \frac{64 \pi \gamma^3}{kT} \frac{D_s}{D_0}$
Kingery (1956)	$\dot{D} = \frac{64 \pi \gamma^3}{kT} \frac{D_s}{D_0} \quad (\text{surface plane})$	Arly (1979)	$\dot{D} = \frac{24 \pi \gamma^3}{kT} \frac{D_s}{D_0} \quad (\text{surface plane})$	Arly (1979)	Stage 2 & 3 $\dot{D} = \frac{64 \pi \gamma^3}{kT} \frac{D_s}{D_0}$
Kingery (1956)	$\dot{D} = \frac{64 \pi \gamma^3}{kT} \frac{D_s}{D_0} \quad (\text{surface plane})$	Arly (1979)	$\dot{D} = \frac{24 \pi \gamma^3}{kT} \frac{D_s}{D_0} \quad (\text{surface plane})$	Arly (1979)	Stage 2 & 3 $\dot{D} = \frac{64 \pi \gamma^3}{kT} \frac{D_s}{D_0}$

HIPed specimens were mounted in acrylic then cut and polished for metallographic examination. Photomicrographs of the cross sections of these samples were taken. Neck radius and pore fractions were measured from the photomicrographs. The fractional porosity (density) was determined by measuring the pore areas adjacent to the central filament and dividing this by the area of the triangle formed by joining the centers of the three filaments adjacent to the pore in question. A representative micrograph for the 0.7875 mm array after compaction is shown in Figure 2. The initial results from these experiments are shown in Figure 3.

While there is considerable scatter in these data, the results for HIPing at 500°C indicate that consolidation is indeed dependent upon fiber diameter. This supports the initial hypothesis that the seven filament geometry is a viable physical model for the separating and characterizing in detail the effects of deformation and sintering during powder compaction.

The scatter in the data comes from several sources. The most important source is the presence of irregular gaps between wires prior to HIPing. Steps are being taken to eliminate gaps by drawing the filament containing tubes prior to HIPing so that these gaps are eliminated. Another source of data scatter could be differential surface contamination, particularly in light of aluminum's tendency to form surface oxides. Current experiments are being conducted using titanium wires to alleviate this difficulty.



Figure 2.  
Pores in Seven Filament Array after HIPing.  
Initial diameter of filaments is 1.5750 mm.  
HIPed for 20 minutes at 500°C and 10,000 psi.

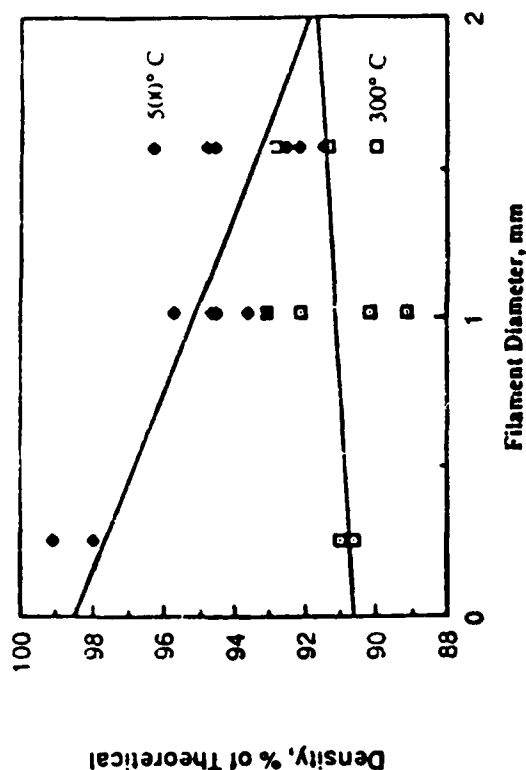


Figure 3.  
HIPed Density as a Function of Filament Diameter and Temperature.  
HIPed for 20 minutes at 10,000 psi.

## CONCLUSIONS

1. Initial experimental results indicate that the seven filament geometry of various diameters is a viable physical model for studying densification during HIPing.
2. These initial experimental results are sufficiently encouraging to employ the seven filament geometry to study densification using other monolithic and composite materials and other stress states, e.g., those involving shear stresses as well as hydrostatic pressure.



## REFERENCES

- (1) W. A. Backofen, *Deformation Processing* (Addison-Wesley Pub. Co. 1972).
- (2) J. Frenkel, *J. Phys. U.S.S.R.* (1945) 9, No. 3, 385.
- (3) G. C. Kuczynski, *Self-Diffusion in Sintering of Metallic Particles*, ADME Trans. 185(1949), 169-178.
- (4) W. D. Kagury and M. Berg, *Study for the Initial Stages of Sintering Solids by Viscous Film, Evaporation and Condensation, and Self-Diffusion*, *J. Appl. Phys.* 24(1950), 1205-1212.
- (5) B. H. Alexander and R. W. Balluffi, *The Mechanism of Sintering of Copper*, *Acta Met.* 5(1957), 466-477.
- (6) M. Schuster and G. C. Kuczynski, *The Role of Grain Boundaries in Sintering*, *Acta Met.* 10(1962), 209-213.
- (7) W. Schuster and R. P. Wenzel, *On the Nature of the Sintering Compact Zone*, *Powder Met. Int.* 18, no. 3(1966), 135-139.
- (8) B. Cabot, *in Sintering and Related Phenomena* (1965), Gordon and Breach Pub., Kuczynski, Newark, Gibbon, eds. 329.
- (9) J. Eddy, F. Leoni, G. Averb, *The Mutual Transport Mechanism During Sintering of Copper-Powder Compacts at High Temperatures*, *Trans. ASME* 230(1964), 1641.
- (10) J. Bone and L. Singh, *The Role of Diffusion versus Plastic Flow in the Sintering of Metal Compacts*, *Acta Met.* 14(1966), 575-582.
- (11) F. Leoni, G. Averb, and D. Berman, *Marker Transport During the Early Stages of Sintering*, *Met. Trans.* 1(1970), 1772-1773.
- (12) T. Vianello and B. M. Spragg, *Pressure Sintering: Mechanisms and Microstructures for Aluminas and Magnesia*, *J. Am. Cer. Soc.* 44(1963), no. 10, 493-496.
- (13) F. A. Nichols and W. W. Mullins, *Surface- (Interface-) and Volume-Diffusion Contributions to Morphological Changes Driven by Capillarity*, *Trans. ADME* 233(1965), 1840-1848.
- (14) M. F. Addy, *A First Report On Sintering Diagrams*, *Acta Met.* 22(1974), 375-389.
- (15) A. S. Mills, E. E. Bunting and M. F. Addy, *Hot Isostatic Pressing Diagrams: New Developments*, *Acta Met.* 33(1985), no. 12, 2163-2174.
- (16) S. V. Huet and J. E. Tate, *Deformation Mechanism Maps for Hot Uniaxial Pressing of Unequal Sized Particles*, *Met. Trans.* 18A(1987), 97-107.
- (17) C. M. Smith, *Consolidation of Rapidly Solidified Titanium by Hot Isostatic Pressing*, *Met. Sci. and Eng.* 9(1987), 105-117.
- (18) W. Smalley, W. Bush, R. Kopp, *Combined Die Forging (CDF) of Prealloyed Ti-6Al-4V Powder*, *Proc. 5th Int. Conf. on Titanium*, Munich (1984), 367-377.
- (19) E. B. Venzke and R. Raj, *Enhancement of Strength through Sinter Forging*, *J. Am. Ceram. Soc.* 70(1987), no. 7, 514-520.
- (20) T. L. Wilson and P. O. Skovranek, *The Role of Interfacial Diffusion in the Sintering of Copper*, *Trans. ADME* 234(1966), 48-58.

## **APPENDIX 2**

**Hot Triaxial Consolidation of Powder Compacts:**

H. R. Piehler, D. M. Watkins, M. A. Khuni, Carnegie Mellon University,  
Pittsburgh, Pa. 15213

Triaxial consolidation of powders has been studied in a hot isostatic press (HIP) modified to impose an additional axial compressive force. The uniaxial compressive force imbalances the hydrostatic stress state and superimposes a shear stress during compaction. This novel process allows for fully general loading on the compact in that the shear and hydrostatic components may be controlled independently. Triaxial compaction differs from sinter forging where the shear and hydrostatic components are inherently coupled during compaction. Increased densification and improved mechanical properties have been observed in metallic and ceramic powders consolidated with shear superimposed on the conventional hydrostatic stress. Effects of processing paths involving different trajectories in temperature, pressure, and shear stress space are described. Initial experimental results for model systems, Ti-6Al-4V and ceramics, consolidated for a range of processing trajectories and rates are presented and discussed in terms of the operative micromechanisms and macroscopic flow during consolidation.

To be presented at the TMS Annual Meeting, Forming of Advanced Materials,  
Las Vegas, Feb. 28, 1989.

## **Hot Triaxial Compaction: A First Report on Shear Plus Hydrostatic Pressing Diagrams and Initial Experimental Results**

**Henry R. Piehler and Daniel M. Watkins**  
Professor and Graduate Student, respectively  
Deformation Processing Laboratory  
Department of Metallurgical Engineering & Materials Science  
Carnegie Institute of Technology  
Carnegie Mellon University  
Pittsburgh, PA 15213-3890

Described herein is a novel compaction process, hot triaxial compaction, which utilizes controlled levels of both shear and hydrostatic stress to consolidate compacts at elevated temperatures. The shear component is imposed by applying an axial force (tension or compression) via a ram and movable seal in a modified hot isostatic pressing (HIPing) unit. This hot triaxial compaction system is capable of achieving a pressure of 60,000 psi, a temperature of 1200° C, and an axial force of 50,000 lb.

The principal benefits of hot triaxially compacting monolithic materials are enhanced densification (at constant time, temperature, and pressure) resulting from shear-induced deformation as well as enhanced performance in the resulting compact. Enhanced performance can result from improved particle bonding caused by increased shear-induced interparticle sliding during compaction. In addition, enhanced performance can be achieved by retarding the decomposition of unstable microstructures by triaxially compacting at lower temperatures than those required to achieve the same density using conventional HIPing; in essence, trading shear stress for temperature to achieve the same density. Hot triaxial compaction of composites can also be used to reduce the extent of reaction zones by compacting at lower temperatures to achieve comparable densities, again trading shear stress for temperature. In addition, hot triaxial compaction of powder-matrix short fiber composites should reduce fiber fracture during consolidation because of the enhanced plasticity of the matrix compared to that during HIPing.

The effect of shear stress on the identification of the dominant densification mechanism is characterized by modifying the traditional hot pressing diagrams to include shear stress as a third dimension. Some initial results for these shear plus hydrostatic pressing diagrams are presented.

Initial results for hot triaxially compacted composites fabricated using short SiC fibers and Ti-6Al-4V powders are presented as well.

Submitted for presentation at the: **Second International Conference on "Hot Isostatic Pressing - Theory and Applications"**



## TASK 2

### High Temperature Structural Materials

H.J. Rack, Investigator

Task 2 of the URI on High-Temperature Metal Matrix Composites, the task title of which is "Modeling of Consolidation and Deformation Processing of Composites", is being conducted at Clemson University, and has three sub-tasks. The Annual Report for this Task consists of separate summaries for each of the three sub-task projects. They are listed below, with the titles of the summaries reflecting the topics of the individual projects. The first sub-task addresses the need to understand and improve interfacial behavior and control of bonding between reinforcements and matrix in metal matrix composites. The second is a preliminary investigation of titanium aluminide alloys, including those of Ti-Al-V composition as well as the more widely studied Ti-Al-Nb-V alloys, with the intent to apply this knowledge to development of aluminide-matrix composites. The third sub-task is a study of a model composite, TiC reinforced Inconel 718, in which the matrix alloy is a well-studied and widely-used nickel-base superalloy of intermediate temperature capability, and with particulate reinforcements of TiC, which is relatively stable in 718.

	Page
<b>SUB-TASK 1</b>	
"Interfacial Modification in Metal Matrix Composites"	
J.P. Clement, K.T. Wu, H.G. Spencer and H.J. Rack	92
<b>SUB-TASK 2</b>	
"Elevated Temperature Plastic Flow and Fracture of Multi-phase Alloys and Composites"	
E. F. Wachtel, J. Wung and H.J. Rack	125
<b>SUB-TASK 3</b>	
"Phase Stability and Aging Response of TiC Reinforced Inconel 718"	
E. F. Wachtel and H.J. Rack	135

INTERFACIAL MODIFICATION  
IN METAL MATRIX COMPOSITES

J.P. CLEMENT,  
K.T. WU, H.G. SPENCER, H.J. RACK  
Materials Engineering Activity  
Department of Mechanical Engineering  
Clemson University  
Clemson, South Carolina

## INTRODUCTION

The influence of exposure temperature and time on fiber-matrix interactions in metal matrix composites has been examined for almost twenty years. Repeated thermodynamic calculations indicate that fiber-matrix reactions are the rule, rather than the exception. Calculations shown in Figure 1 illustrate, for example, that reactions of elemental C(graphite) with elemental Al and Ti are thermodynamically favored over a wide range of temperatures. Furthermore,  $Al_4C_3$  formation at a graphite(C)/Al interface results in a marked reduction in the fiber's strength<sup>1</sup>. Exposure of PITCH and PAN-based graphite fibers to molten aluminum at 680°C for two minutes results in a decrease of 10 and 50 percent, respectively, in the fiber's tensile strength<sup>2</sup>.

Investigations of both Al and Ti-based continuously reinforced metal matrix composites do suggest however that the details of reaction layer growth are system specific, as summarized for Ti-based metal matrix composites in Table 1. In addition, examination of the SiC/Ti results show that these reactions are extremely sensitive to fiber pre-treatment. For example, the introduction of a C-rich layer drastically reduces the rate of layer growth in SiC reinforced composites<sup>4</sup>. However, once this C-rich region is consumed, the rate of growth returns to that of the uncoated fiber<sup>5</sup>. Unfortunately, this sensitivity also makes direct comparisons and correlations between systems, and between different investigators extremely difficult. For example, Tressler et. al.<sup>9</sup> suggested that the reactivity of selected fibers with a Ti-40A matrix could be rated in the order, from highest to lowest, SiC- $Al_2O_3$ -B, while Kennedy and Geschind's results<sup>10</sup> suggest that this order should be  $Al_2O_3$ -B-SiC for reactions observed in a similar Ti-70A matrix.



TABLE 1

Interfacial Reactions in Continuous Fiber Reinforced  
Titanium Metal Matrix Composites

System	Max. Reaction Temp. (°C)/Time(h)	Reaction Products	Ref.
SiC/Ti-6Al-4V	1000/(a)	Ti <sub>5</sub> Si <sub>3</sub> (TiC)/TiC	3
SiC/Ti-6Al-4V	955/10	(a)	4
SiC(SCS-6)/Ti-6Al-4V	900/100	TiC, Ti <sub>5</sub> Si <sub>3</sub> /TiC(Ti <sub>5</sub> Si <sub>3</sub> )/Ti <sub>5</sub> Si <sub>3</sub>	5
SiC /Ti	1150/8	TiC	6
SiC/Ti-6Al-4V	950/1	TiC/Ti <sub>5</sub> Si <sub>3</sub>	7
Al <sub>2</sub> O <sub>3</sub> /Ti		Ti <sub>3</sub> Al/TiO-type (Ti,Al) <sub>2</sub> O <sub>3</sub>	8
/Ti-6Al-4V		"	8,9
/Ti-8Al-1V-1Mo	926/70	"	8
/Ti-6Al-2Sn-4Zr-2Mo	926/70	"	8
/70A, 75A	1000/100	(Ti <sub>3</sub> Al/Ti <sub>2</sub> Al/TiAl)	10
B/Ti-40A	1038/7000	TiB <sub>2</sub>	11
/Ti-75A		"	
B/Ti-Si, Sn, Cu, Cr, Al, Mo, Zr, V (b)	760/100	"	
Borsic/Ti-6Al-4V	955/10	(a)	4
B <sub>4</sub> C-B/Ti-6Al-4V	955/10	(a)	4
W/Ti-75A	1000/100	Ti-W Eutectoid	10
/Ti-75A	930/		11
C/Ti-70A	(a)	TiC	10

(a) NG-Not reported  
(b) Exact composition not given

While the details of fiber preparation, prior to incorporation into a metal matrix composite, have often not been provided, the kinetics of layer growth, once this layer has been established, has been found to obey a parabolic rate law, where the thickness,  $x$ , of the reaction layer can be described as a function of the exposure time,  $t$ , by, <sup>12,13</sup>

$$x^2 = K [\exp (-Q/RT)] t$$

where  $n$ , the parabolic index is a function of matrix crystal structure,  $K$  is a constant whose value depends upon the matrix composition and crystal structure and includes diffusional pre-exponential terms,  $Q$  is the activation energy,  $R$  is the gas constant and  $T$  is the absolute temperature. Detailed examination of kinetic data suggests that it should be possible to develop either a matrix composition or interfacial barrier coating which retards fiber-matrix interactions.

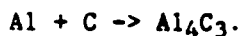
Two previous attempts utilizing the former approach in Ti-based metal matrix composites have been reported<sup>12,14</sup>. Metcalf and Klein<sup>12</sup> found that  $\beta$  isomorphous alloying additions were most effective in retarding fiber-matrix interactions. Guzel et. al.'s more recent study<sup>14</sup> has reinforced this conclusion and has suggested that the search for compatible titanium matrices be extended "outside the  $\alpha + \beta$  region".

Alternatively, fiber surface coatings have attracted detailed attention. Coatings have been designed to promote wetting, while simultaneously provide a barrier against excessive fiber-matrix interaction. These coatings may, in addition, facilitate load transfer between the matrix and the fibers and could, in theory, serve as mechanical fuses to isolate, by interface delamination, any impinging reaction zone cracks.

Of necessity, the coating should be homogenous and have a minimal thickness. The latter criteria is particularly important since previous studies have shown that the tensile strength of coated fibers decrease with increasing layer thickness<sup>15-19</sup>. Finally, the coatings' coefficient of thermal expansion should be tailored to that of the matrix in order to minimize residual stresses at the fiber-matrix interface.

Many fiber coating techniques have been examined. For example, TiC and TiB<sub>2</sub> coatings on C and C on SiC have been applied successfully by chemical

vapor deposition (CVD), and most continuous metal matrix composites are produced utilizing this approach<sup>20,21</sup>. The coatings produced by CVD have been found to effectively promote wetting and bonding between, for example, SiC and Al/Mg/Ti<sup>22,23</sup>, graphite fibers and Al/Mg<sup>24,25</sup>. TiB<sub>2</sub> coatings are effective because they mitigate the reaction between graphite and the metal matrix, B on the C surface reducing the number of available active sites for the reaction<sup>26</sup>:



In contrast, TiC coatings are thermodynamically stable with respect to Al<sub>4</sub>C<sub>3</sub> formation<sup>27</sup>.

Although CVD processing has been successfully utilized for both C and SiC fibers, it is limited in the barrier compositions that can be applied. Furthermore, at least for C fibers, the TiB<sub>2</sub> coating is not air stable.

Recently, Katzman et al.<sup>21,28-30</sup>, have reported the development of a simpler method for producing an air stable C fiber coating. The coating procedure utilizes a sol-gel process, whereby C fibers are passed through an organometallic solution, the organometallic compounds pyrolyzed or hydrolyzed to form an SiO<sub>2</sub> metal oxide coating.

This approach appears to offer a major advance over CVD processes and is the basis for the research reported herein. Emphasize in this investigation has been placed on TiO<sub>2</sub> sol coating of C fibers for inclusion in either an Al or a high temperature titanium aluminide matrix.

#### EXPERIMENTAL PROCEDURES

Two sol-gel coating strategies have been pursued in this investigation. The first involved hydrolysis of metal ions dissolved in acidic water

solutions. Following dissolution, the pH was increased, as the pH increased the degree of polymerization of the hydrous metal oxide increased, the polymer solubility decreased and a gel was formed.

Continued increase of the pH however contributed to floc formation, i.e., aggregation of primary particles. Coating of a surface with a continuous uniform thickness of hydroxide requires that gelation be intercepted prior to floc formation. Unfortunately, initial experiments using glass slides and carbon fibers produced coatings that appeared to be collection of flocs, that is individual particles, rather than a uniform coating. Attempts to overcome this barrier by utilizing very dilute metal ion concentration, e.g.,  $10^{-4}$  M, were also unsuccessful. Further study utilizing a metal alkoxide in an alcohol solvent suggests that floc formation is catalyzed by  $H_2O$ , therefore future attempts to develop directly hydrolyzed sols will be directed towards non-aqueous solvents.

The second strategy utilized in this study involved synthesis of metal oxides from metal alkoxides in non-aqueous solvents; the more common sol-gel procedure.  $TiO_2$  sol coatings were selected for study in this investigation. This selection was based upon the thermodynamic stability of  $TiO_2$  with respect to  $TiC$  formation, see Table 2, the known ability of Ti to enhance the wettability between metals and ceramics<sup>31,32</sup>, and finally its ready availability in the form of a metal alkoxide precursor, titanium isopropoxide (TIP).

Early experiments indicated that control of environment is extremely critical in controlling the hydrolysis reaction, indeed the reaction appears to be initiated by atmospheric moisture. Therefore, all coating experiments were performed in a nitrogen controlled atmosphere dry box, Figure 2.

Table 2  
Thermodynamic Stability of Selected Oxides with  
Respect to Carbide Formation

Oxide	Temp. (°C) for $\Delta G^\circ = 0$
$\text{Al}_2\text{O}_3$	1925
$\text{HfO}_2$	1750
$\text{ZrO}_2$	1730
$\text{SiO}_2$	1475
$\text{TiO}_2$	1200

Glass slides were utilized for many of the initial coating experiments. These slides had previously been cleaned following the procedures outlined in Table 3. These experiments were supplemented by coating C vapor deposited slides, the latter intended to simulate a C fiber surface. Finally, coating

Table 3  
Glass Slide Cleaning Procedure

- Rinse with water
- Immerse in approximately 3M nitric acid
- Rinse with Water
- Immerse in isopropanol
- Store

trials were performed utilizing unsized high strength PAN and PITCH base carbon fibers, AMOCO T650/42 and AMOCO P100S, Figure 3. The mechanical and physical properties of these uncoated fibers are listed in Table 4.

Table 4  
Carbon Fiber Properties\*

Fibers	Tensile Strength KPsi	Young's Modulus MPsi	Tensile Strength MPsi	Young's Modulus GPa	Density g/cc	Diameter $\mu\text{m}$
T 300	522	34	3.6	234	1.77	6.8
T 650/42	760	44	5.2	304	1.80	5.1
P 55S	275	55	1.9	380	2.15	10.1
P 100S	325	105	2.2	724	2.00	9.7

\* All fibers are shear treated and unsized

Prior to actual coating, extensive investigations of solution stability were undertaken. These studies included examinations of the role of  $\text{H}_2\text{O}$ /alkoxide ratio, molarity, acid content and temperature on stability. Solution stability was assessed by measurements of the solution's specific viscosity and turbidity as a function of time.

All coating was performed utilizing a controlled dipping process where the velocity of withdrawal from the coating solution was fixed. Following dipping the coated samples were introduced into a humidity controlled oven at  $60^\circ\text{C}$ , so that the coatings were simultaneously aged, and in part dried. Selection of this drying temperature, as well as the subsequent firing temperature was based on preliminary DSC and TGA evaluations, Figure 4. These results revealed that drying occurs between room temperature and  $200^\circ\text{C}$ , with a maximum desorption of the solvents at  $125^\circ\text{C}$ . Above  $200^\circ\text{C}$ , the

desorption of the solvents is complete, the constant slope on the DSC curve probably being due to the carbonization of the remaining OR groups. The TGA observations confirm that the maximum weight loss, 25 percent, occurs during drying, with the weight loss between 200°C and 400°C being smaller, approximately 5 percent. Above 400°C the weight loss is negligible.

Following drying, coated samples were fired at 300°C for 15 minutes to complete the conversion of the coating from a gel to a ceramic, this transformation being confirmed by X-ray analysis.

Coating thickness was assessed, both prior to firing and following firing, utilizing UV spectroscopy and Fizeau interferometry. In addition, coating uniformity was assessed by scanning electron microscopy, assisted by EDAX chemical analysis.

Finally, qualitative changes in fiber wettability, as influenced by coating, were evaluated by liquid metal vacuum infiltration of C fiber preforms by pure aluminum. This procedure used a special pressurized autoclave, Figure 5. Operationally, this procedure utilizes pressurized gas to force molten metal into a fiber preform, the threshold pressure for infiltration initiation being correlated with the wettability<sup>33</sup>. For example,  $P_c$ , the capillary pressure necessary to raise a liquid column in a capillary of radius,  $r$ , is be given by:

$$P_c = ( 2 * \gamma_{lv} * \cos \theta ) / r$$

where  $\gamma_{lv}$  is the liquid-vapor interfacial energy, and  $\theta$  is the wetting angle. When liquid is forced through the fiber preform by an applied pressure, a threshold pressure must be exceeded before flow commences. This threshold pressure can be measured and converted into contact angle values by replacing  $r$  with the hydraulic radius  $r_h$  ( $r_h$  = volume of liquid in the pore space divided by the wetted area)<sup>34</sup>.

Optical and transmission electron microscopy were also utilized to examine fiber-metal interactions in these pressure infiltrated composites containing coated and uncoated fibers.

## RESULTS

### Solution Stability

Figure 6 shows that increasing H<sub>2</sub>O content, at fixed titanium isopropoxide (TIP) molarity, does not have a marked effect on the rate of change in turbidity with solution aging time. However, increased H<sub>2</sub>O content does drastically decrease the solution stability, the latter being defined as the time required for a step-wise change in the turbidity. Visual observations confirmed that this step-wise change is associated with a clouding of the solution, presumably thru the agglomeration of colloidal particles.

Solution stability can also be controlled by altering the acid concentration and solution temperature, Figures 7 and 8, respectively. For example, increasing the acid concentration to  $2.8 \times 10^{-3}$  m/l, at a fixed TIP molarity and fixed TIP to H<sub>2</sub>O ratio, increases the solution stability from less than 1 hr. to greater than 3 hrs. Further, decreasing the solution temperature from 40°C to 20°C, increases the solution stability from approximately 26 minutes to approximately 45 minutes. Based on these results a solution chemistry of TIP = 0.3 m/l, an acid content of  $8 \times 10^{-3}$  m/l and a TIP to H<sub>2</sub>O ratio of 10, operated at 30°C, were selected for coating evaluation.

### Coating Evaluation

As described previously, coating evaluation involved vertical withdrawal of cleaned glass slides from the TIP solution. Figure 9 shows that as the



speed of the withdrawal increases, at least within the range of withdrawal speeds examined in this study, the thickness of the coating produced increases. Furthermore, this data indicates that an approximate 30 percent reduction in thickness should be expected when a dried coating is fired. For instance, the thickness of a coating that had been dried for 10 min. at 60°C, decreased from 120nm to 104nm when fired at 300°C for 15 minutes. The use of higher firing temperatures, e.g., 500°C versus 300°C, only slightly alter (densification, sintering) the final coating thickness.

Coating thicknesses can also be controlled by altering the TIP concentration and the number of dips, Figures 10 and 11. For example, increasing either the solution molarity or the number of dips increases the coating thickness. Figure 11 further suggests that the original surface energy has a role, albeit a seemingly secondary one, on the coating thickness. The initial dip resulted in a surface coating thickness of 25nm, while each subsequent dip resulted in an increase in thickness of 45nm. Similar conclusions can be made from the C coated slides, where under identical conditions, fired sol coatings were thinner than might be expected from the clear glass slide results.

#### Carbon Fiber Coating

Carbon fiber coating utilized the dipping procedures previously established for the glass slides, with the fibers being dipped as tows, 12000 filaments for the PAN base and 2000 filaments for the Pitch base fibers. Initially the withdrawal speed was 24 cm/min, and the alkoxide concentration was  $\text{TIP} = 0.3 \text{ mol/l}$ . Although these conditions had previously produced 80nm crack free uniform coatings on carbon coated glass slides, the fiber tows were not coated uniformly, the dipping solution being trapped between fibers by capillary forces. As a result, coatings after drying were much thicker

and many fibers were glued to each other by metal hydroxide bridges, Figure 12. Firing caused these coatings to crack.

Reduction of the solution concentration to 0.03mol/l completely eliminated the formation of bridges, Figure 13, with the presence of  $TiO_2$  on the fiber surface being confirmed by EDAX analysis, Figure 14.

Finally, Figure 15 demonstrates the qualitative enhancement in fiber wettability that can be achieved by sol coating of the graphite fibers. Uncoated fibers tend to clump during pressure infiltration, Figure 15(a), while coated fibers are dispersed within the pure Al matrix, Figure 15(b).

### DISCUSSION

Metal alkoxides are known to react vigorously with water to produce metal hydroxides. The reactions are complex but can be represented for simplicity in two steps.

#### Hydrolysis



#### Condensation

##### dealcoholation



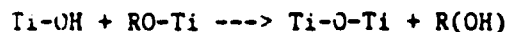
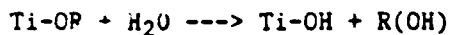
##### dehydration



These reactions occur simultaneously making it difficult to separate the hydrolysis and condensation steps, with the overall reaction being:



In analogy with  $SiO_2$  sols, the hydrolysis-condensation of titanium isopropoxide (TIP) is expected to yield an oxide network, i.e.,



with the degree of polymerization being controlled by TIP to  $\text{H}_2\text{O}$  ratio, solution molarity, temperature and acid content. In general, the degree of polymerization in TIP sols appears to be controlled by the TIP to  $\text{H}_2\text{O}$  ratio as long the ratio is less than the stoichiometric value<sup>35</sup>. The coating microstructure will, in turn, depend on the pH of the solution. If an acid, as in the present investigation, is used as a catalyst the polymer chains grow in a more linear fashion; therefore, the final polymer film will cover the substrate more efficiently and will be less likely to crack. In contrast, if a base had been added to the solution the final coating would have been more like a juxtaposition of particles loosely attached. The coating would, therefore, have been more porous and more sensitive to cracking<sup>36</sup>.

The turbidity results further suggest that as the TIP solution ages the degree of polymerization increases with the sol being converted to a polymer network with more and more crosslinks. Maximum coating efficiency, that is the development of a thin uniform coating, is associated with partially aged TIP solutions. Once coated, evaporation of the solvent, drying, can be started at any time. During this stage the polymer network shrinks as fast as the solvent evaporates. If the network is not stiff enough, i.e., it has not been aged long enough, it will collapse and crack during drying. Because it increases the coating strength, aging before drying also presents one method of minimizing the coatings' tendency to crack.

Further, the current study has shown that air stable  $\text{TiO}_2$  coated C fibers may be formed at low temperature, that is all processing being carried

out at temperatures below 300°C. By controlling the solution concentration, pH, temperature, and time of immersion it is possible to control the uniformity and the thickness of the resultant oxide coating. A given thickness can be obtained many different ways, for example, multiple dipping in a low alkoxide concentration solution.

Finally, preliminary data suggests that TiO<sub>2</sub> coatings can enhance the wettability of C fibers. Currently ongoing transmission electron microscopy is designed to examine what, and to what extent reactions may have occurred during pressure infiltration of TiO<sub>2</sub> coated C fibers.

#### REFERENCES

1. L. Xiangun, Z. Hanlin, and W. Renjie, "The Effect of Long Period Heat-Treatment on Carbon Fiber Reinforced Aluminium Composite," Fifth International Conference on Composite Materials, 1985, W. Harrigan, J. Strife, and A. Dhingra, eds., The Metallurgical Society, Warrendale, PA., pp. 623-629.
2. S. Kohara and N. Muto, "Degradation of Carbon Fibers by Molten Aluminium," Fifth International Conference on Composite Materials, 1985, W. Harrigan, J. Strife, and A. Dhingra, eds., The Metallurgical Society, Warrendale, PA., pp. 631-638.
3. H. J. Dudek, R. Leucht, and G. Ziegler, "Auger Electron Spectroscopy of the Interface of SiC Fiber Reinforced Titanium Alloys," Titanium Science and Technology, G. Lutering, U. Zwicker, and W. Bunk, eds., Deutsche Gesellschaft fur Metallkunde, Munich, FRG, 1985, pp. 1773-1780.
4. T. E. Steelman, R. H. Lorenz, G. R. Martin, and R. P. Robelotto, Silicon Carbide/Titanium Material and Process Fundamentals, AFWAL-TR-82-4036, May, 1982.
5. C. G. Rhodes and R. A. Spurling, "Fiber-Matrix Reaction Zone Growth Kinetics in SiC-Reinforced Ti-6Al-4V as Studied by Transmission Electron Microscopy," Recent Advances in Composites in the United States and Japan, J. R. Vinson and M. Taya, eds., ASTM STP 864, ASTM, Philadelphia, Pa., 1985, pp. 585-599.
6. E. P. Zironi and H. Poppe, "Micro-area Auger Analysis of a SiC/Ti Fibre Composite," Jn. of Materials Science, Vol. 16, 1981, pp. 3115-3121.
7. H. J. Dudek, L. A. Larsen, and R. Browning, "Study of the Fiber/Matrix Interface in a SiC Reinforced Titanium Alloy Using a High Resolution Field Emission Auger Microprobe," Surface and Interface Analysis, Vol. 6, 1984, pp. 274-278.

8. R. E. Tressler, T. L. Moore, and R. L. Crane, "Reactivity and Interface Characteristics of Titanium-Alumina Composites," Jn. of Materials Science, Vol. 8, 1973, pp. 151-161.
9. R. E. Tressler and T. E. Moore, "Mechanical Property and Interface Reaction Studies in Titanium-Alumina Composites," Metals Engineering Quarterly, Vol. 11, 1971, pp. 16-21.
10. J. Kennedy and G. Geschwind, "Interfacial Reactions in Potential Titanium Matrix Composites," Titanium Science and Technology, R. I. Jaffee and H. M. Burte, eds., Plenum Press, New York, 1973, pp. 2299-2312.
11. J. Kennedy, "Reaction Zones in Ti/W Composites," Jn. of Materials Science, Vol. 8, 1973, pp. 291-294.
12. A. G. Metcalf and M. J. Klein, "Compatible Alloys for Titanium Matrix Composites," Titanium Science and Technology, R. I. Jaffee and H. M. Burte, eds., Plenum Press, New York, 1973, pp. 2285-2298.
13. A. G. Metcalf, "Physical Chemical Aspects of the Interface," Composite Materials, A. G. Metcalf, ed., Academic Press, New York, 1974, Vol. 1, pp. 67-123.
14. L. S. Guzei, E. M. Sokolovovskaya, L. L. Tachunichina, V. I. Shulepov, and T. A. Tshemleva, "The Interaction Between Titanium Alloys and SiC-Fibers," Titanium '80, Science and Technology, H. Kimura and O. Izumi, eds., The Metallurgical Society, Warrendale, PA., 1980, pp. 2301-2308.
15. K. Honjo and A. Shindo, "Influence of Carbide Formation on The Strength of Carbon Fibers on which Silicon and Titanium have been Deposited," Jn. Mat. Sci., Vol. 21, pp. 2043-2048.
16. Y. Murakami, K. Nakao, A. Shindo, and K. Honjo, "Effect of Interfacial Conditions on the Tensile Strength of Carbon Fiber-6061 Aluminium Alloy Composites," Composite 86: Recent Advances in Japan and the United States, K. Kawata, S. Umekawa, and A. Kobayashi, eds., Tokyo, 1986, pp. 761-766.
17. K. Honjo and A. Shindo, "Interfacial Behavior of Aluminium Matrix Composites Reinforced with Ceramics-Coated Carbon Fibers," Composite Interfaces, H. Ishiba and J. L. Koenig, eds., North Holland Publ., New York, 1986, pp. 101-107.
18. A. Shindo, "Chemical Property of Carbon Fiber Surface and Interfacial Compatibility of Composites," Composite Interfaces, H. Ishiba and J. L. Koenig, eds., North Holland Publ., New York, 1986, pp. 93-100.
19. V. E. Ovcharenko and O. A. Kashin, "Effect of the Surface Structure of Carbon Fibers on their Strength in the Application of a Carbide Coating in a Metal Melt," Sov. Powder Metall. Mat. Ceram., Vol. 20, 1981, pp. 564-567.

20. S. D. Tsai, M. Schmerling, and H. L. Marcus, The Interface Structure in Graphite/Aluminium Composites, The University of Texas, Mechanical Eng. Dept., Austin, TX 78712. To be published in Ceramic Eng. and Science.
21. H. A. Katzman, Fiber Wetting and Coatings for Composite Fabrication, Aerospace Corp., El Segundo, Report No. TR-0086A (2935-14)-1; SD-TR-86-63, 15 Oct. 86, 35p.
22. L. D. Brown, B. Maruyama, Y. M. Cheong, L. K. Rabenberg, and H. L. Marcus, "Metal Matrix Interfaces and their Impact on the Mechanical Behavior of Components," Composite Interfaces, H. Ishiba and J. L. Koenig, eds., North Holland Publ., New York, 1986, pp. 27-36.
23. W. D. Brewer and J. Unnam, "Metallurgical and Tensile Property Analysis of Several Silicon Carbide/Titanium Component Systems," Mechanical Behavior of Metal-Matrix Components, J. E. Hack and M. F. Amateau, eds., The Metallurgical Society, Warrendale, PA, 1983, pp. 39-50.
24. T. G. Nieh and A. E. Vidoz, "Carbide Coatings on Graphite Fibers by Liquid Metal Transfer Agent Method," Jn. Amer. Ceramic Soc., Vol. 65, 1982, Materials and Mechanics Research Center; AMRC TR 72-32; AD 754-570; Oct. 1972.
25. M. Richman, A. Levitt, and E. Di Cesare, Some Atomistic Observations on the Role of Titanium in Magnesium Graphite Fiber Composites, Army Materials and Mechanics Research Center; AMRC TR 72-32; AD 754-570; Oct. 1972.
26. B. Maruyama and L. Rabenberg, "Oxidation Model of Interface Reactions in Aluminium Graphite Composites," Interfaces in Metal Matrix Composites, A. Dhingra and S. Fishman, eds., The Metallurgical Society, Warrendale, PA., 1986, pp. 233-238.
27. R. Imprescia, L. Levinson, and R. Reiswig, Carbide Coated Fibers in Graphite Aluminium Composites, Los Alamos Scientific Laboratory, NASA, Report AMRC TR 71-44; (NAS126); 1973.
28. H. Katzman, "Fibre Coatings for Fabrication of Graphite-Reinforced Magnesium Composites," Jn. Mat. Sci., Vol. 22 1987, pp. 144-148.
29. H. A. Katzman, "Carbon-Reinforced Metal Matrix Composites," United States Patent, 43766803, Mar. 15, 1983.
30. H. A. Katzman, "Pyrolyzed Pitch Coatings for Carbon Fiber," United States Patent, 43766804, Mar. 15, 1983.
31. M. J. Bennett, "Application and Evaluation of Ceramic Coatings Produced by Sol-Gel Technology and Vapor Deposition Procedures," Coatings for High Temperature Application, E. Lang, ed., Applied Science Publishers, New York, 1983, pp. 169-192.
32. A. Levitt, E. Di Cesare, and S. Wolf, Fabrication and Properties of Graphite Fiber Reinforced Magnesium, Army Materials and Mechanics Research Center; AMRC TR 71-44; AD 735-313; Nov. 1971.

33. J. A. Cornie, A. Mortensen, and M. C. Fleming, "Wetting, Fluidity and Solidification in Metal Matrix Composite Castings: a Research Summary," Sixth International Conference on Composite Materials, F. L. Matthews, N. C. R. Buskell, J. M. Hodgkinson, and J. Morton, eds., Elsevier Applied Science, London, 1987, Vol. 2, pp. 2.297-2.319.
34. L. J. Masur, A. Mortensen, J. A. Cornie, and M. C. Flemings, "Pressure Casting of Fiber-Reinforced Metals," Sixth International Conference on Composite Materials, F. L. Matthews, N. C. R. Buskell, J. M. Hodgkinson, and J. Morton, eds., Elsevier Applied Science, London, 1987, Vol. 2, pp. 2.320-2.330.
35. D. C. Bradley, R. E. Mehrotra, and D. P. Gaur, Metal Alkoxides, Academic Press, New York, 1978.
36. C. J. Brinker and G. W. Scherer, "Gelation and Gel Structures," Jn. of Non-Crystalline Solids, Vol. 70, 1985, pp. 301-

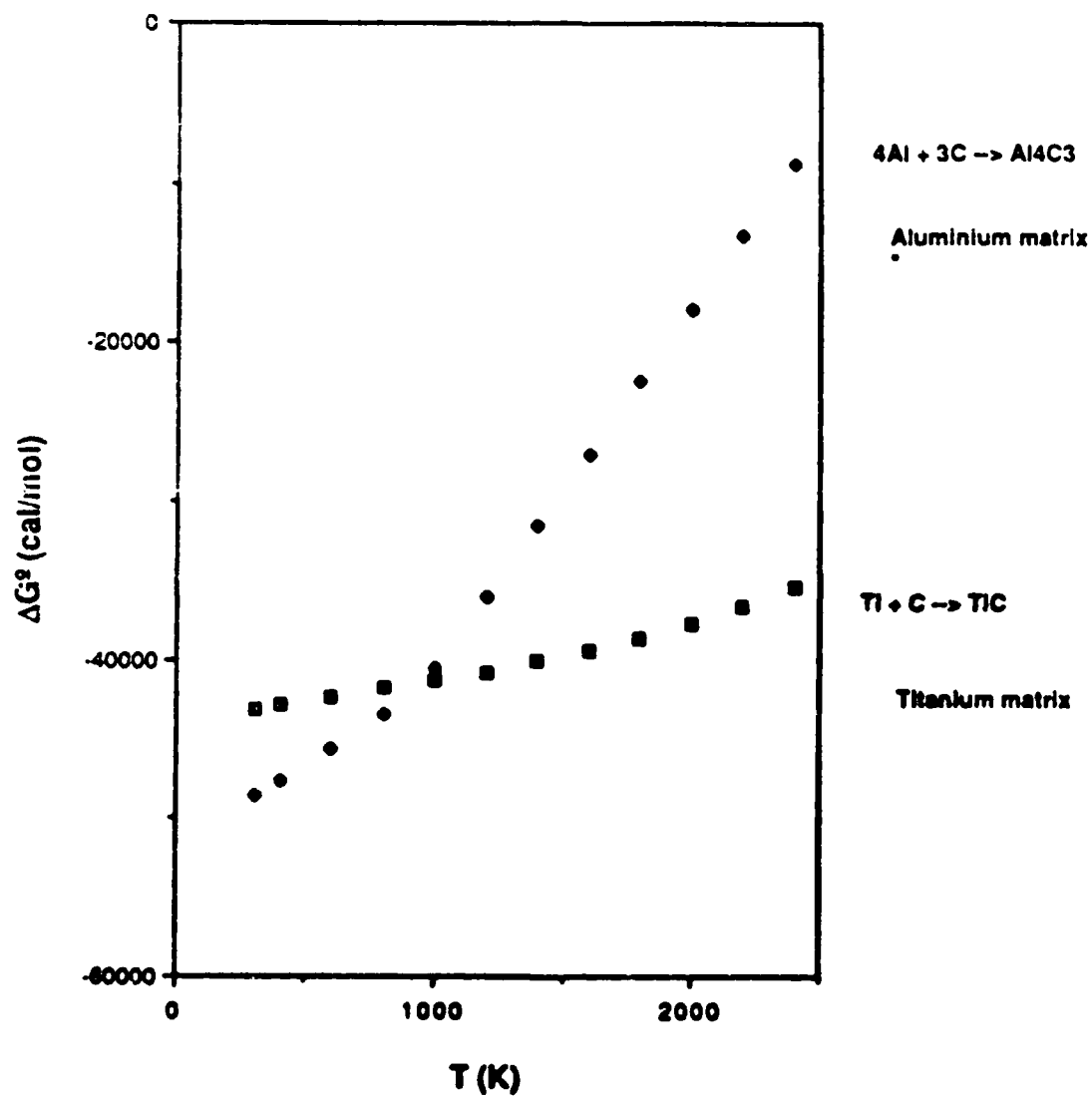


Figure 1: Free energy of formation of  $\text{Al}_4\text{C}_3$  and  $\text{TiC}$  as a function of temperature.



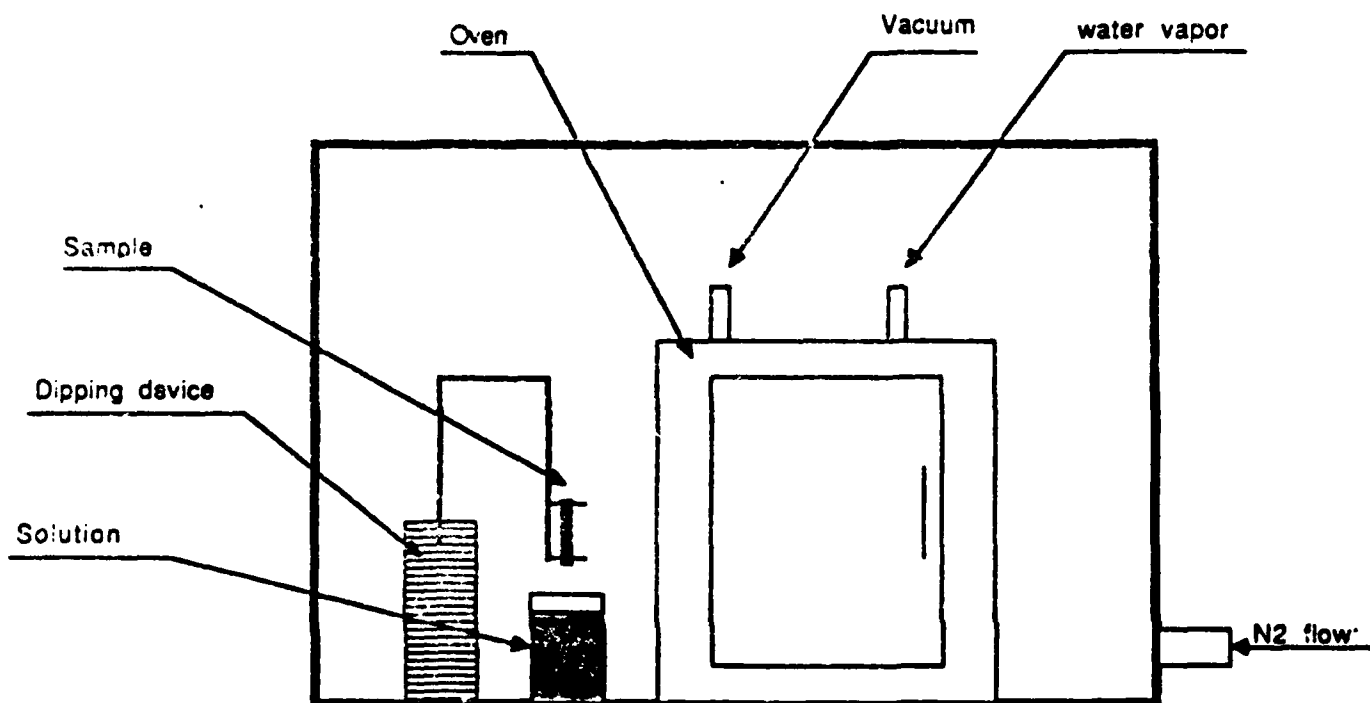


Figure 2: Schematic Illustration of Coating Process

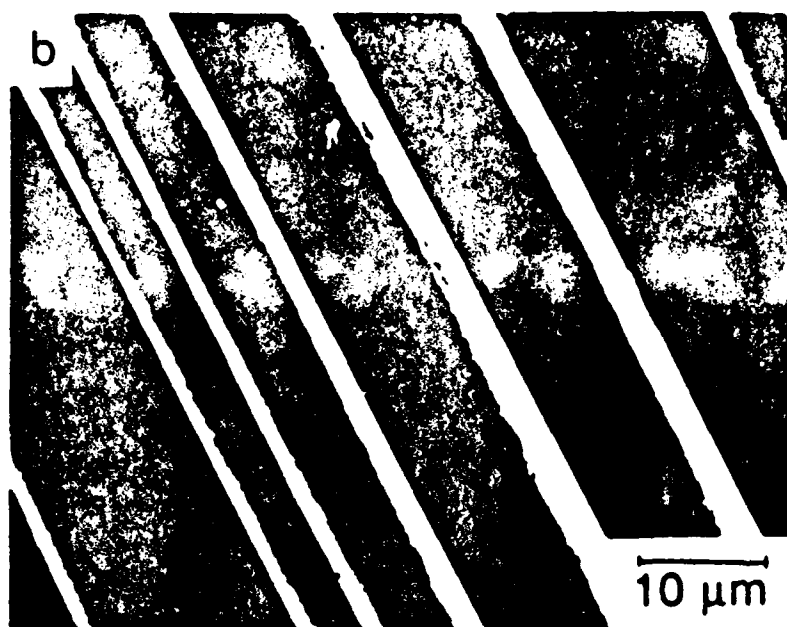
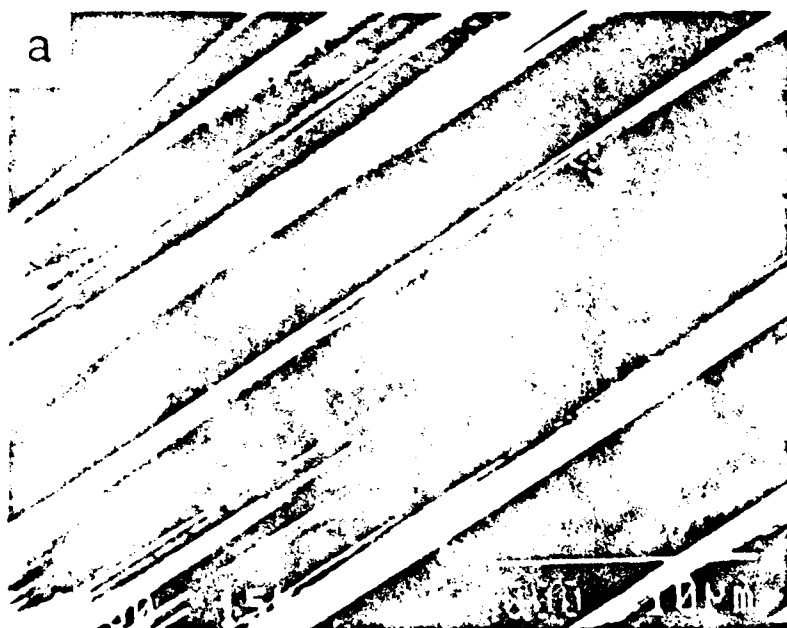


Figure 3 Scanning electron micrographs of unsized (a) PAN 650/42 and (b) Pitch 100S

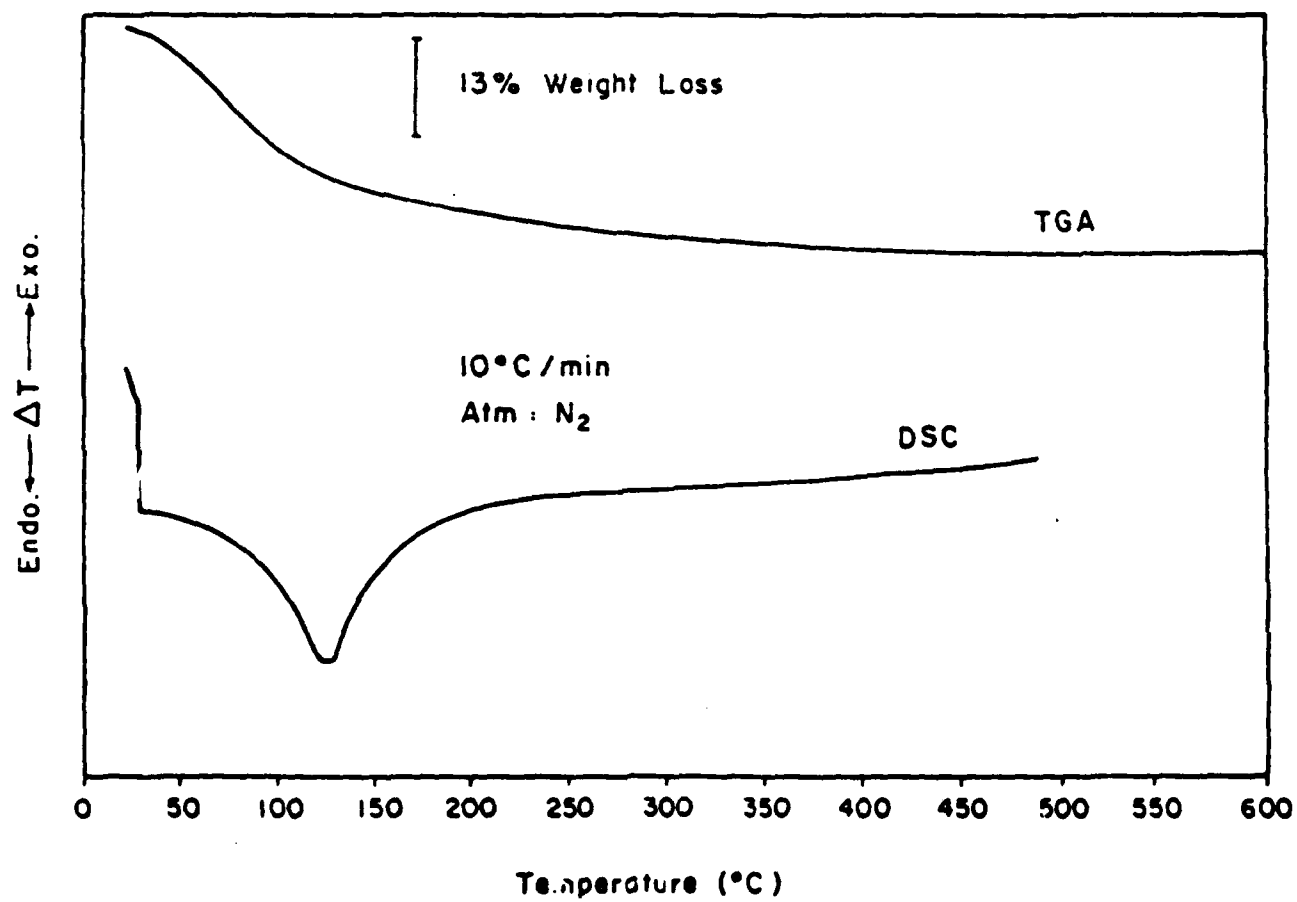


Figure 4: Thermal Analysis of dried  $\text{TiO}_2$  gel.

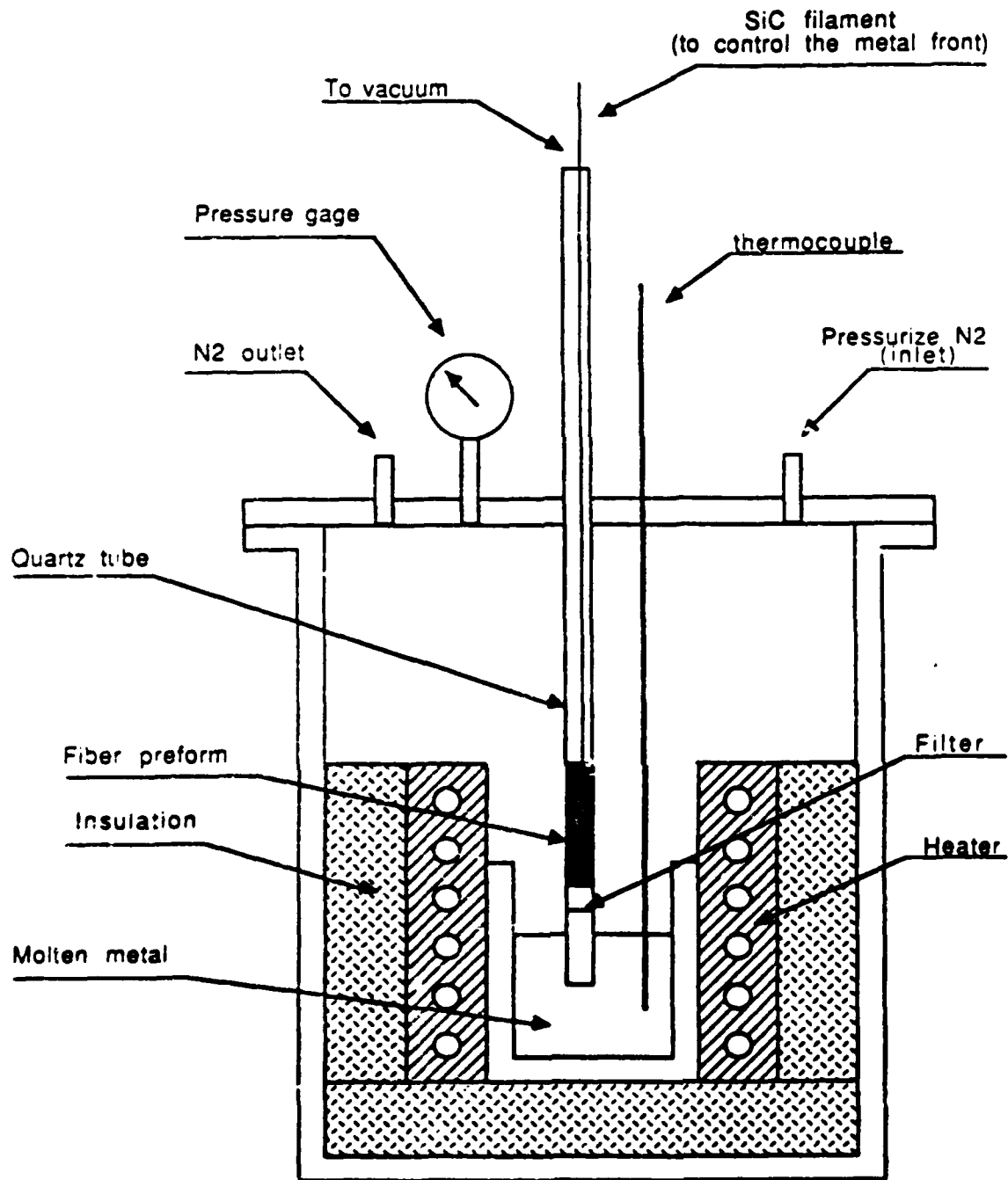


Figure 5: Schematic Diagram of Pressure Infiltration Apparatus

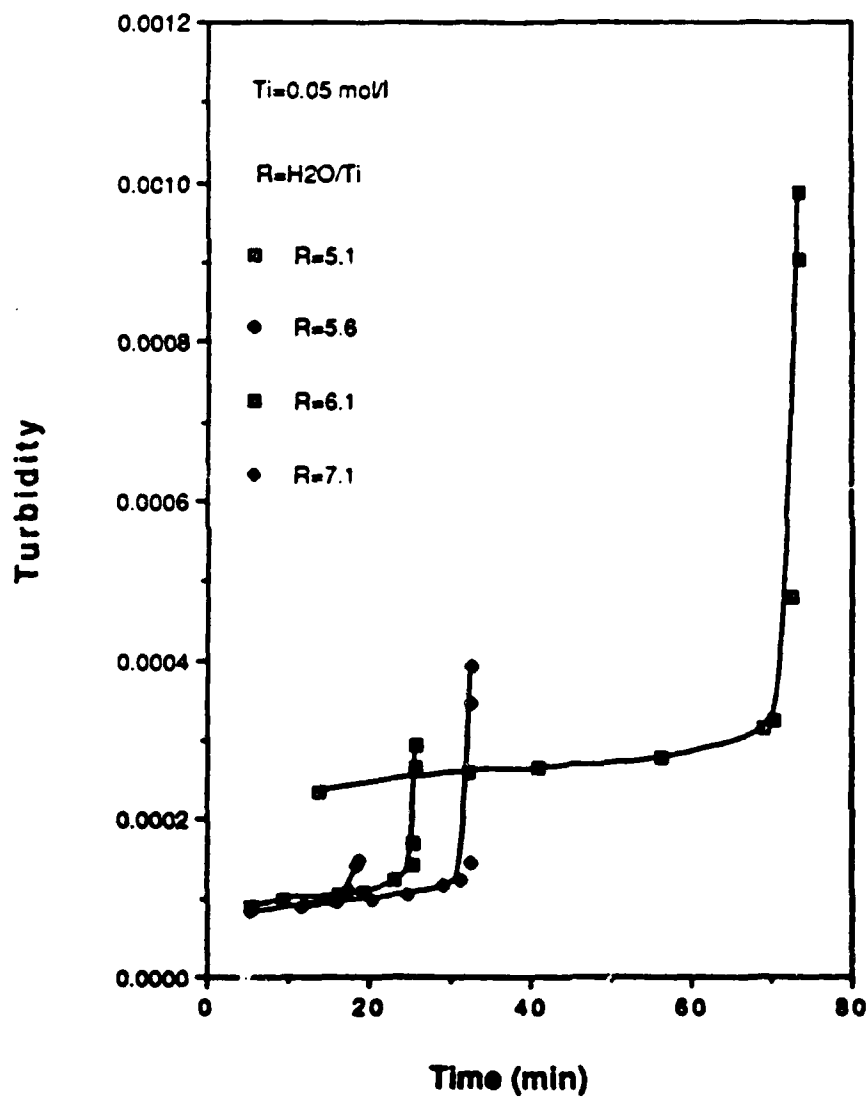


Figure 6: Influence of water content on stability of TIP solution.

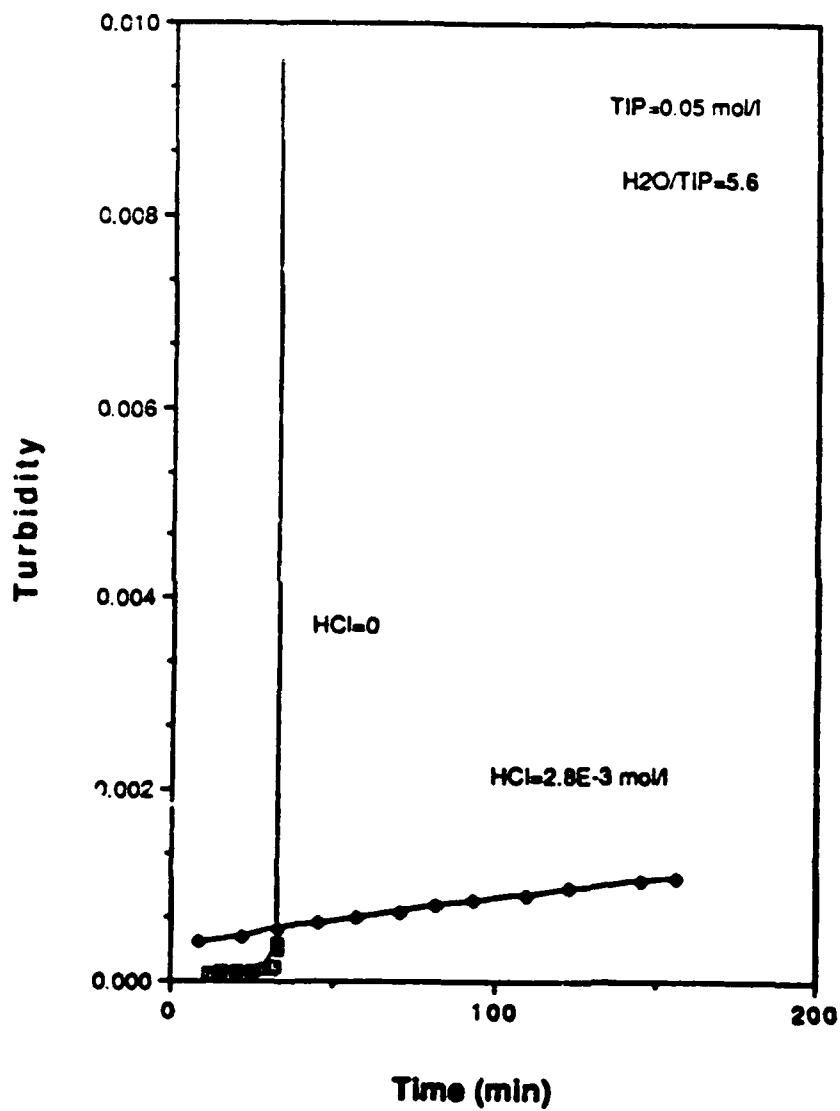


Figure 7: Influence of acid content on sol stability.

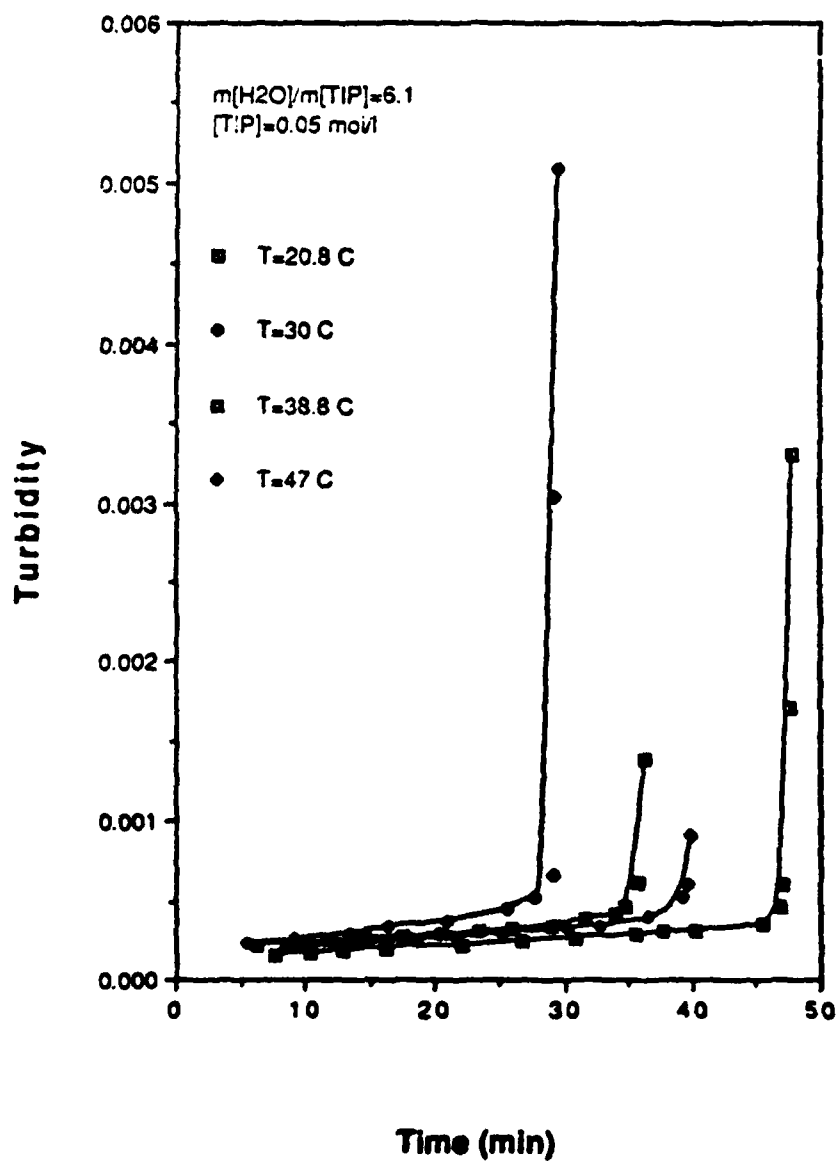


Figure 8: Influence of temperature on sol stability.

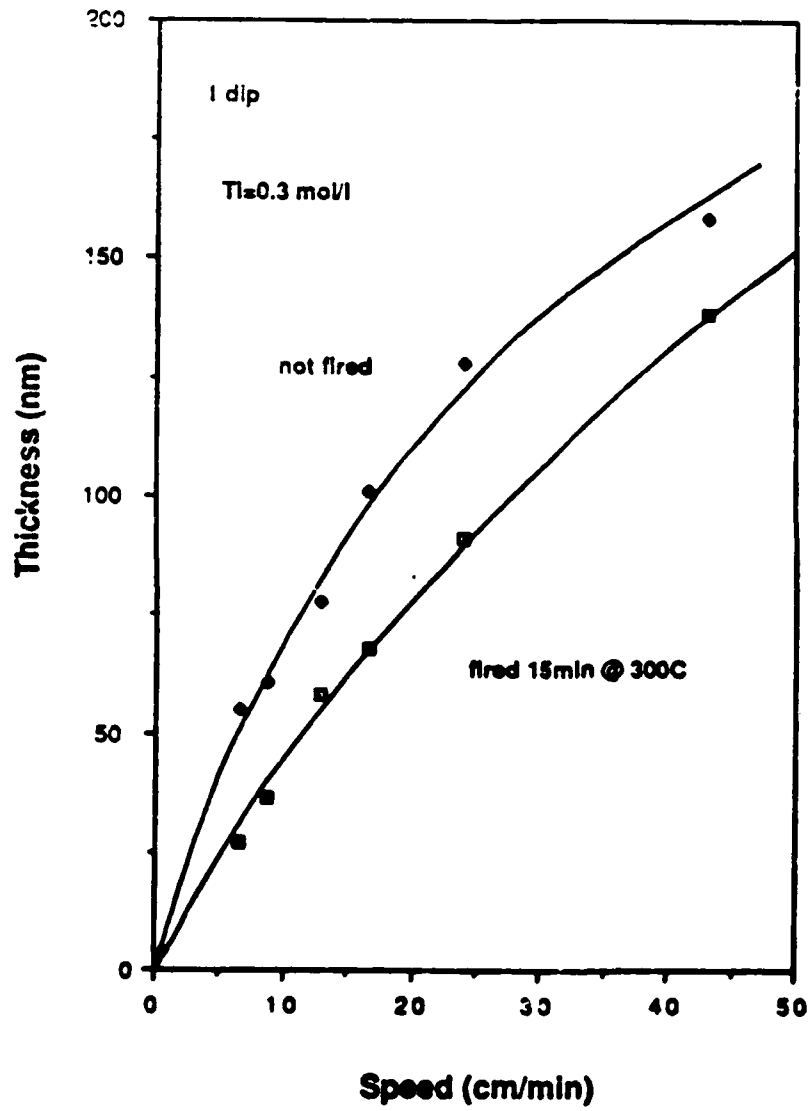


Figure 9: Influence of withdrawal speed on coating thickness.



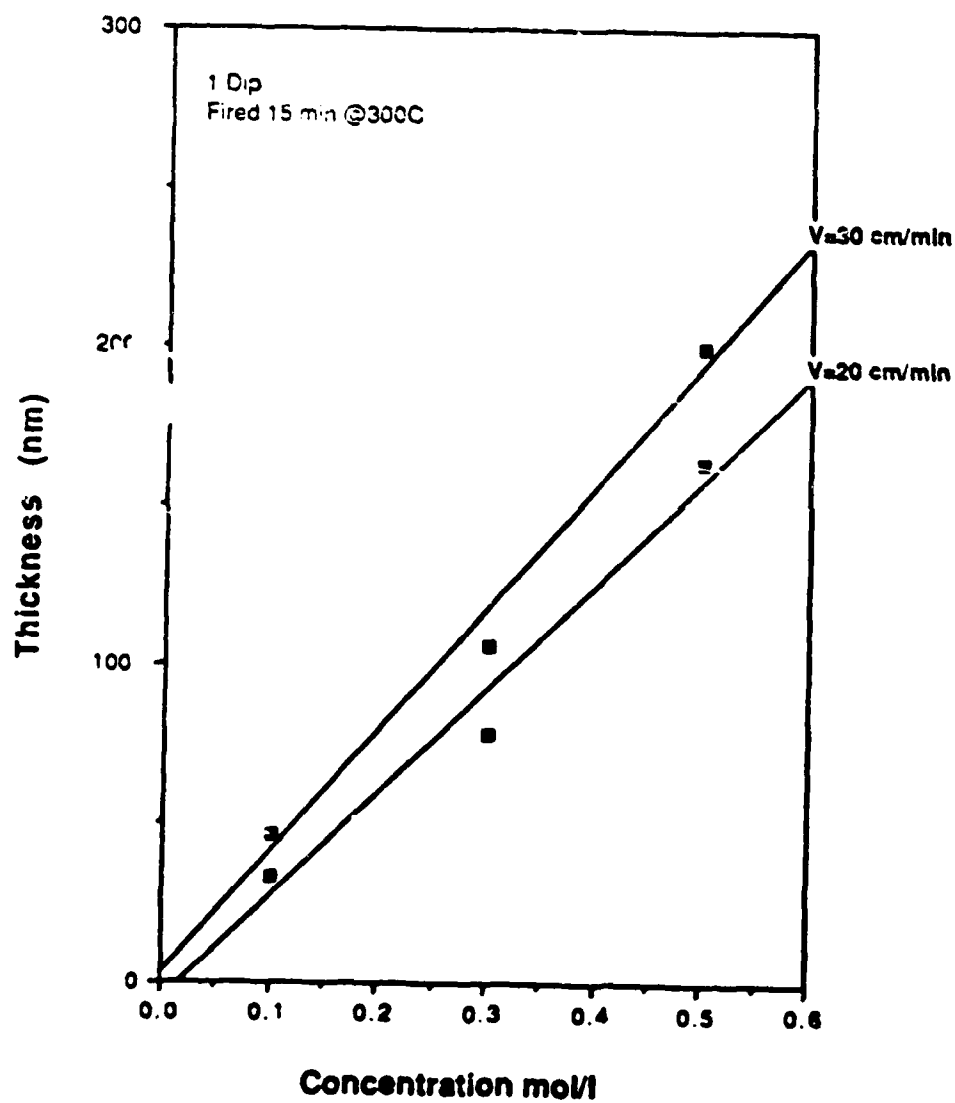


Figure 10: Influence of TIP molarity on coating thickness.

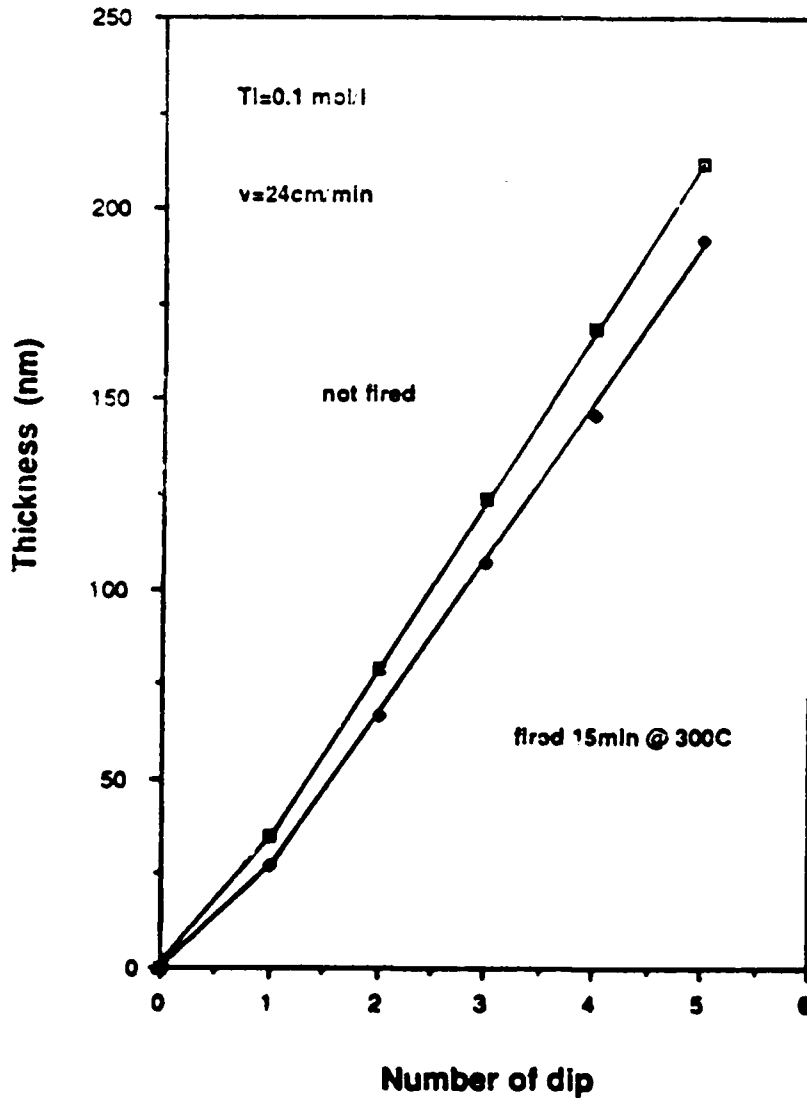


Figure 11: Influence of the number of dips on the coating thickness.

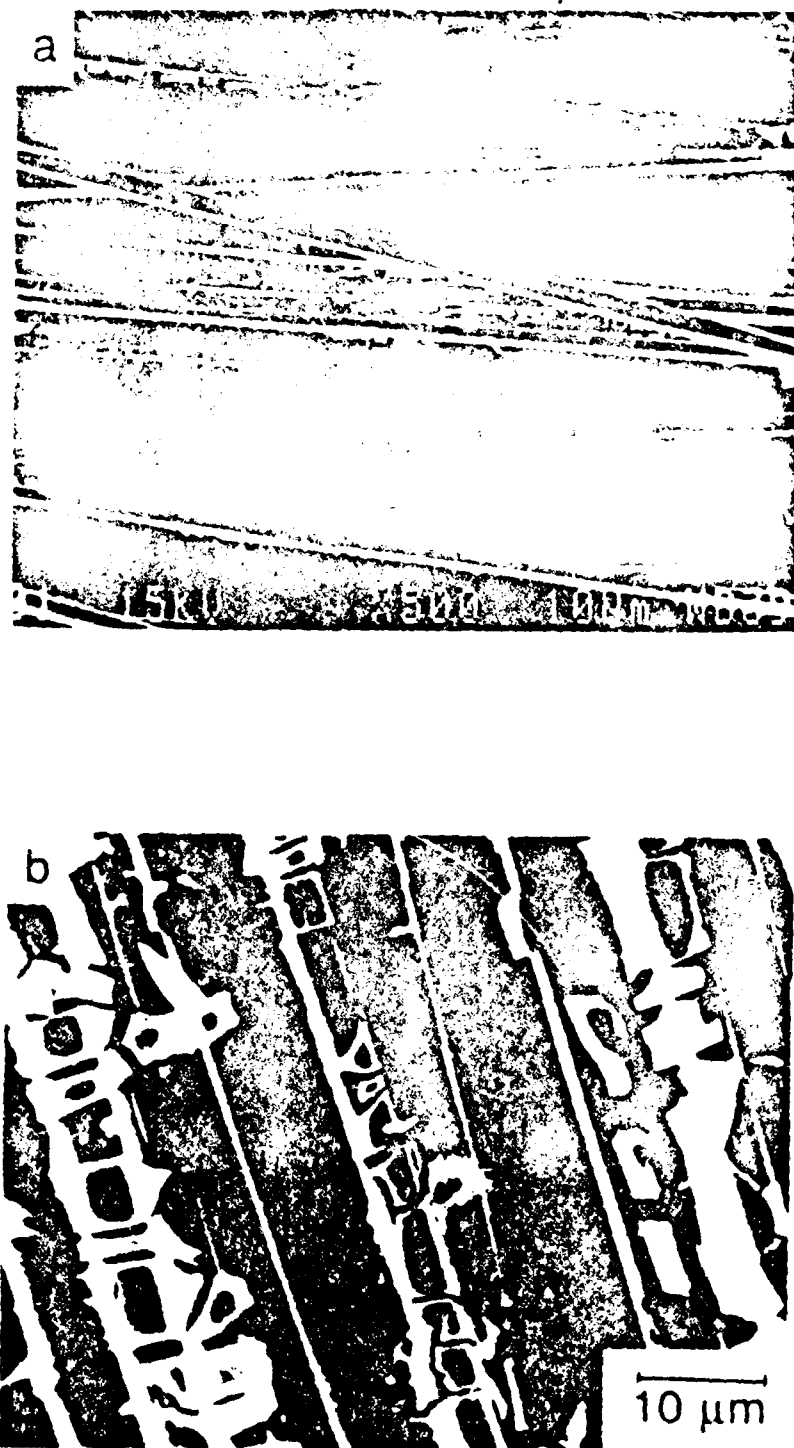


Figure 12 PAN 650/42 fibers dipped once in sol ( $[\text{TIP}] = 0.3 \text{ mol/L}$ ,  $[\text{DMSO}] = 0.1 \text{ mol/L}$ ) and (a) dried at  $60^\circ\text{C}$  or (b) fired at  $300^\circ\text{C}$ .



Figure 13. PAN 650/42 fibers dipped twice in sol ( $[TIP]=0.03\text{mol/l}$ ,  $V=24\text{cm/min}$ ) and dried at  $60^\circ\text{C}$ .

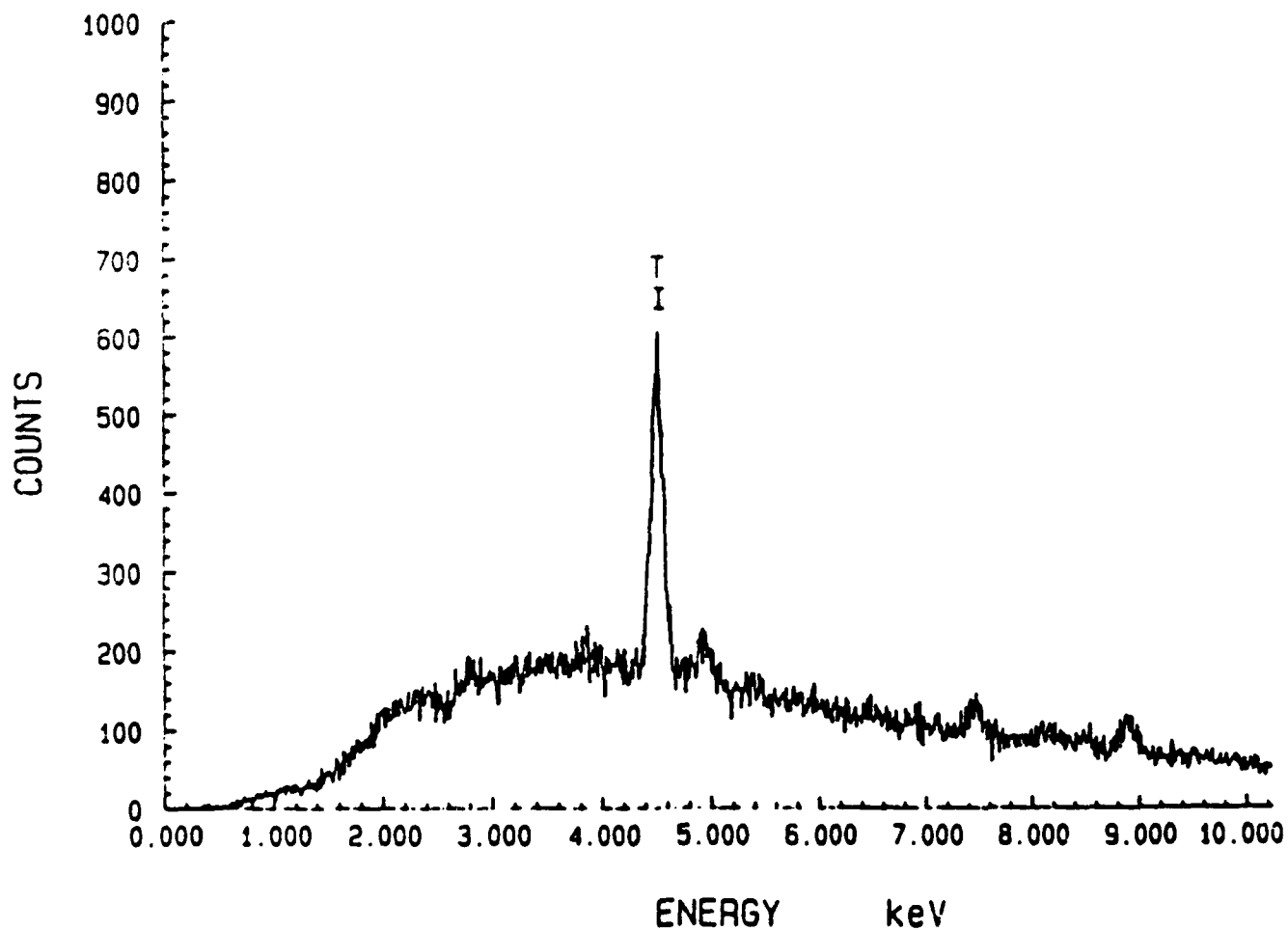


Figure 14: EDAX analysis of pitch 100S dipped twice in sol ([TIP]=0.03mol/l, V=24cm/min) and fired at 700 C.



Figure 15: Optical micrographs of pressure-infiltrated (a) uncoated and (b) coated carbon fibers.



ELEVATED TEMPERATURE PLASTIC FLOW AND FRACTURE  
OF MULTI-PHASE ALLOYS AND COMPOSITES

E. Wachtel, J. Wung and H. J. Rack

Materials Engineering Activity  
Department of Mechanical Engineering  
Clemson University  
Clemson, South Carolina 29634-0921



## INTRODUCTION

Ordered intermetallic compounds, for example, TiAl, Ti<sub>3</sub>Al, NiAl, Ni<sub>3</sub>Al, offer great potential for elevated temperature application as either monolithic alloys or as matrix materials for fiber reinforced metal matrix composites. To date their application has, however, been limited by their rather low room and elevated temperature ductility and fracture toughness. Blenkinsop<sup>1</sup> has reported that it may be possible to enhance both the low and high temperature ductility of intermetallic compounds through the introduction of a controlled amount of a dispersed softer phase,  $\beta$  phase for the specific example of Ti<sub>3</sub>Al. In addition, numerous studies of ceramic materials have shown that it is possible to enhance the fracture toughness of brittle materials through the introduction of a second brittle phase, for example, SiC whiskers in Al<sub>2</sub>O<sub>3</sub>, where, in this instance, the brittle second phase serves to locally deflect propagating cracks<sup>2,3</sup>. In both illustrations, it is clear that the effectiveness of these toughening mechanisms will be critically dependent on achieving a uniform dispersion of the second phase. Attainment of this uniform dispersion in candidate intermetallic systems will require that we develop a detailed understanding of the elevated temperature high strain deformation behavior of these multi-phase materials. This investigation is aimed at achieving this fundamental understanding, utilizing selected titanium aluminide alloys as experimental model materials.

## EXPERIMENTAL APPROACH AND RESULTS

Table 1 lists the alloys being utilized in the present investigation. The alloys may be broadly divided into two types, Group 1 based on a  $\alpha_2$ -Ti<sub>3</sub>Al, DO<sub>19</sub> ordered HCP, matrix and Group 2 based on a  $\gamma$ -TiAl, L1<sub>0</sub>

TABLE 1  
ALLOY CHEMICAL COMPOSITIONS

Alloy Designation	Element(Wt. Pct)							
	Al	Nb	V	Mo	Fe	C	O	N
11	14.25	21.3	-	-	0.05	0.18	0.09	0.012
12	14.6	20.0	3.3	2.1	0.08	0.03	0.08	-
13	20	-	5	-	-	-	-	-
14	20	-	12	-	-	-	-	-
15	27.5	-	5	-	-	-	-	-
21	30	-	5	-	-	-	-	-
22	30	-	9	-	-	-	-	-
23	30	-	20	-	-	-	-	-

ordered FCT, matrix. Selection of Ti-24 Al-11 Nb, alloy 11, and Ti-25 Al-10 Nb-3 V-1 Mo, alloy 12, was based on their ready availability in ingot form and importance as commercial or near-commercial materials. Figure 1 shows representative optical micrographs of these alloys as produced in 7500 lb. ingots. The microstructure of alloy 11 consists of blocky  $\alpha_2$  with a background of extremely fine  $\alpha_2$  and  $\beta$ , while alloy 12 contains a transformed  $\alpha_2$  and  $\beta$  microstructure.

The selection of the Ti-V-Al ternary alloys was based on a consideration of the Ti-Al-V ternary phase diagram as recently presented by Nashimoto et al.<sup>3</sup>, Figure 2. Six alloys are currently being prepared as 15 kgm ingots and were chosen to contain the following combinations of phases:  $\alpha_2$ ,  $\alpha_2 + \beta$ ,  $\alpha_2 + \gamma$ ,  $\alpha_2 + \beta + \gamma$ ,  $\gamma + \alpha_2$  and  $\gamma + \beta$ . Following receipt of these alloys samples

will be provided to J. Howe at Carnegie-Mellon for inclusion in his studies of interfacial structures.

Initially, elevated temperature phase equilibria studies are being undertaken, utilizing differential scanning calorimetry (DSC) and elevated temperature x-ray diffraction (ETX), the latter being conducted in cooperation with the High Temperature Materials Laboratory at the Oak Ridge National Laboratory. Preliminary results of the DSC studies for alloys 11 and 12 are shown in Figure 3. This data indicates that the  $\alpha_2 + \beta \rightarrow \beta$  transformation temperature for these alloys is 1020°C and 1010°C, respectively. The former value of the  $\beta$  transus is in excellent agreement with the pseudo Ti<sub>3</sub>Al-Nb binary diagram shown in Figure 4, while the decrease in  $\beta$  transus noted for alloy 12 is in keeping with the known effects of the additional  $\beta$  stabilizing elements present in this alloy. Detailed analysis of the other transformations suggested by the DSC results is underway utilizing high temperature X-ray diffraction.

Compression samples, having a height to diameter ratio of 2.5 to 1, of alloy 11 and 12 are currently being machined. These specimens will be utilized to establish the influence of strain rate and temperature on the flow properties, employing constant true strain rate compression procedures<sup>6</sup>. It should be noted that the diameter of the test specimen has been selected to ensure polycrystalline deformation, that is the specimen diameter will, at a minimum, be ten times the grain size.

Tests will be run on the closed-loop microcomputer controlled servo-hydraulic MTS machine described in the First Annual Report, with the test sample being rapidly cooled after testing using an integral gas quench attachment to preserve the deformed structure.

## REFERENCES

1. P. A. Blankensop, "Development in High Temperature Alloys," Proc. 5th Int. Con. Titanium, G. Lutjering, V. Zwicker, and W. Bunk, eds., Munich, 1984, Vol. 4, p. 2323.
2. K. T. Faber and A. G. Evans, "Crack Deflection Process - I. Theory," Acta Metall., Vol. 31, 1983, pp. 565-576.
3. K. T. Faber and A. G. Evans, "Crack Deflection Process - II. Experiment," Acta Metall., Vol. 31, 1983, pp. 577-584.
4. K. Hashimoto, H. Doi, and T. Tsujimoto, "Reexamination of the Ti-Al-V Ternary Phase Diagram," Trans. Japan Inst. of Metals, Vol. 27, 1986, p. 741.
5. R. Strychor, J. C. Williams, and W. A. Soffa, "Phase Transformations and Modulated Microstructures in Ti-Al-Nb Alloys," Met. Trans., Vol. 19A, 1988, p. 225.
6. P. L. Carpenter, B. C. Stone, S. C. Ernst, and J. F. Thomas, "Characterization and Modeling of the High Temperature Flow Behaviour of Aluminium Alloy 2024," Met. Trans. A, Vol. 17A, Dec. 1986, pp. 2227-2337.

a



b

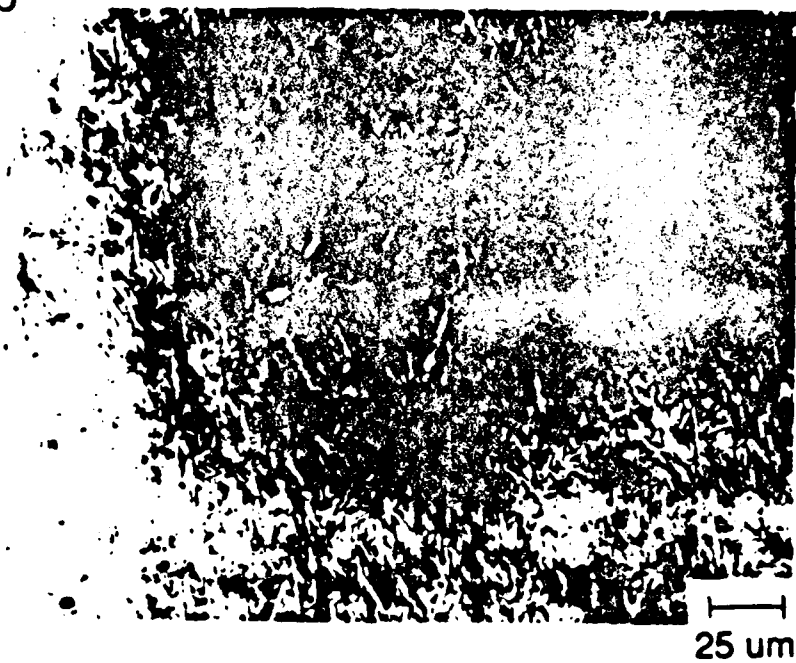


Figure 1 - Optical Micrographs of (a) Alloy 11 and (b) Alloy 12.

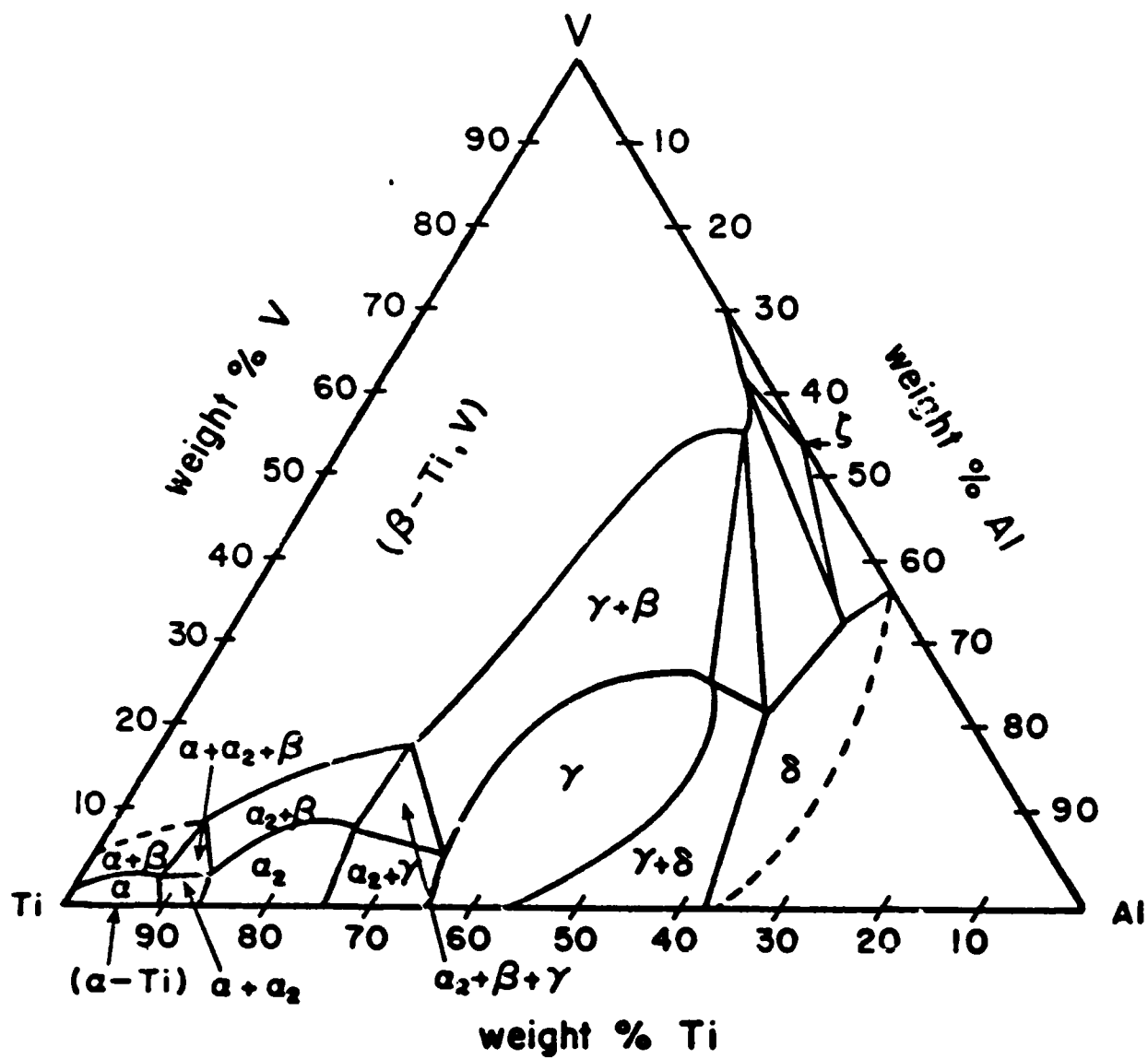
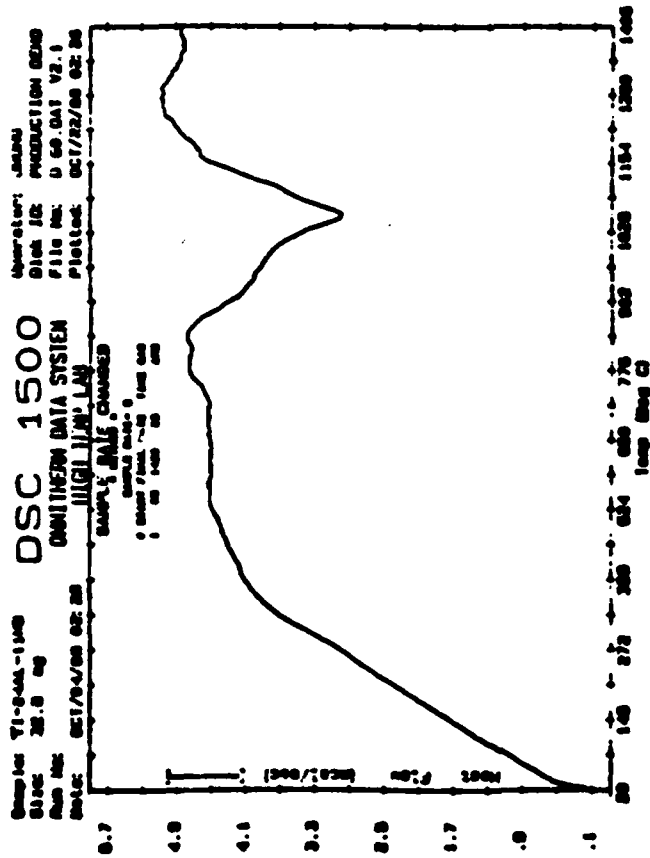


Figure 2 - Isothermal Section of Ti-Al-V Ternary Phase Diagram<sup>4</sup>.

a



b

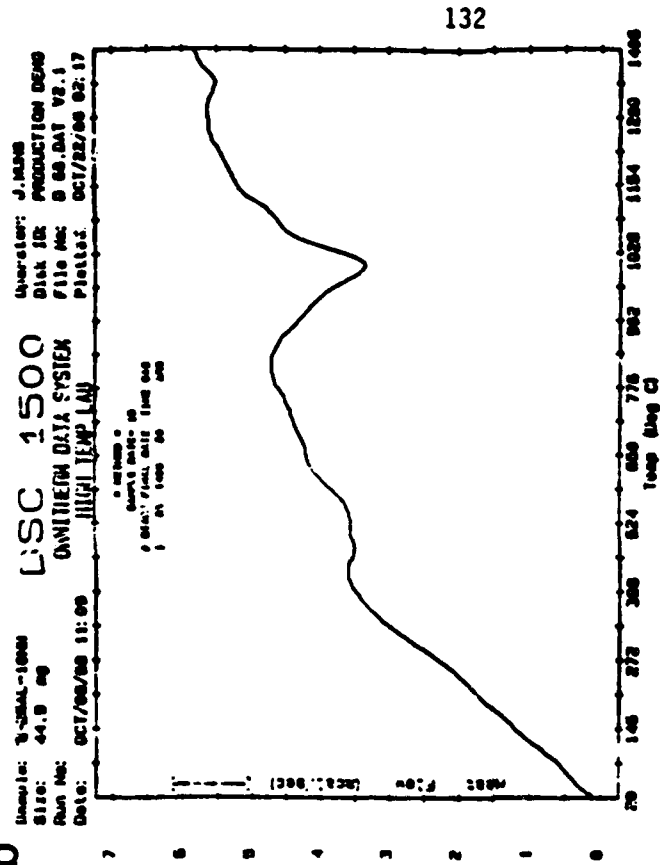


Figure 3 - Differential Scanning Calorimetry for (a) Alloy 11 and (b) Alloy 12.

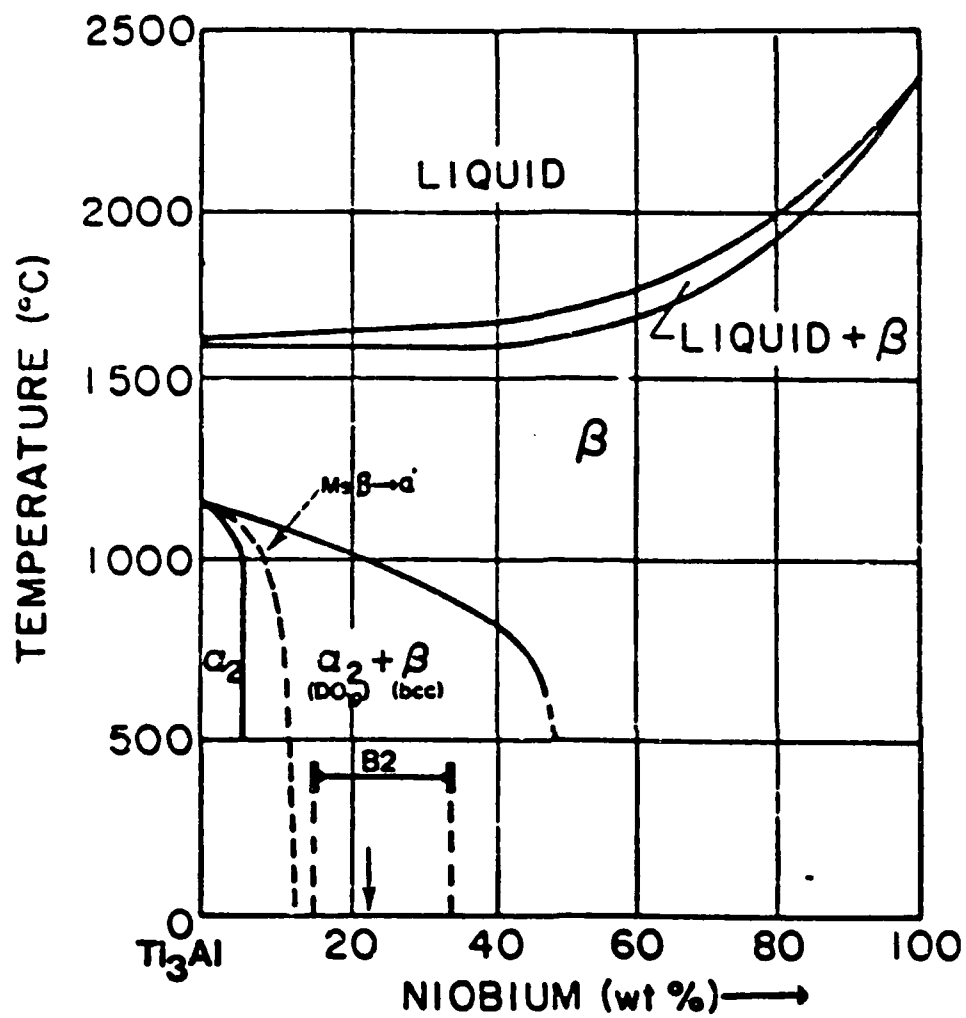


Figure 4 - Pseudo-Binary Ti<sub>3</sub>Al-Nb Phase Diagram<sup>5</sup>.





Phase Stability and Aging Response of  
TiC Reinforced Inconel 718

E. F. Wachtel

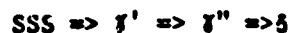
H. J. Rack

Materials Engineering Activity  
Department of Mechanical Engineering  
Clemson University  
Clemson, South Carolina

## INTRODUCTION

Metal matrix composites (MMC's) are being developed to improve specific stiffness, specific strength and high temperature performance. Theoretically MMC's are intended to combine the high toughness and ductility of a metal matrix with the high strength and stiffness of the ceramic reinforcing phase. While most previous efforts have focused on Al and Mg matrix composites, recent advances in material technology have resulted in the development of an intermediate temperature MMC based on a matrix of Inconel 718.

Inconel 718 is a popular intermediate temperature (700°C) Ni-base superalloy for aerospace and turbine disc applications. The alloy is available in cast, wrought and powder metallurgy (P/M) forms, with the cast product having slightly higher Mo content. Precipitation reactions in this alloy, as depicted by the TTT diagram shown in Figure 1, have been studied extensively, with the aging sequence being,



The  $\gamma'$  phase is a disc shaped, coherent precipitate with an ordered FCC structure (L1<sub>2</sub>) having a stoichiometry based on the Ni<sub>3</sub>Al composition, with titanium freely substituting for aluminum.  $\gamma''$  is a metastable, lens shaped, coherent precipitate with an ordered body centered tetragonal crystal structure (DO<sub>22</sub>) having a stoichiometry based on Ni<sub>3</sub>Nb. Titanium and possibly aluminum can substitute for the niobium.  $\delta$  is a stable, incoherent precipitate with an orthorhombic structure (DO<sub>19</sub>), having a stoichiometry based on Ni<sub>3</sub>Nb.

It is generally agreed that the major strengthening phase in Inconel 718 is gamma double prime ( $\gamma''$ )<sup>1-9</sup>. This is anomalous to other nickel based superalloys containing aluminum and titanium which are strengthened by a gamma prime ( $\gamma'$ ) precipitate reaction<sup>10-12</sup>. While  $\gamma'$  is detected in Inconel

718, it is not considered to be the strengthening phase<sup>6-9</sup>. Overaging of Inconel 718 results from coarsening of the  $\gamma''$  precipitates and precipitation of the delta phase. Studies of P/M alloys have shown that the precipitation reactions are similar to those of the cast and wrought products<sup>13-14</sup>.

Various carbides may also be present in the Inconel 718 system. These include: an MC type (usually titanium or niobium carbide or carbo-nitride) which has a random cubic morphology (titanium and niobium carbides are mutually soluble in one another), a  $M_6C$  type, which is derived from the decomposition of MC and which typically has a blocky, grain boundary morphology, a  $M_7C_3$  type which has a blocky intergranular morphology and a  $M_{23}C_6$  type which forms from the decomposition of either MC or  $M_7C_3$  and has a grain boundary platelet morphology. In addition to  $\gamma''$  strengthening, various investigators have suggested that niobium carbide (NbC) precipitation may also enhance the properties of Inconel 718<sup>1,2,5,7,8,9,15</sup>. Carbide type, distribution and morphology have been shown to affect properties, particularly ductility and stress rupture<sup>15</sup>. Finally, the stability of carbides and the solubility of carbon in Inconel 718 have been studied, with the solubility of carbon increasing substantially at temperatures greater than 980°C<sup>15</sup>.

Previous experience with aluminum and magnesium matrix composites has shown that precipitation reactions may be altered by the presence of a ceramic reinforcement<sup>16-19</sup>. This phenomenon is particularly pronounced in systems where the precipitation reactions exhibit heterogeneous nucleation. Enhanced heterogeneous nucleation and growth of precipitates in this instance is associated with a dislocation network, the network having developed in response to the thermal strain associated with the mismatch in coefficient of thermal expansion between the matrix and reinforcement. Indeed, dislocation

densities on the order of  $10^{13}/\text{cm}^2$  have been reported at the matrix-reinforcement interface<sup>20</sup>.

It is well established that the  $\gamma'$  phase nucleates heterogeneously in Inconel 718, typically at extrinsic stacking faults or at intrinsic slip dislocation<sup>4,21,22</sup>.  $\gamma''$  nucleation is intimately associated with existing  $\gamma'$  precipitates<sup>7</sup>. In addition, niobium carbide is reported to nucleate heterogeneously<sup>1,2,7,23</sup>. Based on the above considerations, it would be anticipated that the aging kinetics of Inconel 718 should be affected by the addition of a ceramic reinforcing phase.

The primary objective of this study is to determine the effect the addition of a reinforcing phase addition has on the precipitation reactions and aging kinetics of an Inconel 718 matrix composite. A second objective is to examine the stability of TiC as a reinforcing phase in this Ni base superalloy.

#### EXPERIMENTAL PROCEDURES

The materials used in this study were: a P/M composite of Inconel 718 nominally reinforced with 20 volume percent TiC, P/M 718 and cast 718. Compositions of the ingot and powder alloys are given in Table I. P/M and

Table I. Chemical Composition of Ingot and Powder

Element	Ni	Fe	Cr	Mo	Ti	Al	Nb	Mn	Si
Powder	52.8	18.3	18.4	3.1	1.0	0.6	5.3	0.1	0.2
Ingot	52.5	18.7	18.3	3.1	1.0	0.6	5.4	0.1	0.1

composite billet fabrication involved wet blending of -200 mesh, gas atomized powder with TiC particulate, drying and canning/evacuated in a mild steel

can. Scanning electron micrographs and L&N Microtrac powder size distributions for the Inconel 718 and TiC materials are shown in Figures 2 and 3, respectively. Compaction of the P/M and composite materials was achieved by hot isostatic pressing at 1150°C for three hours at a pressure of 103 MPa, as depicted in Figure 4. Following compaction the billets were extruded at 1040°C with an extrusion ratio of 19:1. Finally, in order to maintain consistent thermomechanical processing history, the cast material was subjected to the same hiping and extrusion treatment.

The microstructure of the P/M and cast materials was initially examined utilizing standard metallographic procedures. In addition, the composite material's microstructure was extensively examined using a JEOL JSM IC848 scanning electron microscope in the backscatter mode. Semi-quantitative analysis of the various phases present in the backscatter micrographs was done using x-ray energy dispersive spectroscopy (EDS), the system being calibrated using a copper standard. A spot mode was utilized to analyze the composition of the various phases observed in the TiC reinforced Inconel 718, with a beam spot diameter of 0.02  $\mu\text{m}$ .

Differential scanning calorimetry and  $R_c$  hardness measurements were used to compare the precipitation reactions of the composite and the unreinforced materials. The aging kinetics were examined by monitoring the hardness of 0.5 in. x 0.5 in. x 0.5 in. solution treated and quenched samples as a function of isothermal aging time, from 0.5 to 1000 hours over aging temperatures varying from 650°C to 870°C. The reported  $R_c$  values are the average of three measurements made at each time-temperature combination.

Thin foil transmission electron microscopy studies are currently underway to determine the location and nature of the precipitate reactions and the type and extent of the matrix/reinforcing phase interfacial reaction.

---

Precipitates and reaction products are being analyzed using selected area electron diffraction (SAED) and energy dispersive x-ray spectroscopy (EDS). Five time - temperature combinations are being analyzed for the composite material as follows: 1. Super-saturated solid solution, as-quenched, 2. Underaged, 650°C for 1 hour, 3. Peak aged, 760°C for 3 hours, 4. Age softened, 870°C for 30 hours, and 5. Overaged, 870°C for 300 hours.

In addition, elevated temperature tensile and stress rupture testing is being performed in cooperation with DWA Composite Specialties, with selected failed specimens being examined using SEM fractography techniques.

### RESULTS

Figure 5 shows a typical SEM backscatter electron micrograph of the 1150°C solution treated composite. Three distinct phases are obvious in this micrograph: light, grayish and black. A spectrum for the black phase, identified as TiC, is shown in Figure 6. In general, TiC was randomly distributed throughout the matrix with the volume fraction and the size being lower than anticipated. Indeed, the average volume fraction of TiC, as measured in the composite, was approximately five volume percent, with the average particulate size ranging from 5 to 10  $\mu\text{m}$ . The spectrum for the gray phase, a mixed carbide of Ti and Nb, probably a mixed MC type carbide, is shown in Figure 7. This result is reasonable since both carbides have the same structure (simple cubic) and are completely soluble in one another occupying various sites on a carbon sublattice. Finally, the spectrum for the light, Inconel 718 matrix, is shown in Figure 8.

Preliminary differential scanning calorimetry observations are shown in Figure 9. While P/M 718 exhibits a single relatively sharp peak at 810°C, with indication of other peaks at 375°, 600° and 900°C, the DSC trace for the

TiC reinforced composite suggest the presence of peaks at 375°, 550°, and 1000°C. Further experiments aimed at more precise determination of the reaction temperatures and the enthalpies of reaction are currently underway.

The results of the aging studies are shown in Figure 10. It is apparent that the aging kinetics of the cast, P/M and composite materials are a distinct function of aging temperature. Aging at 650°C results in a gradual increase in  $R_c$  hardness in both the cast and P/M Inconel 718, with peak hardness occurring after aging for 256 hrs. In contrast, aging of the TiC reinforced composite is accelerated, with almost all aging response occurring within the first hour, little increase in hardness being observed thereafter. Further, little difference in aging response is noted after aging at 705°C, overaging of all materials being observed at times greater than 4 hrs.

Increasing the aging temperature to 760°C once again allows separation of the unreinforced and reinforced Inconel 718. At this aging temperature, overaging, that is a decrease in hardness, is delayed by the introduction of the reinforcement, overaging being observed for aging time in excess of 32 hrs for the unreinforced materials, while overaging is only observed in the reinforced alloy for aging times greater than 100 hrs.

Aging at 815°C results in overaging of all materials at times greater than 0.5 hrs., with some evidence for a second aging peak being observed in the composite material. Indeed, this secondary aging peak is more pronounced in the composite material aged at 870°C, while only a slight degree of age hardening is observed in the unreinforced alloys.

A comparison of the elevated temperature tensile properties of unreinforced and reinforced Inconel 718 are shown in Figures 11 and 12. The former results indicate that there appears to be little improvement in the high temperature strength of Inconel 718 occasioned by the introduction of



the TiC reinforcement. However, there is, independent of temperature, a severe reduction of the tensile ductility associated with TiC reinforcement. The failure mechanism of the unreinforced material is ductile rupture as seen in Figure 13. Similarly in the composite material, the matrix material exhibits some ductility as evidenced by localized dimpling while the reinforcement fails by brittle cleavage as seen in Figure 14. Fractographic evidence suggests that at least part of this reduction in tensile ductility is directly related to TiC clumping, Figure 15.

Preliminary stress rupture properties of unreinforced and reinforced Inconel 718 are shown in Figure 16. Once again, at least at the single stress level and temperature examined to date, there appears to be no benefit associated with TiC reinforcement of Inconel 718. Further creep and stress rupture measurement are currently underway to substantiate these results over a wider range of temperature and stress level.

#### DISCUSSION

It is hypothesized that the differences in aging response noted between unreinforced and TiC reinforced Inconel 718 can be explained by considering the thermal stability and redissolution of TiC during the P/M processing sequence utilized in fabricating the composites currently under investigation.

During elevated temperature compaction, extrusion and solution treatment, TiC will therefore partially dissolve, the extent of dissolution depending on exposure time and temperature. It is further hypothesized that on cooling Nb and Ti will combine at the Inconel/TiC interface forming mixed MC carbides, with the resulting matrix being enriched in Ti and depleted of Nb. Analytical transmission electron microscopy studies have confirmed

*Page 144 Blank (misnumbered)*

this hypothesis, precipitates of (Ti,Nb)C having been detected in the peak aged material, Figure 17. The compositions determined by analytical TEM confirm earlier SEM-EDS results but indicate that the actual Nb concentration of the mixed carbides may be as high as 40 atomic percent.

Furthermore increases in Ti content thru, in the present instance, dissolution of the TiC reinforcement, will accelerate the formation of  $\gamma'$  precipitates. In addition, increased matrix Ti content could promote the formation of the  $\epsilon$  phase ( $Ni_3Ti$ ) which, while not normally observed in Inconel 718, has been reported in other Ni-base superalloys having higher Ti contents. Detailed TEM studies are currently underway to verify these hypothesis.

In addition to a difference in the kinetics, the magnitude of the aging response appears to have been altered. The ratio of peak hardness to super saturated solid solution hardness may be used to assess the magnitude of the aging response. For the unreinforced material, this ratio is an order of magnitude higher than the reinforced material. Further, the ratio of the overaged hardness to the supersaturated solid solution hardness is an indication of the stability of the system. Again, an order of magnitude difference is seen between the unreinforced and the reinforced material. It is believed that this affect may be due, in part, to the effectively low concentration of Nb in the matrix, smaller coherency strains associated with  $\gamma''$  and a smaller volume fraction of the  $\delta$  phase.

In an attempt to assess the stability of the composite, samples were subjected to multiple solution treatment and aging sequences. The results of the reversibility experiments are shown in Figure 18. These results show that the aging behavior of the TiC reinforced material is dependent on the prior thermo-mechanical history of the material, one possible reason for this

may involve the reaction between the matrix and the TiC. A more comprehensive analysis of this phenomenon is planned using DSC.

#### CONCLUSIONS

To date the following conclusions may be drawn from this study of the aging behavior and stability of TiC reinforced Inconel 718.

1. The aging response (magnitude) and the aging kinetics (rate of reaction) of the composite material are substantially different than those of the unreinforced materials.
2. The matrix and reinforcement react to form a mixed MC carbide (Ti/Nb)C which alters the matrix chemistry.
3. The elevated temperature strengths of TiC reinforced Inconel 718 are at best equivalent to the unreinforced alloy, while the tensile ductilities are inferior.

## REFERENCES

1. H. L. Eiselstein, "Metallurgy of a Columbium-Hardened Nickel-Chromium-Iron Alloy," Advances in the Technology of Stainless Steels and Related Alloys, ASTM STP 369, Philadelphia, 1965, pp. 62-79.
2. M. Kaufman and A. E. Palty, "The Phase Structure of Inconel 718 and 702 Alloys," Trans. AIME, Vol. 221, 1961, pp. 1253-1261.
3. J. F. Barker, E. W. Ross, and J. F. Radavich, "Long Time Stability of Inconel 718," Jn. of Metals, Vol. 22, 1970, pp. 31-41.
4. R. S. Cremisio, J. F. Radavich, and H. M. Butler, "The Effect of Thermo-mechanical History on the Stability of Alloy 718," International Symposium on Structural Stability in Superalloys, Seven Springs, PA, 1968, pp. 597-618.
5. W. J. Boesch and H. B. Canada, "Precipitation Reactions and Stability of Ni<sub>3</sub>Cb in Inconel Alloy 718," International Symposium on Structural Stability in Superalloys, Seven Springs, PA, 1968, pp. 579-596.
6. D. F. Paulonis, J. M. Oblak, and D. S. Duvall, "Precipitation in Nickel-Base Alloy 718," Trans. ASM, Vol. 62, 1969, pp. 611-622.
7. R. Cozar and A. Pineau, "Morphology of Y' and Y" Precipitates and Thermal Stability of Inconel 718 Type Alloys," Met. Trans., Vol. 4, 1973, pp. 47-59.
8. J. W. Brooks and P. J. Bridges, "Long Term Stability of Inconel Alloy 718 for Turbine Disc Applications," High Temperature Alloys for Gas Turbines and Other Applications 1986, ed. W. Betz, et al., D. Reidel Publishing Co., Dordrecht, Holland, 1986, pp. 1431-1440.
9. J. F. Barker, D. D. Kruger, and D. R. Chang, "Thermo-mechanical Processing of Inconel 718 and Its Effects on Properties," Advanced High-Temperature Alloys: Processing and Properties, ed. S. Allen, R. M. Pelloux and R. Witmer, ASM, Metals Park, Ohio, 1986, pp. 125-137.
10. R. F. Decker, "Strengthening Mechanisms in Nickel-Base Superalloys," Steel Strengthening Mechanisms Symposium, Zurich, Switzerland, May 1969, 147-170.
11. E. A. Fell, "The Effect of Thermal Treatment on the Constitution of 80-20 Nickel-Chromium Alloys Hardened with Titanium and Aluminum," Metallurgia, Vol. 63, 1961, pp. 157-166.
12. J. M. Oblak, W. A. Owczarski, and B. H. Kear, "Heterogeneous Precipitation of Metastable  $\gamma'$ -Ni<sub>3</sub>Ti in a Nickel-Base Alloy," Acta Met., Vol. 19, 1971, pp. 355-363.
13. H. F. Merrick, "Effect of Heat Treatment on the Structure and Properties of Extruded P/M Alloy 718," Met. Trans., Vol. 7A, 1976, pp. 505-514.
14. K. Hajjarle, R. Angers, and G. Dufour, "Phase Analysis of Sintered and Heat Treated Alloy 718," Met. Trans., Vol. 13A, 1982, pp. 5-12.

15. E. L. Raymond, "Effect of Grain Boundary Denudation of Gamma Prime on Notch-Rupture Ductility of Inconel Nickel-Chromium Alloys X-750 and 718," Trans. AIME, Vol. 239, 1967, pp. 1415-1422.
16. H. J. Rack and J. W. Mullins, "Tensile and Notch Tensile Behavior of SiC<sub>w</sub> Reinforced 2124 Aluminum," High Strength Powder Metallurgy Aluminum Alloys II, ed. G. J. Hildeman and M. J. Koczak, The Metallurgical Society, Warrendale, PA., 1986, pp. 155-171.
17. H. J. Rack, "P/M Aluminum Metal Matrix Composites," Dispersion Strengthened Aluminum Alloys, ed. Y-W Kim, The Metallurgical Society, Warrendale, PA, 1988, in press.
18. H. J. Rack and R. W. Krenzer, "Thermomechanical Treatment of High Purity 6061 Aluminum," Met. Trans., Vol. 8A, 1977, pp. 335-346.
19. H. J. Rack, "The Influence of Prior Strain upon Precipitation in a High-Purity 6061 Aluminum Alloy," Mat'l's Sci. and Eng., Vol. 29, 1977, pp. 179-188.
20. M. Vogelsang, R. J. Arsenault, and R. M. Fisher, "An In Situ Study of Dislocation Generation at Al/SiC Interfaces in Metal Matrix Composites," Met. Trans., Vol. 17A, 1986, pp. 379-389.
21. A. A. Guimaraes and J. J. Jonas, "Recrystallization and Aging Effects Associated with the High Temperature Deformation of Waspaloy and Inconel 718," Met. Trans., Vol. 12A, 1981, pp. 1655-1666.
22. D. D. Krueger, S. D. Antolovich and R. H. Van Stone, "Effects of Grain Size the Precipitate Size on the Fatigue Crack Growth Behavior of Alloy 718 at 427°C," Met. Trans., Vol. 18A, 1987, pp. 1431-1449.
23. F. J. Rizzo and J. D. Buzzanell, "Effect of Chemistry Variations on the Structural Stability of Alloy 718," International Symposium on Structural Stability in Superalloys, Seven Springs, PA, 1968, pp. 501-543.
24. ASM Metals Handbook; 9th Edition, Volume 3, Properties and Selection: Stainless Steel, Tool Material and Special Purpose Materials, American Society for Metals, Metals Park, Ohio, 1980.
25. Aerospace Structural Metals Handbook, Metals and Ceramics Information Center Battelle Columbus Division.
26. E. Supan, DWA Composite Specialists, Unpublished Data.



Figure 1. TTT Diagram of Inconel 718<sup>10</sup>.

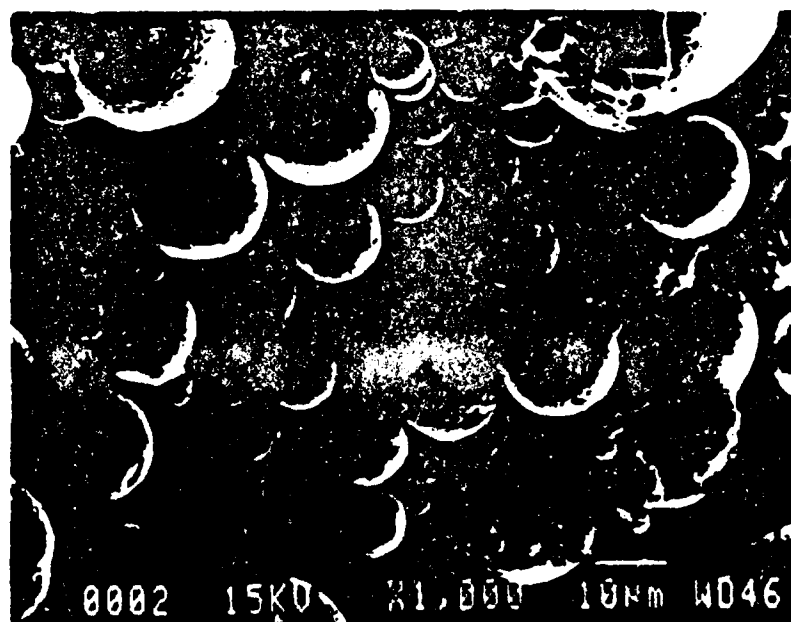
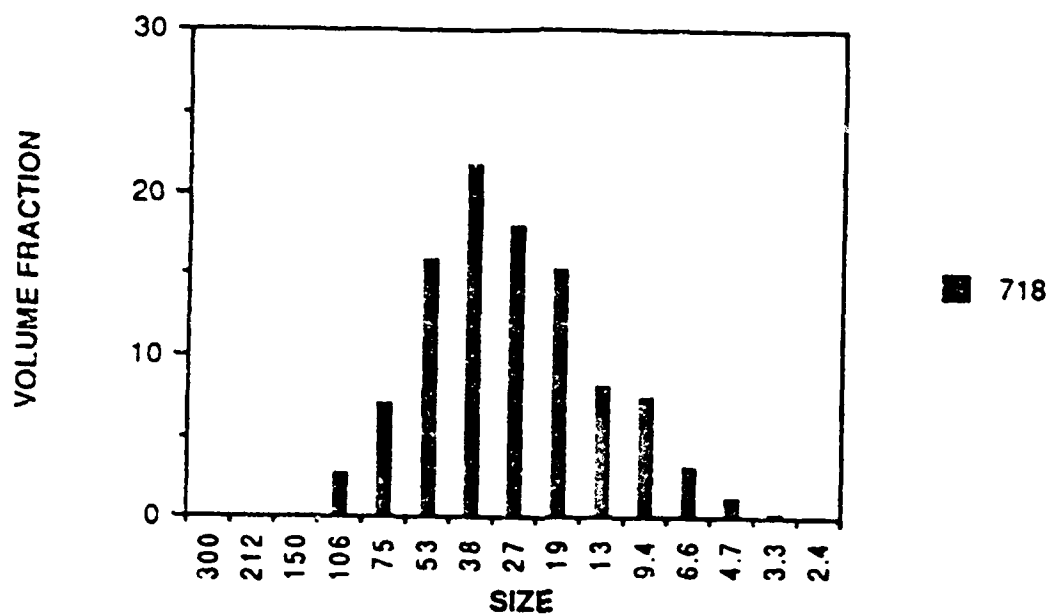


Figure 2. Scanning Electron Micrograph and L&N Microtrac Analysis of Inconel 718 Powder.



Figure 3. Scanning Electron Micrograph of Titanium carbide powder.



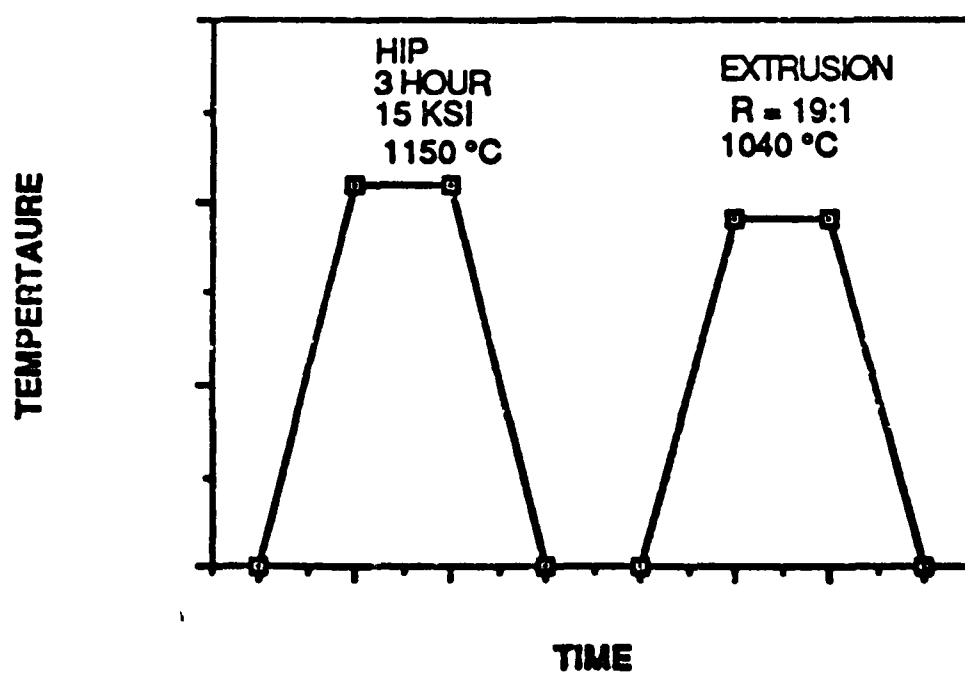


Figure 4. Thermo-mechanical Processing Schedule.



Figure 5. Backscatter Scanning Electron Micrograph of Inconel 718 Reinforced with 20 V/O TiC.

LT= 200 SECS

INCONEL 718 WITH 20 VOL % TIC SPOT MODE TIC

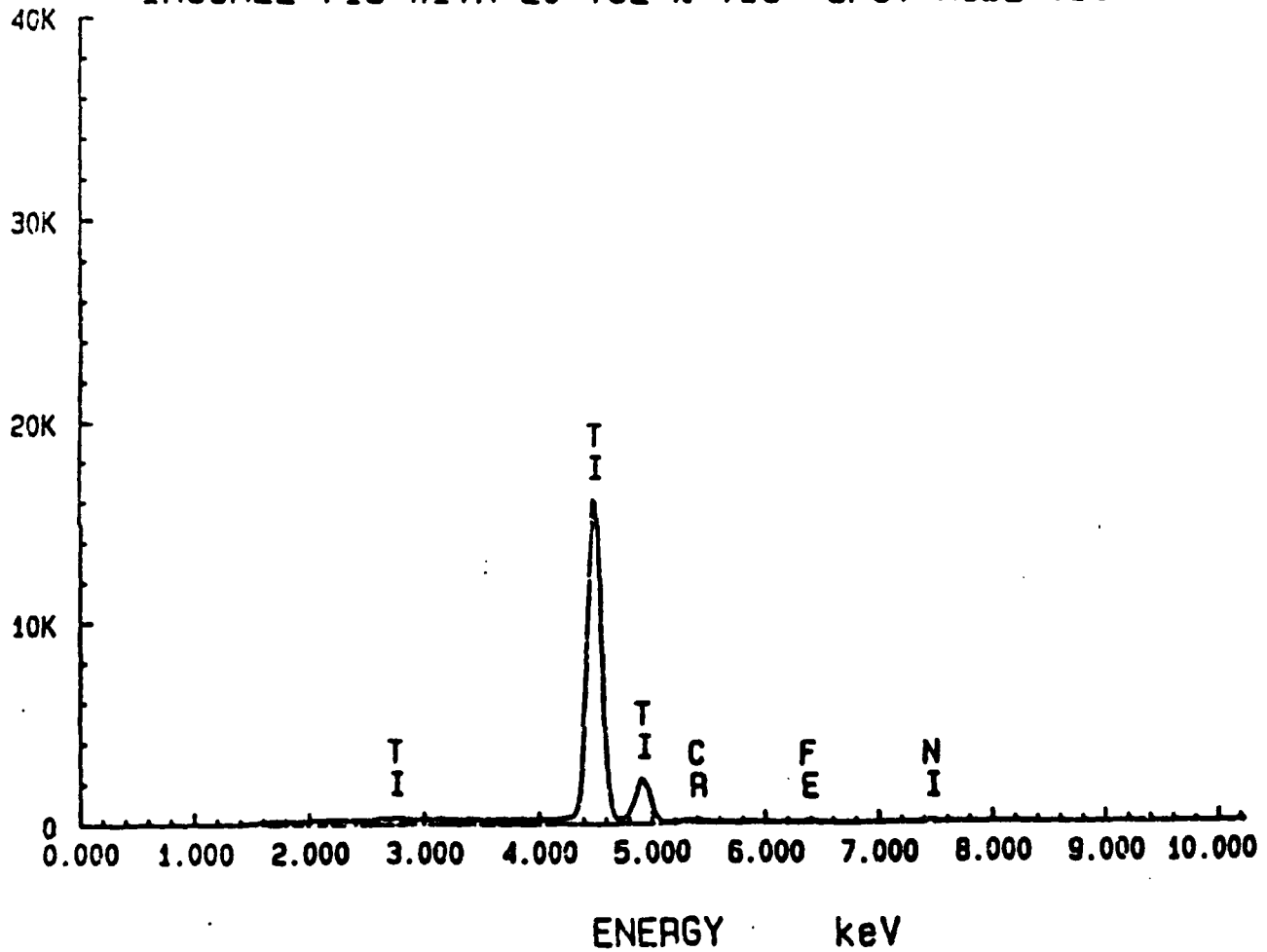


Figure 6. EDS spectrum of TiC Particulate.

LT= 200 SECS  
IN 718 + 20 VOL% TIC SPOT MODE OF PPT

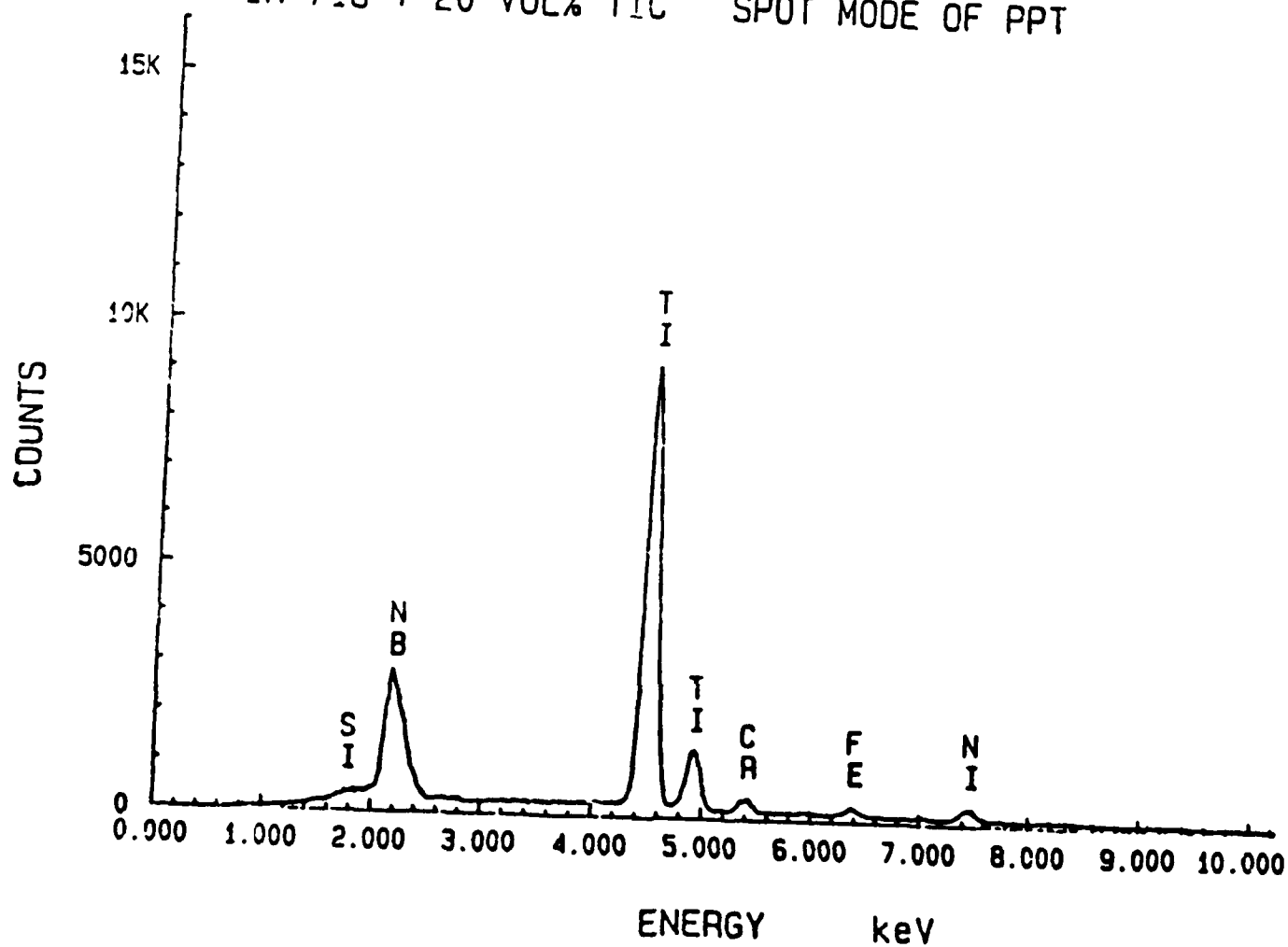


Figure 7. EDS Spectrum of MC Carbide.

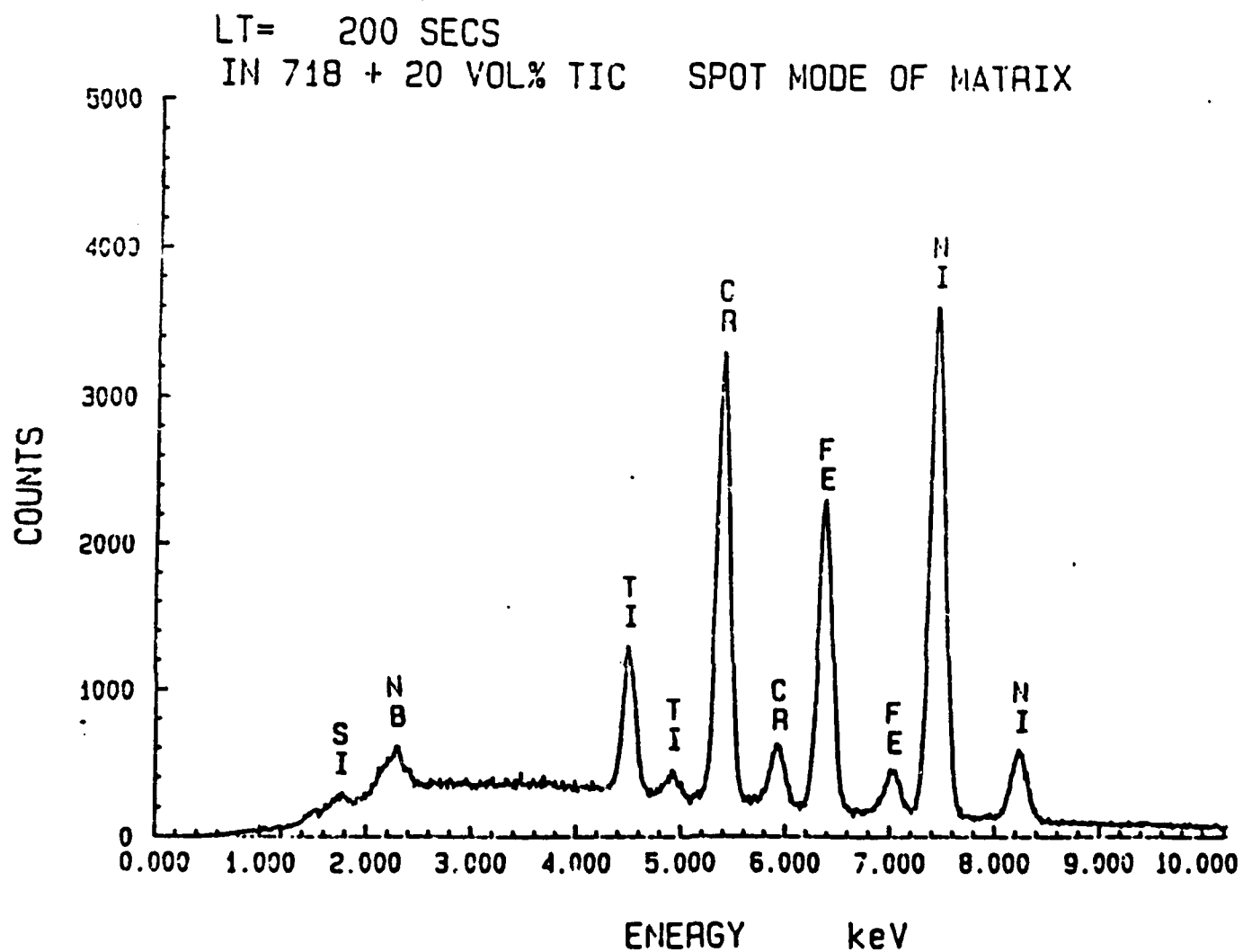


Figure 8. EDS Spectrum of Matrix Material.

Sample: INCOL 718/20TiC

Size: 58.3 mg

Run No:

Date: OCT/22/88 23:00

DSC 1500

OMNITHERM DATA SYSTEM

HIGH TEMP LAB

Operator: J. WUNG

Disk ID: PRODUCTION DEMO

File No: 3 58.DAT V2.1

Plotted: OCT/30/88 00:46

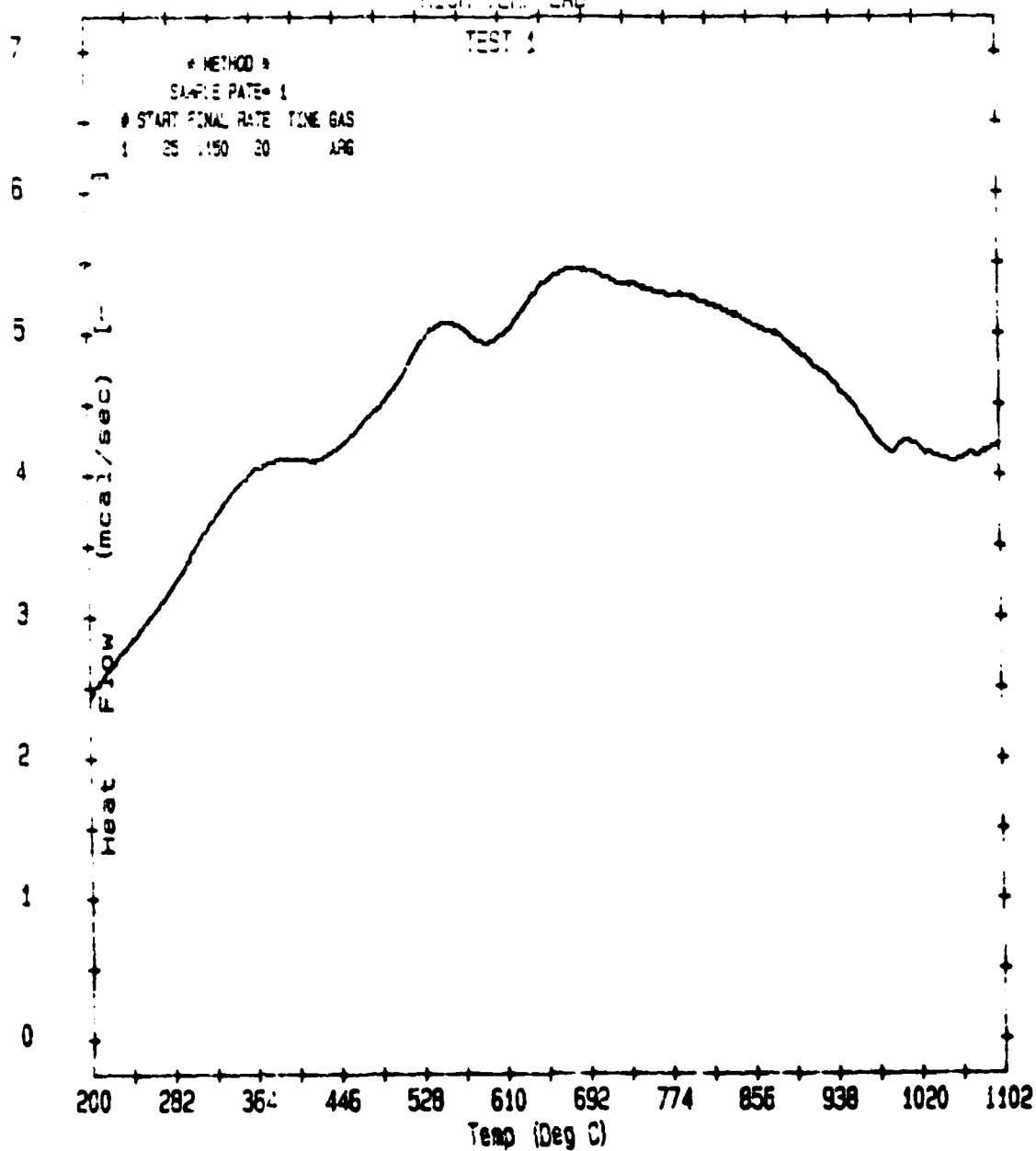


Figure 9. Differential Scanning Calorimetry of (a) Reinforced and (b) Unreinforced 718.

Sample: INCONEL 718

Size: 41.4 mg

Run No:

Date: OCT/03/88 13:36

DSC 1500

OMNITHERM DATA SYSTEM

HIGH TEMP LAB

Operator: J.WUNG

Disk ID: PRODUCTION DEMO

File No: D 59.DAT V2.1

Plotted: OCT/30/88 00:53

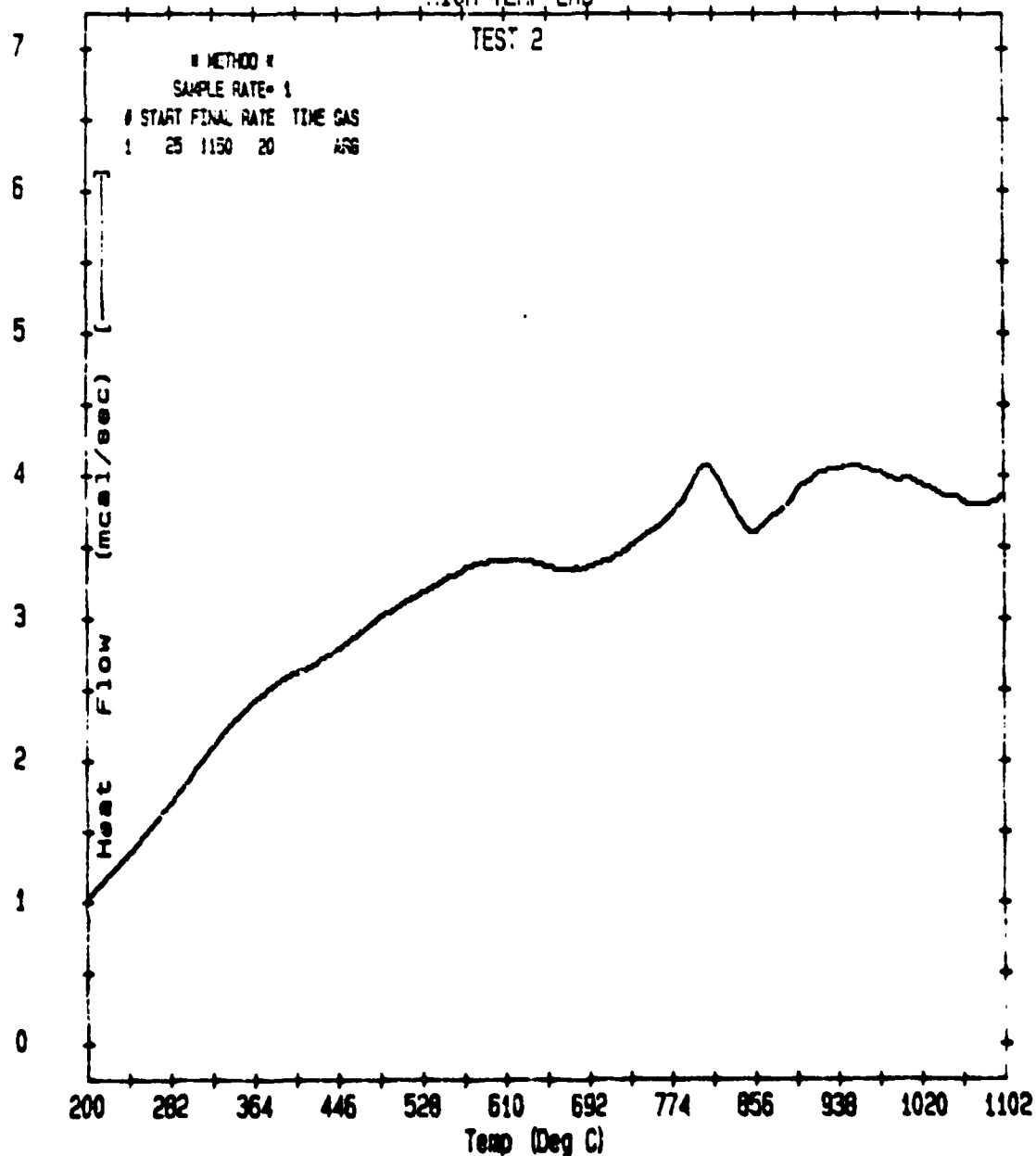
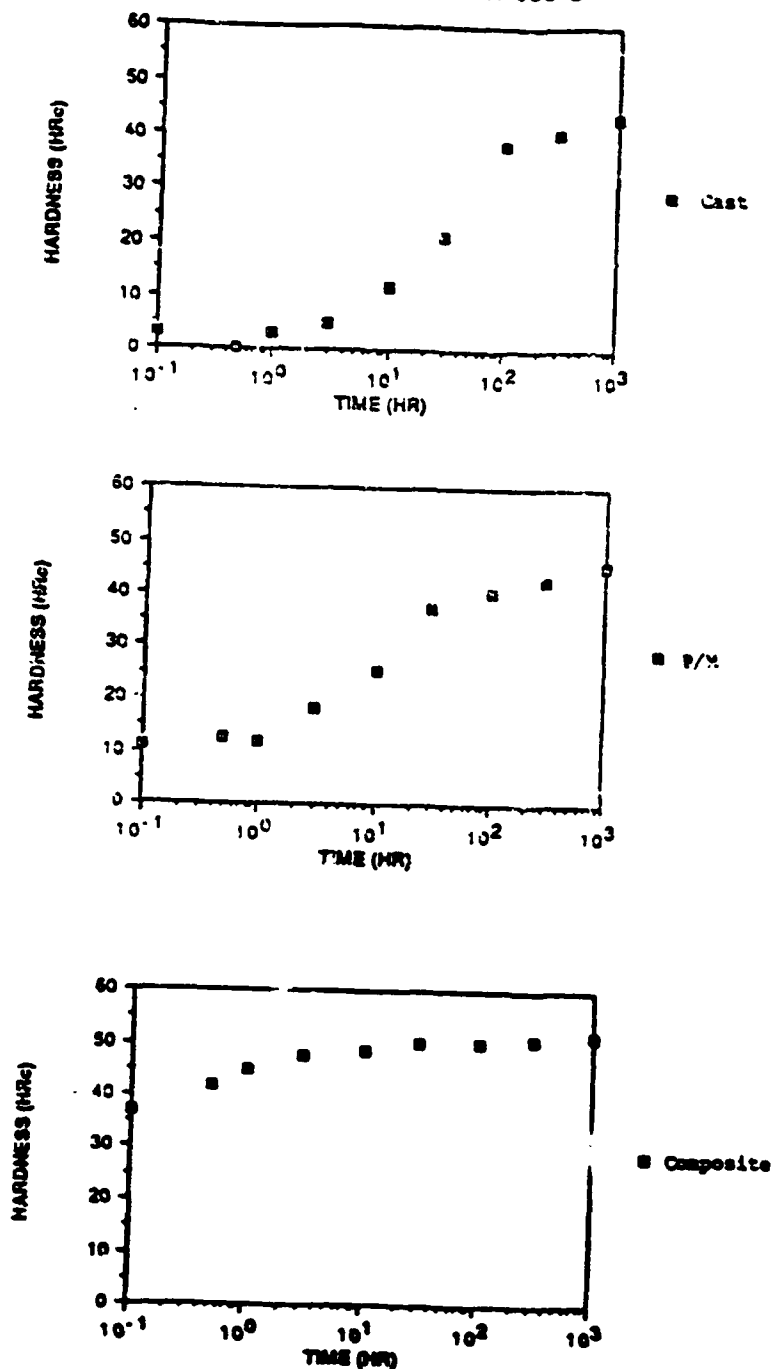


Figure 9. Continued.

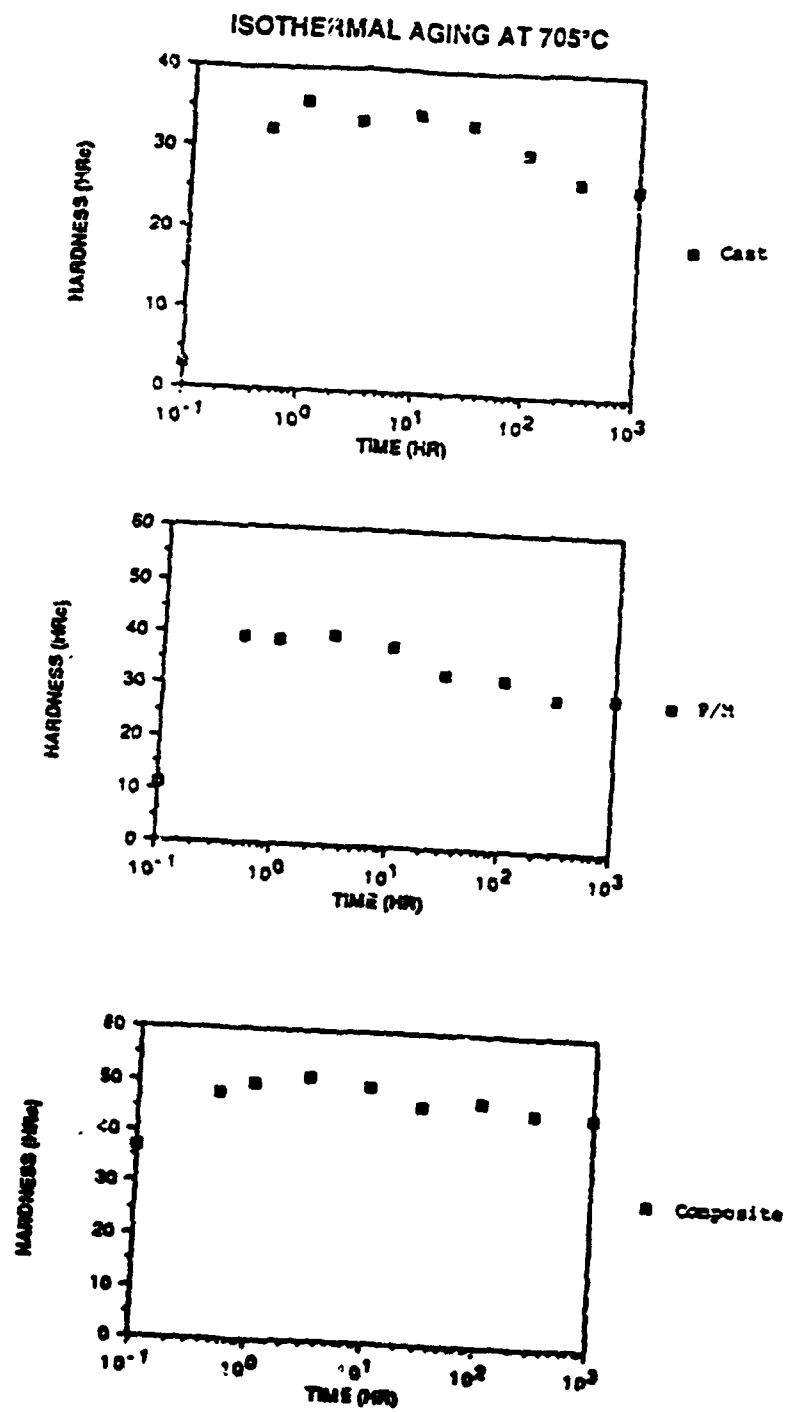
## ISOTHERMAL AGING AT 650°C



(a)

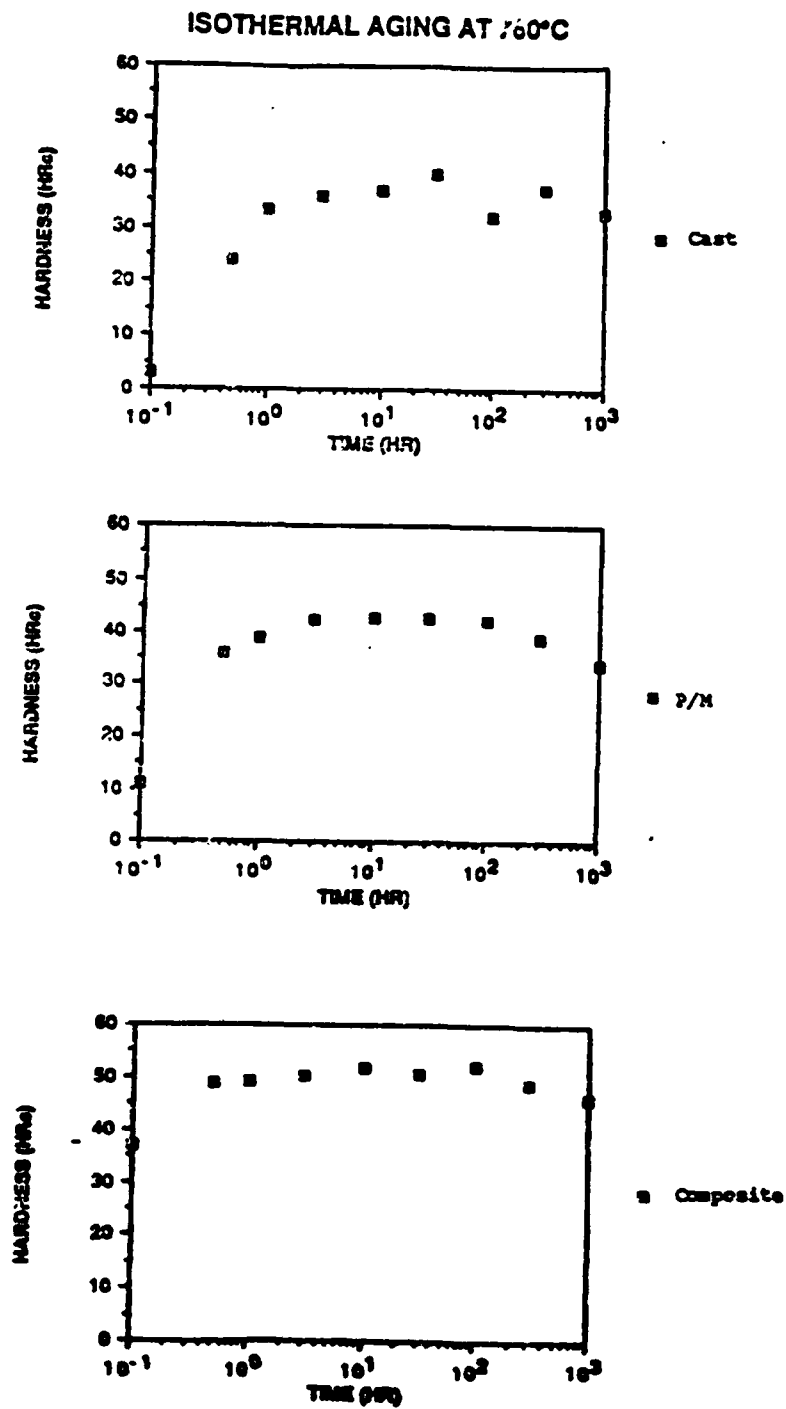
Figure 10. Influence of Isothermal Aging on Hardness of Cast, P/M and 20 V/O Composite Inconel 718. Isothermal Aging Temperatures (a) 650°C, (b) 705°C, (c) 760°C, (d) 815°C and (e) 870°C. All Samples Solution Treated at 1150°C for 1 Hr. and Water Quenched Prior to Aging.





(b)

Figure 10. Continued.



(c)

Figure 10. Continued.

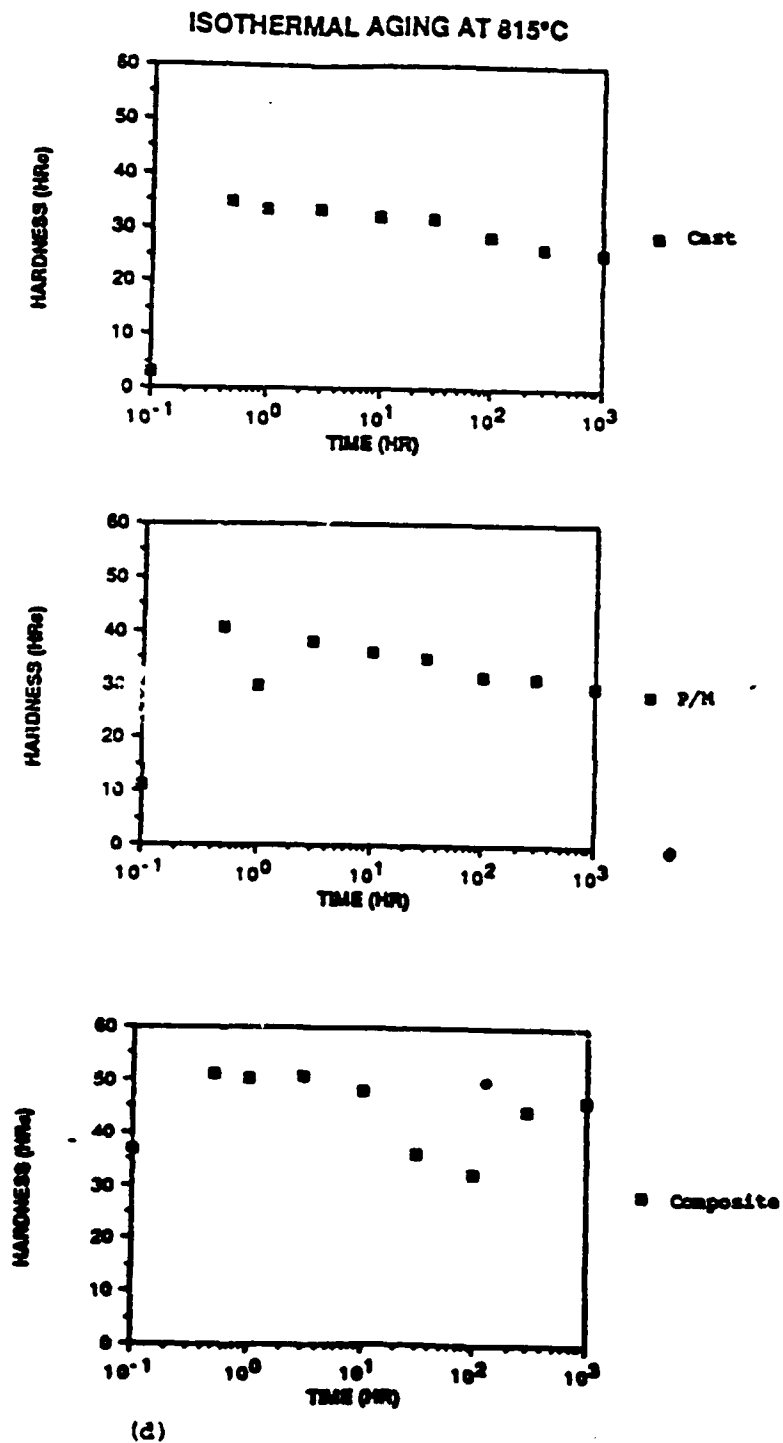


Figure 10. Continued.

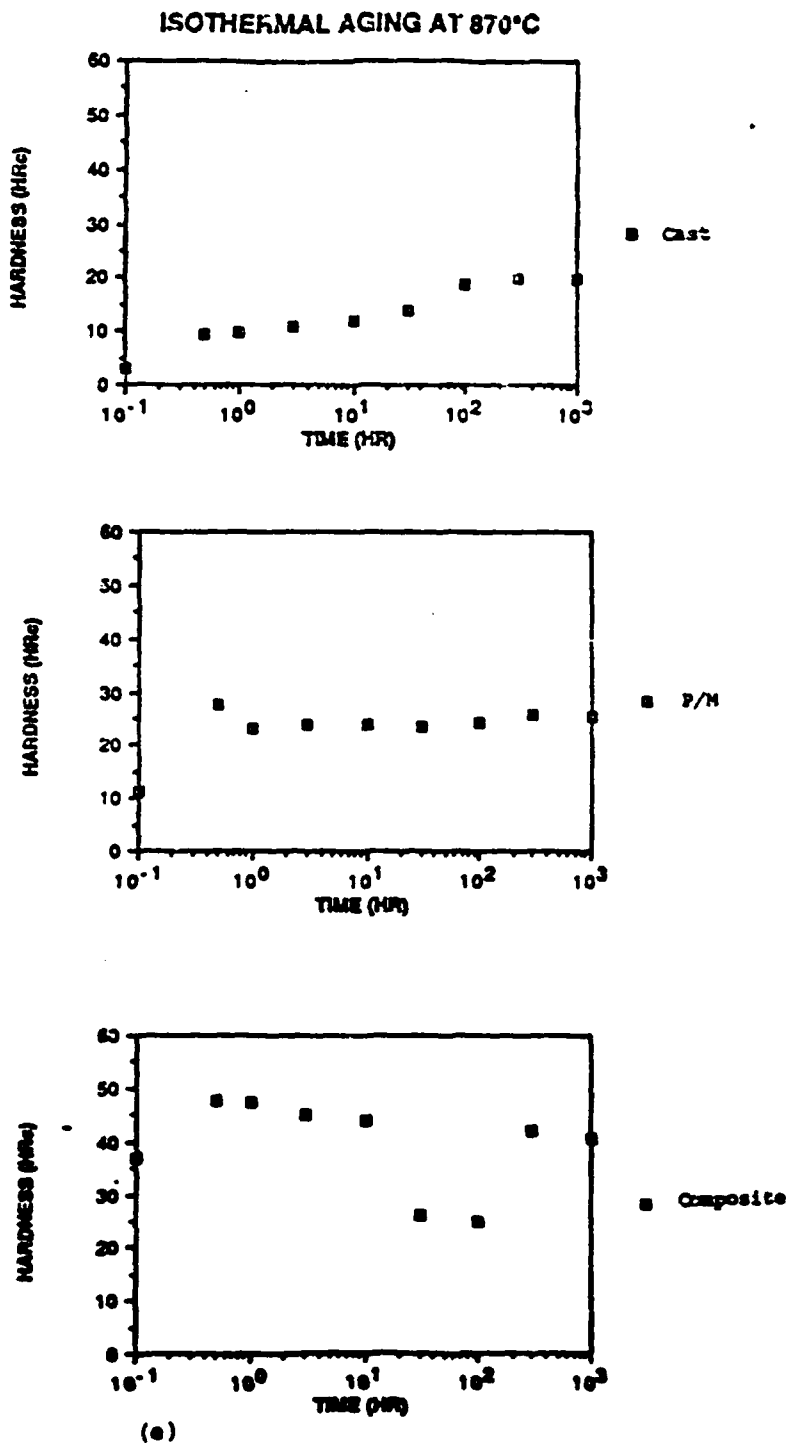
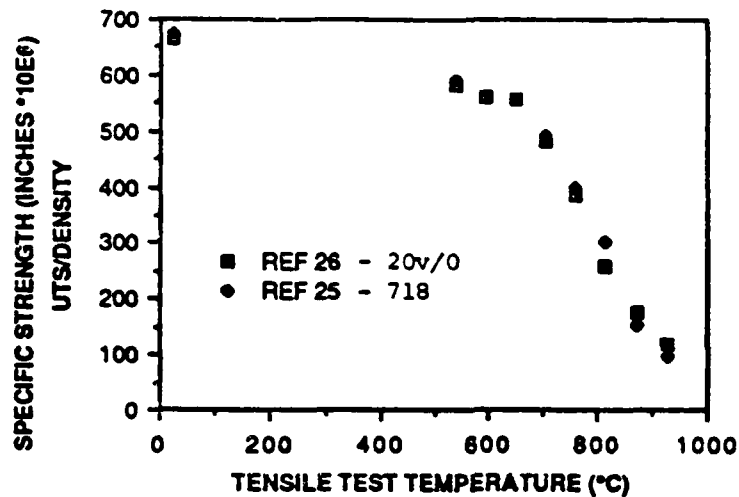
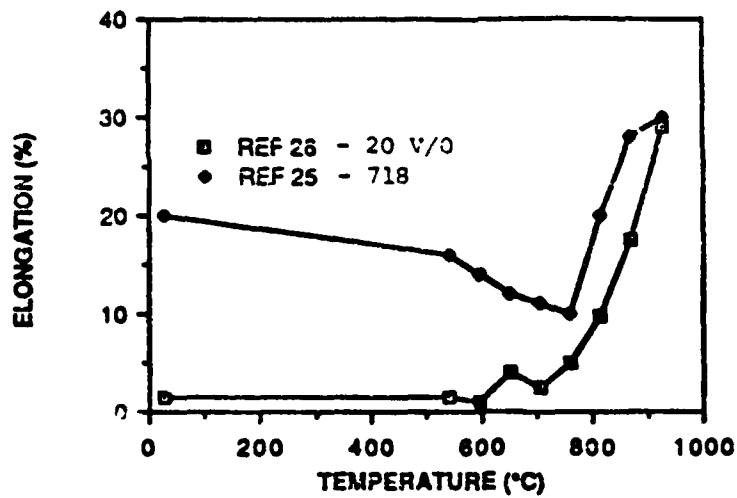


Figure 10. Continued.



SOLUTION TREATED AT 955°C FOR 1.5 HR AND N2 GAS QUENCH  
AGED AT 718 °C FOR 8 HR, COOLED @ 45°C/HR TO 621°C 8 HR AND AIR COOLED

Figure 11. Elevated Temperature Tensile Properties.



SAMPLES SOLUTION TREATED AT 955°C FOR 1.5 HR AND N<sub>2</sub> GAS QUENCHED  
AGED AT 718 °C FOR 8 HR, COOLED @ 45 °C/HR TO 621°C AND AIR COOLED

**Figure 12. Elevated Temperature Ductility of Composite and Cast Material.**



Figure 13. Fractograph of Elevated Temperature Tensile Failure in 718.



Figure 14. Fractograph of Elevated Temperature Tensile Failure of TiC Reinforced Composite.



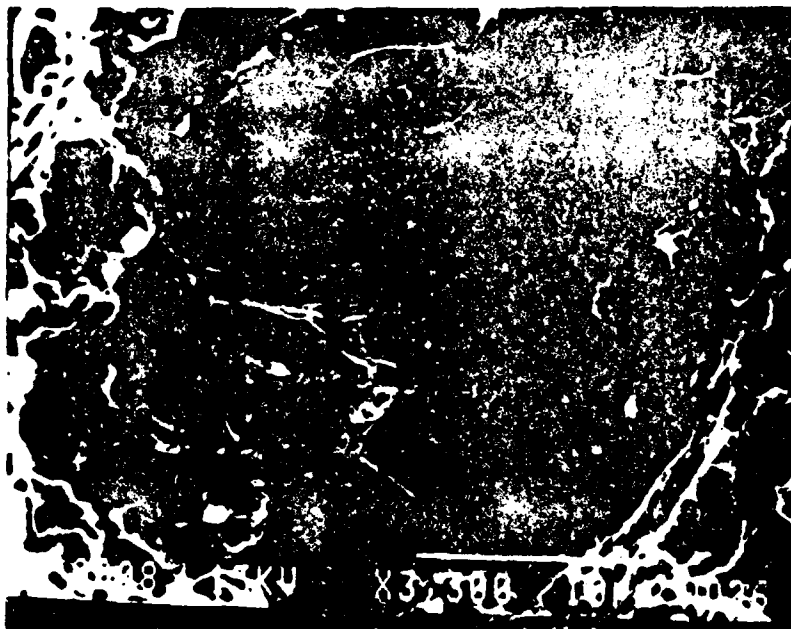


Figure 15. Fractograph of Clamped TiC in Elevated Temperature Tensile Test Fracture Surface.

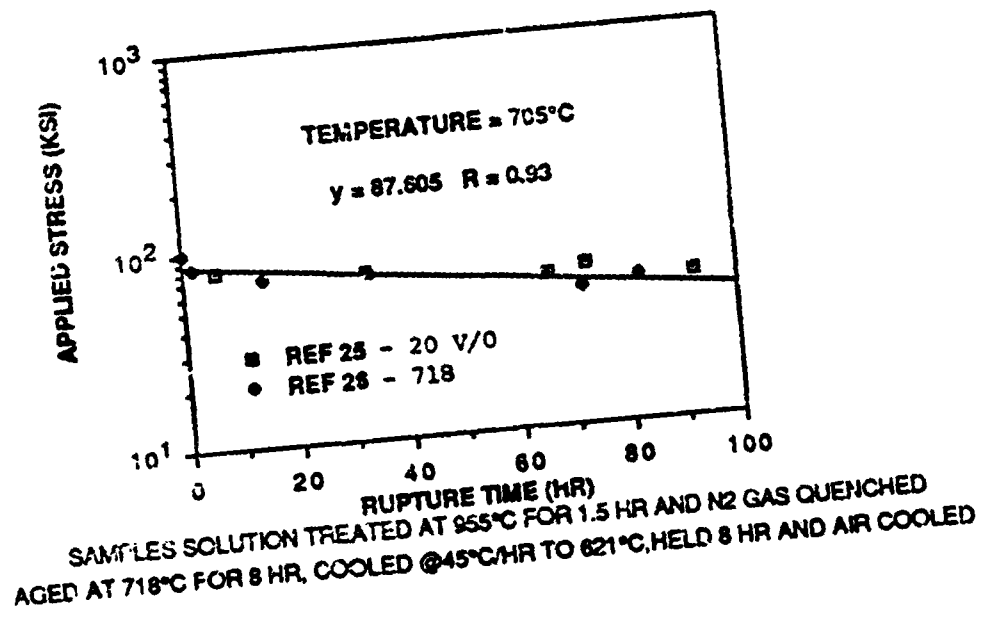


Figure 16. Stress Rupture Data.

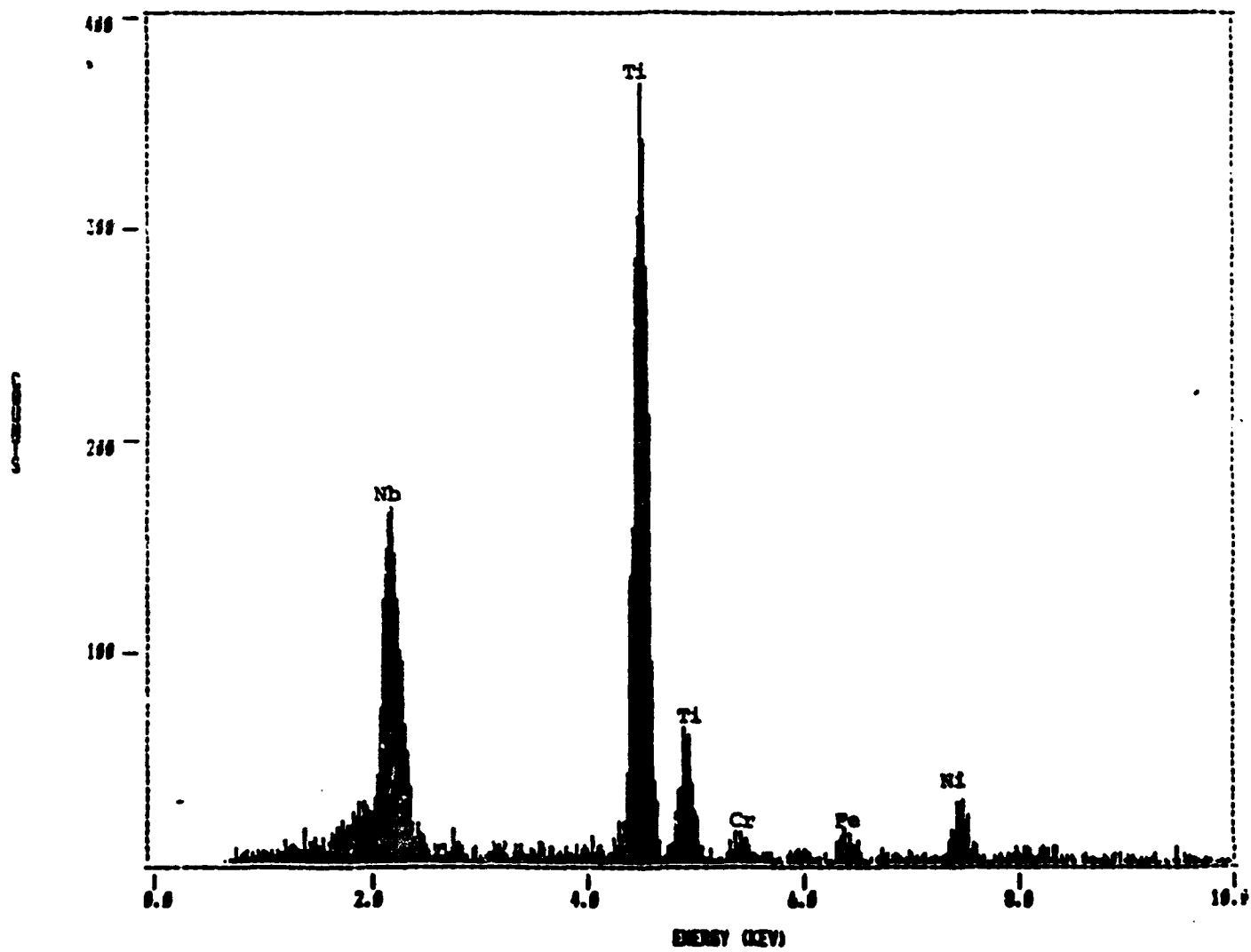


Figure 17. TEM EDS Spectrum of (Nb/Ti)C Precipitate.

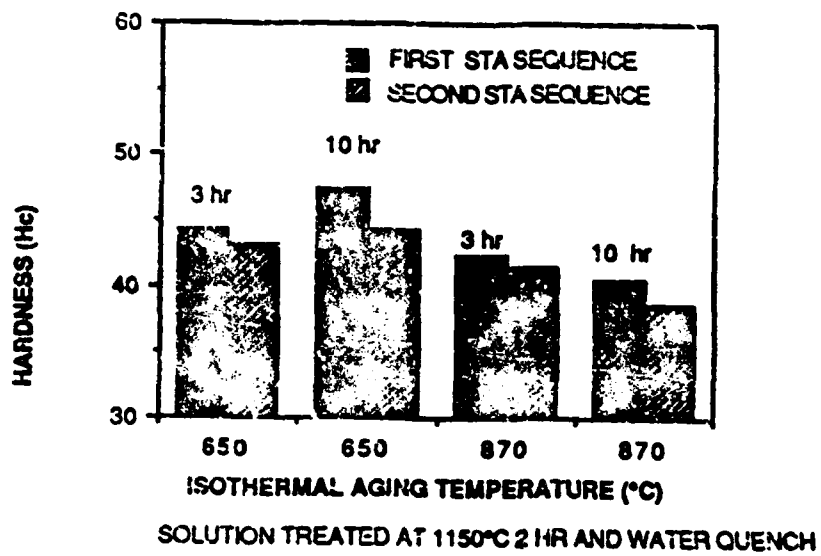


Figure 18. Reversibility Study.

**PART 2**

**CHARACTERIZATION**



## **Interfacial Structure and Stability in Metal and Intermetallic Matrix Composites (Year 2)**

**James M. Howe, Investigator**

Research during the second year of this program concentrated on achieving two objectives: i) complete the research on microstructural evolution and measurement of residual strains in Al/SiC<sub>w</sub> composites that was begun in the first year, and ii) begin research on the structure and deformation of TiAl and Ti<sub>3</sub>Al base matrices, since these appear to be the most promising candidates for future high-temperature composites. Excellent progress was made in both areas, as summarized below.

### **i) Microstructural Evolution During Heat Treatment and Deformation in Al/SiC**

A detailed microstructural analysis of a 2124-Al/SiC<sub>w</sub> composite during heat treatment and deformation was performed in order to understand the role of the interface on the mechanical properties. Results indicate that extensive precipitation of the S-phase at the Al/SiC<sub>w</sub> interface during aging leads to cracking of SiC whiskers during deformation. This, coupled with void formation at SiC clusters, appears to be the major cause for the low ductility of the composite. This research was presented at a symposium on Composite Materials at the 44th Annual Meeting of the Electron Microscopy Society of America in August, 1988 (Attachment I) and a manuscript was just completed for submission to Acta Metallurgica (Attachment II).

### **ii) Measurement of Residual Stress in Al/SiC Composite**

It has been suggested that residual stresses near the interface in Al/SiC<sub>w</sub> composites cause accelerated aging and significant strengthening, although these stresses have not been measured directly. In this study, local residual strains (stresses) around SiC<sub>w</sub> were measured using convergent-beam electron diffraction (CBED). Results indicate that strains on the order of 0.2%, which correspond to the macroscopic yield stress, are present near the interface and

diminish to zero about 1  $\mu\text{m}$  away. Measurement of the strains required considerable development of the CBED technique. The results are summarized in Attachment III and a manuscript is in preparation for submission to Acta Metallurgica.

### iii) Structure and Deformation of $\alpha_2/\gamma$ Interface in TiAl Alloy

As an initial step toward understanding the role of interfacial structure on deformation in TiAl alloys, a detailed microstructural analysis of an  $\alpha_2/\gamma$  alloy was performed. Results indicate that the  $\alpha_2/\gamma$  interface contains a dense array of  $a/6\langle 112 \rangle$  partial dislocations which accommodate misfit and enable growth of and the  $\alpha_2$  and  $\gamma$  phases. Deformation at high temperatures occurs by a twinning mechanism, and twinning dislocations cut through both the  $\alpha_2$  and  $\gamma$  phases. This research was presented at a symposium on Titanium: Surface and Interfaces at the World Materials Congress in September, 1988 and a manuscript was submitted to Metallurgical Transactions A (Attachment IV).

### iv) Structure and Deformation of $\alpha_2/\beta$ Interface in $\text{Ti}_3\text{Al}$ Alloys

The  $\alpha_2/\beta$  interface appears to play a critical role in the deformation of  $\text{Ti}_3\text{Al}$  base alloys although little is known about the structure of the interface. In order to understand  $\text{Ti}_3\text{Al}$  base composites, a detailed microstructural examination of the  $\alpha_2/\beta$  interface and deformation mechanisms in each phase has been undertaken. A Ti-7Mo-16Al (at.%) alloy is being studied because of the variety of ordered and disordered h.c.p./b.c.c. interfaces that can be obtained in this system. As shown in Attachment V, rod-shaped  $\alpha_2$  precipitates have a Burgers orientation relationship with the  $\beta$  matrix and contain  $\langle c+a \rangle$  misfit dislocations spaced about 10 nm apart. Large-grain tensile specimens are being deformed to understand the role of this interface on deformation.

### v) Additional Presentations and Publications

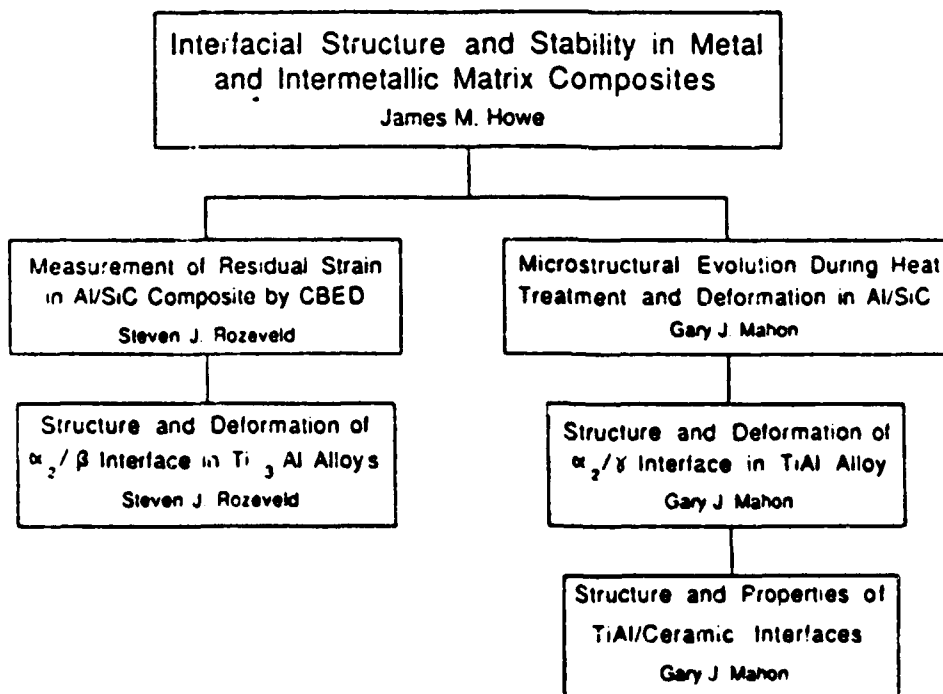
An invited paper on High-Resolution TEM of Precipitate Growth by Diffusional and Displacive Transformation Mechanisms was



presented at the 44th Annual Meeting of E.M.S.A. and has been accepted for publication in Ultramicroscopy (Attachment VI). This work was partially supported under the present grant.

### Plans for the Third Year

Our experience with the Al/SiC composites has indicated that it is difficult to understand the role of the interface on composite properties because there are many factors involved in a commercial material. During the third year we plan to circumvent this problem by fabricating bi-layer specimens of SiC and other ceramics with TiAl and Al-alloy matrices, and examine the strength of these interfaces as a function of heat treatment and interfacial reaction. Detailed microstructural analyses of the interfaces will be performed in order to understand the mechanisms of strength and degradation. When high-quality composites based on TiAl become available, we will compare the interfaces in these materials with those in the bi-layer specimens. We will also continue to investigate the role of the  $\alpha_2/\beta$  interface in deformation and begin to look at bi-layer specimens of these alloys as well. The flow-chart below outlines the direction of this program to date.



**Attachments**

	<u>Page</u>
<u>Attachment I.</u> Reprint from <i>Proc. 44th EMSA Meeting</i>	177
<u>Attachment II.</u> Manuscript submitted to <i>Acta Metallurgica</i>	179
<u>Attachment III.</u> Residual stresses in Al/SiC <sub>w</sub> composites - summary	209
<u>Attachment IV.</u> Manuscript submitted to <i>Met. Trans. A</i>	214
<u>Attachment V.</u> Summary of hcp/bcc interface observations	249
<u>Attachment VI.</u> Invited paper, accepted for <i>Ultramicroscopy</i>	253

## ATTACHMENT I

G. W. Bailey, Ed., *Proceedings of the 4th Annual Meeting of the Electron Microscopy Society of America*  
Copyright © 1988 by San Francisco Press, Inc., Box 680A, San Francisco, CA 94101-6800, USA

# MICROSTRUCTURAL DEVELOPMENT DURING HEAT TREATMENT AND DEFORMATION OF AN ALUMINUM-SILICON CARBIDE COMPOSITE

G. J. Mahon and J. M. Howe

Department of Metallurgical Engineering and Materials Science, Carnegie Mellon University, Pittsburgh, PA 15213

Aluminum-SiC reinforced composite alloys are currently being considered for structural applications in the aerospace industry as a result of their increased strength and stiffness and reduced density when compared with their monolithic counterparts.<sup>1</sup> However, the main drawback of these materials is their lack of tensile ductility and a decrease in fracture toughness.<sup>2</sup> By deforming Al-SiC composites under hydrostatic pressure the tensile ductility can be increased.<sup>3</sup> This enables changes in microstructure to be investigated after a few percent strain, thus providing information about deformation mechanisms in this class of materials. Conventional TEM techniques have been applied to study microstructural development during both heat treatment and deformation.

The material studied was AA2124 with 13vol.%SiC, commercially manufactured by ARCO Chemicals using a process of hot compaction and extrusion. The material was solutionized at 504°C for 4 h, quenched and aged at 177°C for 8 h. Tensile bars were strained 3% parallel to the extrusion direction under 100 ksi hydrostatic pressure. TEM specimens were prepared by ion-milling in a liquid nitrogen cold-stage.

During quenching from the solutionizing temperature, dislocations are produced in the Al as a result of the difference in thermal expansivity between the fibers and matrix (Fig. 1). Furthermore, the dislocations (A) were produced from the corner of the SiC whisker, demonstrating that such asperities act as a stress concentrator. Also note the helical dislocations (B) which were formed by condensation of excess vacancies onto screw dislocations.<sup>4</sup> These helices were also associated with  $Mn_3Cu_2Al_{10}$  intermetallic particles which are distributed throughout the material, and often terminate at the particle/matrix interface.

Upon subsequent aging, S' precipitates form heterogeneously on the dislocations. Since this phase occurs as laths which grow preferentially in the  $\langle 100 \rangle_{Al}$  direction,<sup>5</sup> one-third of the precipitates can be seen end-on by imaging along  $\langle 100 \rangle_{Al}$ . Figure 2 shows helices decorated with these laths, and indicates that only one of the precipitate variants forms on dislocations of any given Burgers vector. In the regions closest to the whiskers where the dislocation density is highest, individual precipitates are not distinguishable. Thus, the strength of the matrix is likely to vary considerably depending on proximity to fibers, since this will affect the dislocation and S' precipitate densities. Coarse precipitation has also been observed at whisker/matrix interfaces, intermetallic/matrix interfaces, and grain boundaries.

After deformation, several new features appear in the microstructure. The most obvious is cracking of the SiC whiskers in a direction perpendicular to their long axis (Fig. 3). Some cracked intermetallics are also found, one of which is also shown in Fig. 3. There is no matrix failure associated with these cracked particles. Evidence has also been found for decohesion of matrix/SiC interfaces, even when the interface lies almost parallel to the tensile direction. Finally, faceted voids are formed in constrained matrix between two or more whiskers (Fig. 4) and also at the ends of apparently isolated fibers.<sup>6</sup> Further work is being performed to establish which of these features develop first, and which are critical in determining the fracture characteristics of these materials.<sup>7</sup>

## References

1. D. L. McDaniels and C. A. Hoffman, NASA Technical Paper 2392 (1984).
2. A. D. Divecha and S. G. Fishman, in *Proc. 3rd Int. Conf. on Mechanical Behavior of Materials* (eds. K. J. Miller and R. F. Smith) Pergamon Press (1980) 351.
3. A. K. Vasudevan, private communication.
4. G. Thomas and M. J. Whelan, *Phil. Mag.* 4 (1959) 511.
5. J. M. Silcock, *J. Inst. Metals* 89 (1961) 203.
6. S. R. Nutt and J. M. Duva, *Scripta Met.* 20 (1986) 1055.
7. This research was supported by the AFOSR under grant no. F49620-87-C-0017, and is being performed in collaboration with A. K. Vasudevan and A. COA.

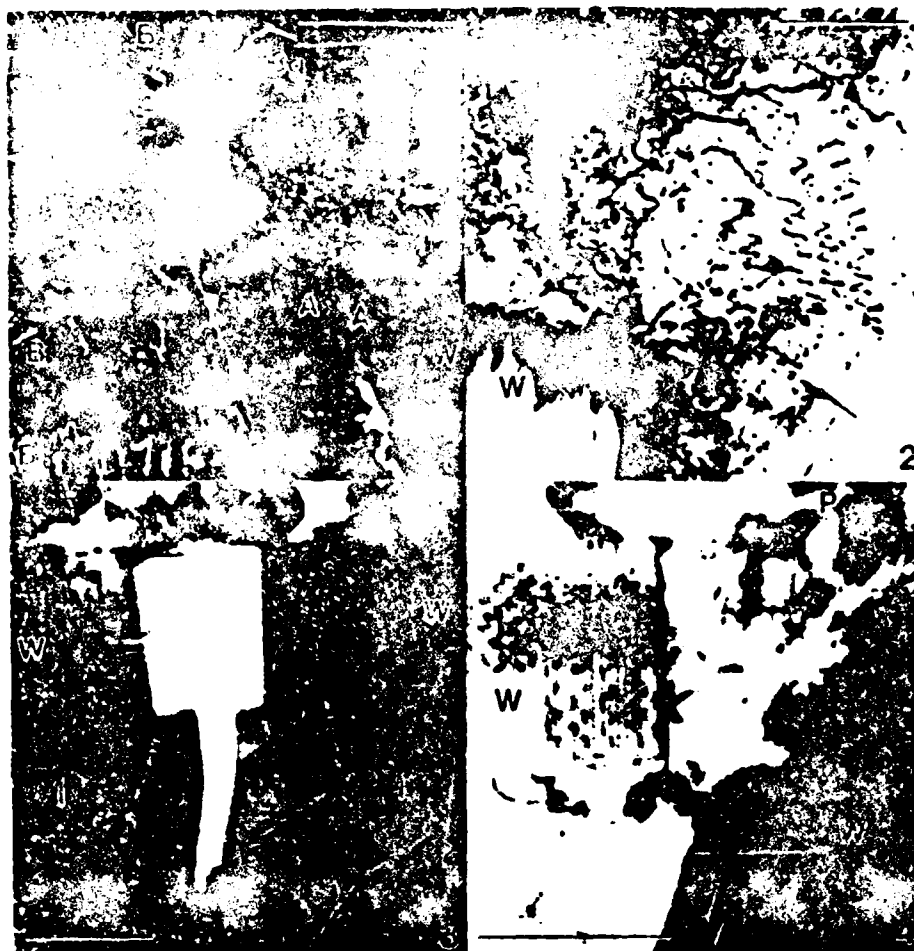


FIG. 1.--Weak-beam micrograph of dislocation generation at SiC whisker (W). Note dislocations produced at corner (A) and helices (B).  $g/3g = [-11]$ . Bar = 0.2  $\mu\text{m}$ .  
 FIG. 2.--Heterogeneous precipitation of  $S'$  on dislocations. Beam direction near  $[100]_{\text{Al}}$ . W = SiC whisker. Bar = 0.3  $\mu\text{m}$ .  
 FIG. 3.--Cracked SiC whisker (W) and intermetallic particle (i). Bar = 0.3  $\mu\text{m}$ .  
 FIG. 4.--Faceted void at SiC whisker (W) ends. P = coarse grain boundary precipitates. Bar = 0.2  $\mu\text{m}$ .

**Microstructural Development and the Effect of Interfacial  
Precipitation on Deformation Under Hydrostatic Pressure  
In an Aluminum/Silicon-Carbide Composite**

**G. J. MAHON, J. M. HOWE and A. K. VASUDEVAN\***

Department of Metallurgical  
Engineering and Materials Science  
Carnegie Mellon University  
Pittsburgh PA 15213

\*Office of Naval Research  
Applied Research and Technology Directorate  
800 N. Quincy St., Code 1216  
Arlington VA 22217-5000

**ABSTRACT**

A 2124 Al/SiC whisker composite was heat-treated to the same matrix hardness in an underaged and overaged condition, and tensile tests were performed at room pressure and under hydrostatic pressure. The overaged composite had a lower ultimate tensile strength and ductility, which was attributed to S-phase precipitation at the Al/SiC<sub>w</sub> interface. This interfacial precipitation leads to increased load transfer to the whiskers, resulting in early failure during testing. Hydrostatic pressure does not increase the tensile ductility, indicating that failure occurs by strain localization. Microstructural examination suggests that such localization is probably due to cracking of SiC whiskers and void nucleation in constrained regions between adjacent SiC whiskers.

## 1. INTRODUCTION

Aluminum/silicon-carbide composites are attracting much attention for potential aerospace applications as a result of increased strength and decreased density when compared with conventional Al alloys [1,2]. However, the use of these materials is limited by their low fracture toughness and ductility. There has been much work done on this class of materials, including examination of: (i) the microstructure of the alloys and the effect of adding SiC on the matrix [3,4], (ii) dislocation generation in the matrix due to the difference in coefficient of thermal expansivity between the two phases [5-7], (iii) precipitation in the matrix [8-14] and at interfaces [15-18], (iv) micromechanisms of failure [16-23], and (v) strengthening mechanisms in the composites [24-30]. However, few if any of these studies have followed microstructural evolution throughout the processing and deformation stages in order to understand the mechanical properties. As such, it is difficult to generalize about mechanisms of deformation and fracture in these materials and to determine if many reported observations are system specific.

While it is commonly accepted that interfaces play an important role in the mechanical properties of composite materials, there have been few investigations which have been able to isolate the effects of interfacial strength on the resulting properties. This is primarily due to the complex interaction between the SiC reinforcement and the age-hardening matrices, since the aging behavior can change the matrix strength, ductility, and deformation mechanism, as well as the interfacial bonding, which in turn affect the overall composite properties. In order to try and isolate the effect of interfacial bonding on the properties of an Al/SiC<sub>w</sub> composite, the following study was undertaken. The matrix of a 2124/SiC<sub>w</sub> composite [31,32] was heat-treated to nominally the same hardness in an underaged and overaged condition based on published microhardness curves [10]. Unreinforced material was also heat-treated to the same nominal matrix hardness, again in an underaged and overaged condition, in order to verify that there was no change in the tensile behavior of the matrix in these two

conditions. TEM was also used to verify that the reinforcement only acts to accelerate aging and does not affect the resultant phases or deformation mechanism. By having the same matrix properties, any differences in deformation behavior of the reinforced materials in the underaged and overaged conditions should be a result of the change in interfacial strength.

In addition, deformation studies at room pressure and under hydrostatic pressure were performed on this material in order to understand the lack of ductility. Deformation under hydrostatic pressure has been shown to increase tensile ductility in many alloy systems by suppressing void growth and coalescence, but without affecting the void nucleation stage [33,34]. Thus, by applying a hydrostatic pressure during deformation, there exists the potential for extending ductility in these materials in order to examine deformation at larger strains than could normally be achieved. This would lead to a detailed knowledge of void nucleation in these discontinuously reinforced composites.

The results presented here will include a detailed study of microstructural development in this alloy in order to isolate the effects caused solely by the deformation, and hence give a complete picture of microstructural evolution during heat treatment and deformation. Suggestions are made for improvements of the mechanical properties of this class of materials.

## 2. EXPERIMENTAL

### 2.1. Material

The material for this investigation was manufactured by ARCO Chemical Company using a method of hot compaction and extrusion. Unreinforced and reinforced materials were produced using identical methods, as described elsewhere [10]. The matrix alloy was AA2124 (nominally 4 at.% Cu, 2 at.% Mg, 0.5 at.% Mn) reinforced with 13.5 vol.% SiC whiskers.

## 2.2. Heat Treatment

The as-received materials were solutionized at 504°C for 4 hours and quenched into ice water. Subsequent aging was carried out at 177°C. The reinforced material was aged for 2 hours (underaged) and 8 hours (overaged); the unreinforced material for 4 hours (underaged) and 14 hours (overaged), all of which produced a matrix hardness of about 94 Vickers DPH.

## 2.3. Deformation

Tensile specimens were produced with the tensile axis parallel to the extrusion direction. Specimens were tested to failure, and a set from the reinforced materials were stopped at 3% true strain. The unreinforced alloy was also sectioned at 3% true strain by preparing a specimen from the necked region of the fractured material with the corresponding reduced area. Hydrostatic pressures of 0.1 MPa (room pressure) and 689 MPa (100 ksi) were applied during the tests.

## 2.4. Specimen Preparation

Specimen preparation was designed to ensure that dislocations were not produced by deformation and that there was no excessive specimen heating. This was achieved by cutting 250µm slices using a diamond blade and thinning to 125µm on 600 grit SiC paper. The reinforced material was then further thinned on a Gatan dimpler to 30µm followed by ion-milling at 5keV, 0.2mA per gun and 12° incident angle on a Gatan dual-beam ion-mill with a liquid-nitrogen cold stage. The undeformed material was taken from the ends of the tensile specimens to ensure the same heat treatments had been applied in both cases. The final stage of preparation for the unreinforced material was electropolishing in a Fischione twin-jet polisher using a 1/3 nitric-2/3 methanol solution at 15 V and -30°C.



## 2.5. Microstructural Examination

Specimens were examined in a Philips EM420 equipped with a STEM unit and a PGT Energy Dispersive X-ray (EDX) analysis system. The microanalysis system was used to provide qualitative chemical information from the Al/SiC<sub>w</sub> interface and for precipitate analysis. Bright-field and weak-beam dark-field TEM images were obtained at 120 keV using conventional procedures [35].

## 3. RESULTS

### 3.1. Microstructural Development During Heat Treatment

#### 3.1.1. Aluminum/Silicon-Carbide Composite

##### (I) As Quenched

Quenching of the composite from the solutionizing temperature produced the type of dislocation distribution shown in Fig. 1. This weak-beam dark-field TEM image shows two types of dislocations. One is helices formed in the matrix slightly away from and occasionally in contact with the SiC whiskers. These are formed as a result of condensation of excess vacancies onto pre-existing screw dislocations [36,37] and thus, must be formed during the early stages of the quench, when the vacancies are still mobile. The second type of dislocations are those seen at the ends of SiC whiskers and which often appear to terminate in the Al/SiC<sub>w</sub> interface at a corner (arrows in Fig. 1). These dislocations are produced as a result of the difference in coefficient of thermal expansivity between the Al matrix and SiC whiskers [5,6] and are presumably formed at a temperature where the vacancies are essentially immobile. The micrograph in Fig. 1 shows that the corners of the SiC whiskers act as stress concentrators and assist in dislocation generation. There is no evidence of discrete dislocation loops in the microstructure.

## (II) Underaged

After aging for 2 hours at 177°C there is evidence of small precipitates on the pre-existing dislocations, as shown in Fig. 2. However, it is very difficult to detect extra diffraction spots in the electron diffraction pattern, preventing complete identification of the phase at this stage. When compared with the overaged microstructure, it is most probably the S' phase ( $\text{Al}_2\text{CuMg}$ ).

## (III) Overaged

After 8 hours at 177°C, precipitation at dislocations is well advanced. This is shown in Fig. 3, where bright-field and centered dark-field TEM images demonstrate that precipitates completely decorate the prior dislocations. The diffraction pattern is consistent with the S' phase [38] and this is presumably the same phase which was present in the underaged condition. Since the S' phase occurs as laths which grow preferentially in the  $\langle 100 \rangle_{\text{Al}}$  direction [39,40], one-third of the precipitates can be seen end-on by imaging along  $\langle 100 \rangle_{\text{Al}}$ . From Fig. 3 it is apparent that only one set of variants of S' is nucleated on any particular dislocation, indicating that the heterogeneous nucleation of this phase occurs as a result of misfit accommodation by the Burgers vector of the dislocation [40]. Since the dislocations are heterogeneously distributed in the matrix as shown in Fig. 1, so are the age-hardening precipitates.

The general microstructure produced after aging for 8 hours is illustrated in Fig. 4. This many-beam bright-field TEM image shows the extent of precipitation in the matrix and, more significantly, the extensive precipitation decorating almost the entire  $\text{Al}/\text{SiC}_w$  interface.

## (IV) Microanalysis of Interfaces

The interface chemistry in the as-quenched material has been compared with that in the overaged condition using STEM and EDX microanalysis. A typical spectra from the

as-quenched condition is shown in Fig. 5(a). The major peaks present are Si and Al associated with the  $\text{SiC}_w$  and matrix, respectively. The smaller peaks are from Cu and Mg in solution. There are no other large peaks, indicating the absence of any gross precipitation at the interface. This is supported by the micrograph in Fig. 1, where there is some evidence of small Cu and Mg-rich precipitates, but these are fairly scarce. This may be compared with the microstructure in Fig. 4, where considerable interface precipitation has occurred during aging, leading to the typical EDX spectra shown in Fig. 5(b). The extra peaks are Cu and Mg, which from their concentration ratio are consistent with the S-phase, i.e., the Cu:Mg ratio is close to 1:1. These observations are similar to previous results in the literature [17,18]. As will be seen later, this interface precipitation appears to be responsible for a change in the tensile properties between the underaged and overaged materials.

### 3.1.2. Aging Behavior of Unreinforced Alloy

Many of the features discussed above for the Al/ $\text{SiC}_w$  composite appear to occur in the unreinforced alloy. Figure 6 is a bright-field TEM image taken after quenching and aging for 14 hours that shows a large  $\text{Al}_{20}\text{Cu}_2\text{Mn}_3$  intermetallic particle (seen frequently in both materials) from which helical dislocations have formed. In addition, there are discrete dislocation loops in the matrix, some of which may have formed by the continued condensation of vacancies onto screw dislocations. However, other loops are much larger than would be expected from this mechanism, and were probably formed by condensation of vacancies directly into loops in the matrix [37]. The dislocation density of the unreinforced material was much lower than that of the composite material, although no quantification has been attempted due to the heterogeneous dislocation distributions in both cases. During subsequent aging there was once again heterogeneous precipitation of S'-phase at the dislocations, as was seen for the composite. There was also precipitation of presumably S phase at the intermetallic/matrix interfaces.

### 3.2 Tensile Tests

The tensile results for all the materials are plotted in Fig. 7, which shows true stress versus true plastic strain. The plastic portion of the strain was determined by subtracting the elastic component, which was obtained by fitting a straight line to the linear portion of the original stress/strain curves. The plastic ductility was obtained by measuring the plastic extension at maximum load (plastic instability). Analysis of the tensile data are not complete, but the following preliminary conclusions can be drawn.

For the unreinforced 2124 tested at 0.1MPa, the U.T.S. and plastic ductility of the underaged and overaged material appear to be nearly identical; the overaged material work hardens a little more, and has about 2% less plastic strain at instability. This is consistent with previous results [10] and supports the rationale used in designing the experiments performed in this study, where 4 and 14 hour heat treatments (or 2 and 8 hour in the reinforced material) were used to give identical matrix properties.

The addition of SiC whiskers to the material produced a dramatic increase in U.T.S. and work hardening rate, but, as expected a significant decrease in the ductility. For the composite materials, the most important feature to note is that the underaged material exhibits both a greater U.T.S. and ductility than the overaged composite when tested at 0.1MPa (approximately 680 MPa and 5% plastic strain vs. 640MPa and 3% plastic strain). Furthermore, testing under 689MPa hydrostatic pressure did not significantly affect the tensile behavior of either the underaged or overaged composite materials, with only about an increase of 1% in the plastic strain. In the discussion which follows, these results will be compared with the microstructural information to provide an overall picture of deformation in the Al/SiC<sub>w</sub> composites.

### 3.3. Deformation-Induced Microstructures

After 3% deformation both the underaged and overaged reinforced and unreinforced materials have considerable dislocation tangles in the matrix. These can be distinguished from the dislocations present prior to deformation since all the dislocations present prior to aging are decorated with precipitates. A detailed analysis of these dislocations has not been attempted due to the excessive strain contrast associated with the dense S' precipitates, however, there was no evidence of planar slip in any of the microstructures.

Several other features were introduced into the overaged composite during deformation. None of these were present in the undeformed material. The most common form of damage was cracking of SiC whiskers in a direction perpendicular to their long axis, i.e., along a  $\{111\}_{\beta\text{-SiC}}$  plane. Figure 8 shows one of these cracked whiskers together with an adjacent intermetallic  $\text{Al}_{20}\text{Cu}_2\text{Mg}_3$  particle which has also cracked. Note that there is no matrix failure associated with the cracked particles. Furthermore, the separation at the SiC whisker is greater than that at the intermetallic, indicating that it fractured first.

Other features are also introduced during deformation, but they are much less common. Figure 9 shows decohesion at the  $\text{Al}/\text{SiC}_w$  interface. This may have occurred as a result of the slight misalignment of the whisker with respect to the tensile axis. The SiC side of the opening appears relatively clean; what evidence there is of precipitation (arrows) occurs on the aluminum side, indicating that decohesion has occurred between the SiC and S phase rather than between the Al and the S precipitates.

Other features that were apparent after deformation were voids associated with the ends of SiC whiskers, as reported previously [17,18,22,23]. An important feature was that many of these voids were formed in the constrained regions between adjacent whiskers, as shown in Fig. 10. Other voids were associated with apparently isolated whiskers, as seen in Fig. 11, but this might be a result of sectioning during thin-film preparation where an adjacent

whisker either above or below has been removed. Note the highly faceted nature of the voids in both Figs. 10 and 11; the reason for this is not known.

Microstructural analysis of the underaged composite revealed much less damage when compared with the overaged composite. There were far fewer cracked SiC particles, and no evidence was found for the formation of voids or of interface decohesion after 3% strain. As will be discussed below, this appears to be due to a change in the interfacial characteristics between the underaged and overaged composite.

#### 4. DISCUSSION

##### 4.1. Tensile Data

As pointed out in the results section, analysis of the tensile data is not yet complete. However, by comparing these results with the microstructural observations made using TEM, some interesting conclusions can be reached regarding the role of the interface on the composite properties.

The reason for the various heat treatments used in this study was to produce matrices with the same hardness despite having different microstructures. As seen from the tensile data for the unreinforced 2124 alloy, very similar yield strengths and ductilities occur for the two aging times used. Based on the available studies in the literature [8-14], it seems reasonable to conclude that the major effect of the reinforcement on the age-hardening response of the matrix is to alter the precipitation kinetics of the age-hardening phase.

As shown earlier in Fig. 7, the tensile curves for the reinforced material after aging for 2 and 8 hours exhibit different characteristics; the overaged composite having a lower U.T.S. and ductility than the underaged composite. This behavior can be explained by relating it to the microstructural observations. Firstly, during aging of the composite there is copious S-phase precipitation at the Al/SiC interface. Secondly, the microstructure of the overaged

composite after 3% strain shows significantly more cracking of the SiC whiskers compared with the underaged composite. Assuming that the matrices do indeed have the same tensile characteristics, the differences in tensile behavior can therefore be attributed to the S-phase precipitation.

There are two possible explanations for how the S phase caused earlier fracture of SiC<sub>w</sub> in the overaged composite. The most likely is that S-phase precipitation at the interface causes increased load transfer to the SiC whiskers, causing them to fracture at lower strains. This idea that precipitation can alter load transfer to the reinforcement particles has been previously suggested in composites reinforced with different particles [41]. If this is the case, the elastic modulus of the overaged composite should be greater than that for the underaged material. The magnitude of this elastic modulus has been estimated from the true-stress/true-strain data. Although fitting a straight line to the elastic part of the stress/strain curve is not an accurate way of determining the elastic modulus, there does appear to be about a 5% increase in modulus of the overaged composite compared with the underaged material. This would seem to support the idea of increased load transfer due to S-phase precipitation, although an accurate measurement of elastic modulus in the two materials is necessary to confirm this.

The alternative explanation for earlier cracking of SiC<sub>w</sub> in the overaged composite is that precipitation at the interface causes an extra tensile strain to be introduced into the SiC<sub>w</sub> and that this "residual" strain causes the SiC to crack at a lower applied tensile stress. The exact nature of the stress which might be introduced by this precipitation has not been determined, being dependent on the orientation relationship between the SiC and the orthorhombic S phase and the volume expansion associated with the precipitates. No experimental evidence has yet been found to support this argument. In either case, the precipitation produces a lower ductility and ultimate tensile stress since the composite with the cracked fibers is unable to successfully carry the applied loads, leading to premature failure of the tensile specimens.

#### 4.2. Hydrostatic Pressure

Another aspect of this investigation was the application of hydrostatic pressure during tensile testing in an attempt to increase the plastic ductility in the composites by suppressing void growth and coalescence. The tensile results clearly show that in this particular composite it is not possible to suppress void nucleation and growth, and that failure occurs at almost the same strain at 689MPa as at room pressure. This indicates that failure occurs in a highly localized manner such that very little void growth and coalescence are required and that the governing factor in failure is the void nucleation stage. As mentioned above, whisker cracking is the most common feature introduced at 3% strain, and it is likely that this leads to early failure in the overaged composite. Such cracking could be avoided by using a fiber which can accommodate some deformation along its axis and/or by weakening the interfacial bond. In addition, voids are also generated in the constrained regions between adjacent whiskers at whisker ends, producing essentially the same type of defect in the matrix as that produced by cracking of the whiskers. This could also be responsible for the lack of an increase in ductility as a result of testing under hydrostatic pressure.

Therefore, the results from this investigation point to whisker cracking and void nucleation in the constrained regions between adjacent whiskers as major factors influencing the lack of tensile ductility in this particular composite. Reduced precipitation at the Al/SiC<sub>w</sub> interface (i.e., a weaker interface) increases both the U.T.S. and ductility, and elimination of clustering of the reinforcement would help to prevent void formation, and may also improve the tensile properties.

#### 5. CONCLUSIONS

During aging of a 2124/SiC<sub>w</sub> composite extensive S-phase precipitation occurs at the matrix/reinforcement interface. This precipitation is responsible for producing significantly different mechanical properties during tensile testing of underaged and overaged composites.



with the same matrix properties by increasing load transfer to the SIC<sub>w</sub>.

Tensile testing under hydrostatic pressure does not dramatically alter the plastic ductility of the composite, indicating that failure is very localized.

Suppression of voids in the microstructure, and hence increased plastic ductility of the composite could be produced by the following methods; (i) altering the processing conditions to reduce whisker clustering and hence eliminate void formation in the constrained regions between adjacent SIC whiskers, (ii) adjusting the heat treatment to give less S-phase precipitation and thus a weaker interfacial bond and less SIC whisker cracking, and (iii) using a reinforcement capable of withstanding greater loads along its tensile axis.

#### ACKNOWLEDGEMENTS

This research was supported by the Air Force Office of Scientific Research under Grant No. F49620-87-C-0017. The tensile testing was performed at ALCOA Technical Center when one of the authors (A.K.V.) was employed there.

## REFERENCES

- [1] S. V. Nair, J. K. Tien and R. C. Bates, *Int. Metals Rev.* **30** (1985) 275-290.
- [2] T. W. Chou, A. Kelly and A. Okura, *Composites* **16** (1983) 187-206.
- [3] R. J. Arsenault and R. M. Fisher, *Scripta Met.* **17** (1983) 67-71.
- [4] P. K. Liaw, J. G. Gregg and W. A. Logsdon, *J. Mater. Sci.* **22** (1987) 1613-1617.
- [5] M. Vcgeisang, R. J. Arsenault and R. M. Fisher, *Met. Trans.* **17A** (1986) 379-389.
- [6] R. J. Arsenault and N. Shi, *Mater. Sci. and Eng.* **81** (1986) 175-187.
- [7] K. K. Chawla and M. Matzger, *J. Mater. Sci.* **7** (1972) 34-39.
- [8] T. G. Nieh and R. F. Kariak, *Scripta Met.* **18** (1984) 25-28.
- [9] H. J. Rack, in "Proc. ICCM VI and ECCM 2", Eds. F. L. Matthews, N. C. R. Buskell, J. M. Hodgkinson and J. Morton, Elsevier Applied Science, Amsterdam (1987) Vol. 2, 382-389.
- [10] T. Christman and S. Suresh, Brown University Report No. NSF-ENG-8451092/1/87, June 1987.
- [11] H. J. Rack and J. W. Mullins, in "High Strength Powder Aluminum Metallurgy Alloy II", Eds. M. Koczak and G. Hildemann, TMS-AIME, Warrendale, Pa (1986), 155-171.
- [12] I. Dutta and D. L. Bourell, presented at "Interface Phenomena in Composites: Processing, Characterization and Mechanical Properties", Newport RI, (1988). To be published in *Mater. Sci. and Eng.*
- [13] I. Dutta, D. L. Bourell and D. Latimer, to be published in *J. Comp. Mater.* (1988).
- [14] C. M. Friend and S. D. Luxton, *J. Mater. Sci.* **23** (1988) 3173-3180.

- [15] L.-J. Fu, M. Schmerling and H. L. Marcus, in "Composite Materials, Fatigue and Fracture", Ed. H. T. Hahn, ASTM STP 907 (1986) 51-72.
- [16] R. J. Arsenault and C. S. Pande, *Scripta Met.* 18 (1984) 1131-1134.
- [17] S. R. Nutt, in "Interfaces in Metal Matrix Composites", Eds. A. K. Dhingra and S. G. Fishman, TMS-AIME, Warrendale, PA (1985) 157-167.
- [18] S. R. Nutt and R. W. Carpenter, *Mater. Sci. and Eng.* 76 (1985) 165-177.
- [19] C. Johnson, K. Ono and D. Chellman, in "Composites '88: Recent Advances in Japan and the United States", Eds. K. Kawata, S. Umekawa and A. Kobayashi, Proc. Japan-U.S. CCM III, Tokyo (1988) 647-654.
- [20] J. J. Lewandowski, C. Liu and W. H. Hunt, Jr., in "Powder Metallurgy Composites", Eds. M. Kumar, K. Vedula and A. M. Ritter, TMS-AIME (1987) 647-654.
- [21] C. P. You, A. W. Thompson and I. M. Bernstein, *Scripta Met.* 21 (1987) 181-185.
- [22] S. R. Nutt and J. M. Duva, *Scripta Met.* 20 (1986) 1055-1058.
- [23] S. R. Nutt and A. Needleman, *Scripta Met.* 21 (1987) 705-710.
- [24] B. Derby and J. R. Walker, *Scripta Met.* 22 (1988) 529-532.
- [25] V. C. Nardone and K. M. Prewo, *Scripta Met.* 20 (1986) 43-48.
- [26] R. J. Arsenault, *Mater. Sci. and Eng.* 64 (1984) 171-181.
- [27] M. Taya and R. J. Arsenault, *Scripta Met.* 21 (1987) 349-354.
- [28] H. M. Ledbetter and M. W. Austin, *Mater. Sci. and Eng.* 80 (1987) 53-61.

- [29] T. G. Nieh and D. J. Chellman, *Scripta Met.* 18 (1984) 925-928.
- [30] R. J. Arsenault and S. B. Wu, *Scripta Met.* 22 (1988) 767-772.
- [31] T. Christman, A. Needleman, S. Nutt and S. Suresh, *ibid* ref. [12].
- [32] T. Christman and S. Suresh, *Mater. Sci. and Eng. A*, 102 (1988) 211-216.
- [33] I. E. French and P. F. Weinrich, *Scripta Met.* 8 (1974) 87-90.
- [34] T. E. Davidson and C. S. Ansell, *Trans. AIME* 245 (1969) 2383-2390.
- [35] P. Hirsch, A. Howie, R. B. Nicholson, D. W. Pashley and M. J. Whelan, "Electron Microscopy of Thin Crystals", Butterworths, London (1985).
- [36] M. Kirtani and S. Weissman, *J. Appl. Phys.* 42 (1971) 2603-2611.
- [37] G. Thomas and M. J. Whelan, *Phil. Mag.* 4 (1959) 511-527.
- [38] A. K. Gupta, P. Gaunt and M. C. Chaturvedi, *Phil. Mag. A* 55 (1987) 375-387.
- [39] J. N. Silcock, *J. Inst. Metals* 89 (1980/81) 203-210.
- [40] G. C. Weatherly, Ph.D. Thesis, University of Cambridge, 1988.
- [41] J. J. Stephens, J. P. Lucas and F. M. Hosking, *Scripta Met.* 22 (1988) 1307-1312.

## FIGURE CAPTIONS

Figure 1. Weak-beam dark-field TEM image of 2124/SiC<sub>w</sub> after quenching from the solutionizing temperature. The helical dislocations (H) and dislocations generated from the whisker ends are arrowed;  $g/3g = [111]$ .

Figure 2. Bright-field TEM image of 2124/SiC<sub>w</sub> quenched and aged for 2 hours showing dislocations decorated with small precipitates (arrowed).

Figure 3. (a) Bright-field TEM image of 2124/SiC<sub>w</sub> after aging for 8 hours, and (b) centered dark-field TEM image taken using a precipitate reflection (arrow) showing S' precipitation completely decorating the prior dislocations. The diffraction pattern corresponds to  $[100]_{Al}$ .

Figure 4. Bright-field TEM image of 2124/SiC<sub>w</sub> aged for 8 hours showing extensive, coarse precipitation (arrowed) at the Al/SiC interface.

Figure 5. Typical EDX spectra collected from the Al/SiC<sub>w</sub> interface. (a) As quenched. (b) Aged for 8 hours.

Figure 6. Bright-field TEM image of 2124 quenched and aged for 8 hours at 177°C showing dislocation loop (L) formation in the matrix and helix formation (H) at a coarse intermetallic particle (I).

Figure 7. Tensile data for the (a) underaged, and (b) overaged reinforced and unreinforced materials tested at room pressure and at 689MPa hydrostatic pressure.

Figure 8. Bright-field TEM image of 2124/SiC<sub>w</sub> aged for 8 hours and deformed 3% under 689MPa hydrostatic pressure showing cracked SiC whisker and cracked intermetallic. The tensile axis is indicated (T).

Figure 9. Bright-field TEM Image of 2124/SiC<sub>w</sub> aged for 8 hours and deformed 3% under 689MPa hydrostatic pressure showing decohesion at the Al/SiC<sub>w</sub> interface. The tensile axis is indicated (T) and S precipitates at the interface are distinguished by arrows.

Figure 10. Bright-field TEM image of 2124/SiC<sub>w</sub> aged for 8 hours and deformed 3% under 689MPa hydrostatic pressure showing void formation in the constrained region between adjacent SiC whiskers. The tensile axis is indicated (T).

Figure 11. Bright-field TEM image of 2124/SiC<sub>w</sub> aged for 8 hours and deformed 3% under 689MPa hydrostatic pressure showing void formation at apparently isolated SiC whiskers. The tensile axis is marked (T).



Figure 1

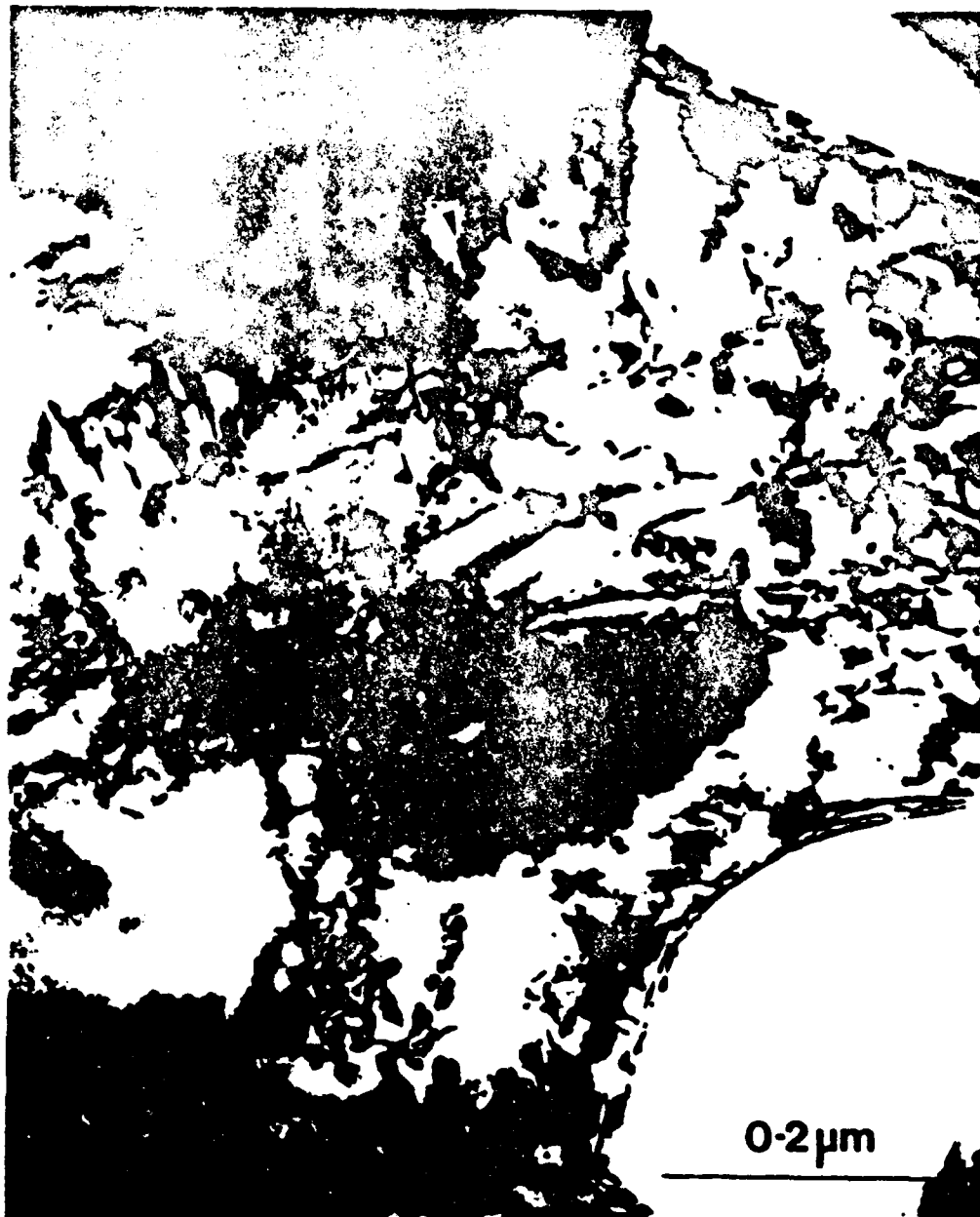


Figure 2





Figure 3



Figure 4

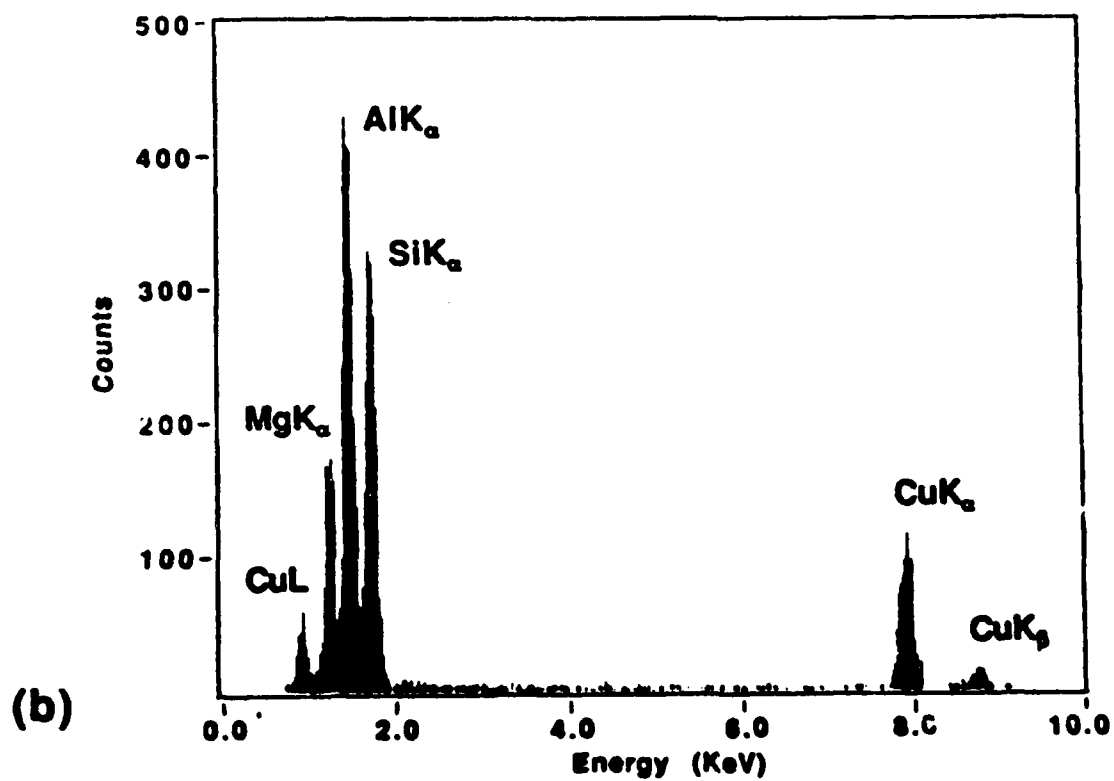
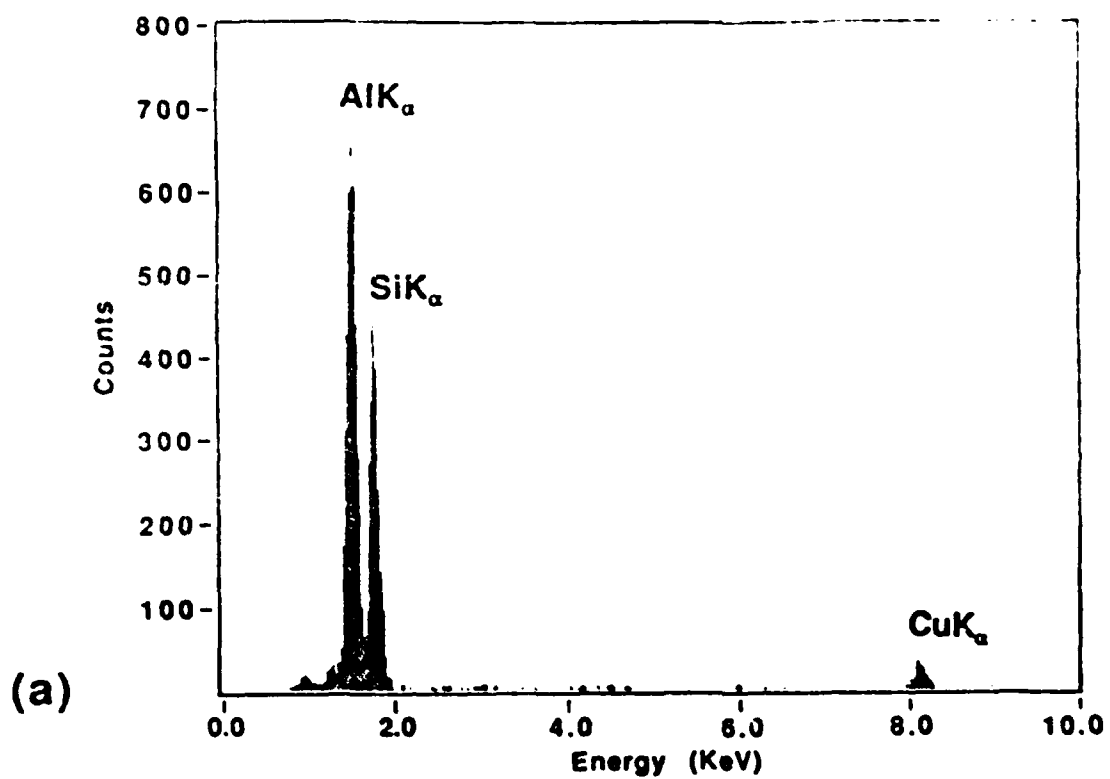


Figure 5



Figure 6

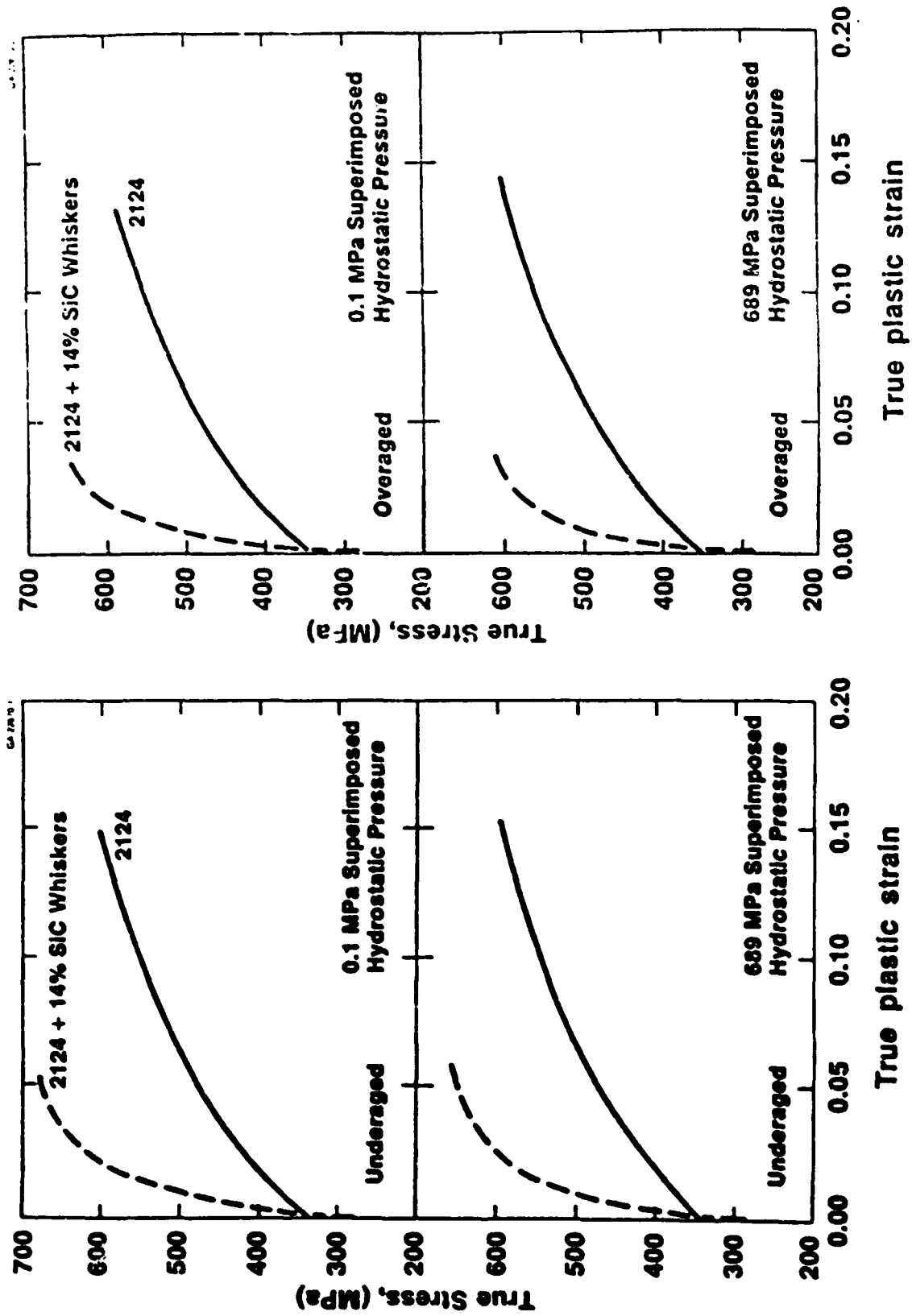


Figure 7



Figure 8



Figure 9

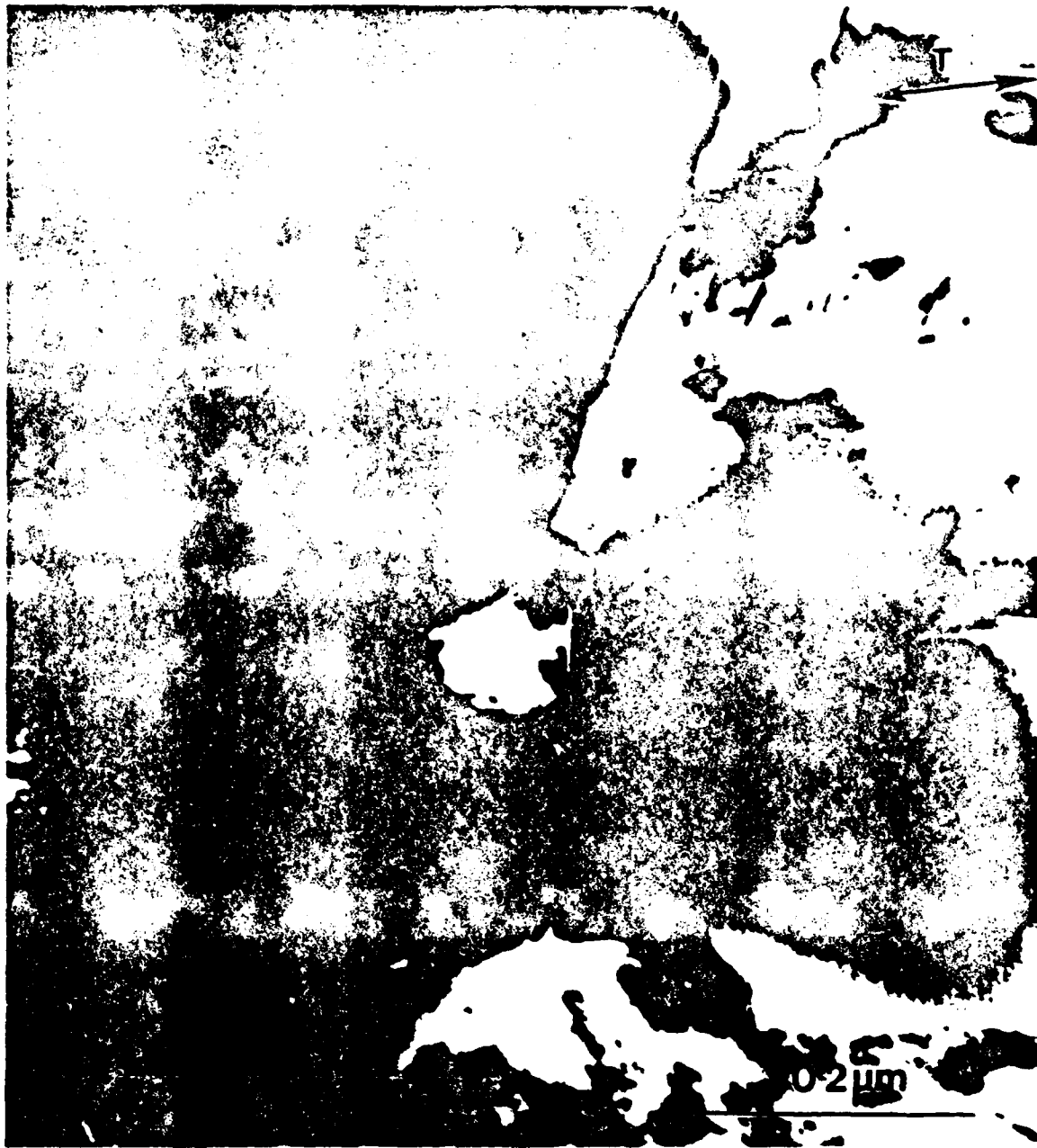


Figure 10





Figure 11

